Diss. ETH No. 19097

Bidirectional Interfacing of Compressed-Air and Electric Power Employing Ultra-High-Speed Drives and Turbomachinery

A dissertation submitted to the
ETH ZURICH

for the degree of
DOCTOR OF SCIENCES

presented by
DANIEL KRÄHENBÜHL
Dipl. El. Ing. ETH Zurich
born 5. August 1982
citizen of Zäziwil, Bern

accepted on the recommendation of
Prof. Dr. Johann W. Kolar, examiner
Prof. Dr. Michael V. Casey, co-examiner

2010

Acknowledgements

I would like to thank many people who made this work possible and who supported me during the last three years at the Power Electronic System Laboratory (PES). First, I would like to thank my supervisor Prof. Dr. Johann W. Kolar for offering me such an exciting research topic, for the stimulating and professional atmosphere and for taking always the time to give me support and advice.

I am very grateful to Prof. Dr. Michael V. Casey for co-referring this thesis, and for spending a part of his sabbatical helping me with optimizing and calculating compressor maps of electrically driven turbomachines.

Furthermore, I want to express my gratitude to the entire PES staff including PhD students, secretaries and especially the electronics workshop, for helping me soldering various electronic prototypes that allowed me to run my experiments.

I also would thank all the semester- and master-theses students who worked with great enthusiasm for the success of this thesis or have been helping me in the teaching activity especially for the practical courses.

This thesis would not have been possible without the support from various people in industry. Special thanks go to Celeroton, hs-turbo (High-Speed Turbomaschinen GmbH), ATE (Antriebstechnik und Entwicklungs GmbH), Myonic, Arnold Magnetic Technologies and last but not least to the ITET and PHYS machine workshops for the manufacturing of most of the mechanical parts.

Finally, I would like to thank everyone who contributed to this thesis and would like to give special thanks also to my girlfriend, my family and friends for their great support during the years of study.

Abstract

In pressure reduction devices, such as valves, conventional throttles or turbo expanders, the ability to obtain work from the pressure drop is usually sacrificed. A mesoscale system for converting pressurized gas flow into electric power is a promising solution for recovering energy from pressure reduction processes and thereby increasing the efficiency of such plants considerably.

Such a device could also supply power to sensors and actuators on industrial robots and thereby reduce the drawbacks in the distribution of electrical energy, like wire attrition through mechanical exposure, loose connection problems and limited mobility.

The trend in compressors for fuel cells, domestic heat pumps, aerospace and automotive heating, ventilation and air conditioning systems, is towards ultra-compact size, low massflow rate, high compression ratio and high efficiency. This can be achieved by using turbocompressors instead of scroll, lobe or screw compressors. Therefore, the reversal of a compressed-air-to-electric-power system (e.g. electric power to compressed gas) is also considered in this thesis.

Several of the above mentioned applications require ultra-compact systems. Power density in both turbomachinery and electrical machines increases with increasing rotational speed. Therefore, to achieve highest power density, these systems operate at rotational speeds between 100 000 rpm and 1 Mrpm at power levels of up to several kilowatts.

The novel system presented in this thesis is a ultra-high-speed, ultra-compact compressed-air-to-electric-power demonstrator that produces an electrical output of 100 W while operating from a compressed air input source with a pressure of 300 kPa to 600 kPa. The demonstrator has to supply a constant dc voltage and must be able to follow load changes; this implies the integration of power electronics, a throttling valve and a DSP based control. Analytical models and simulations for the individual parts (turbine, generator, power electronics, valve and control) have been developed, with the goal of achieving an optimal, i.e. most compact and efficient overall system. This includes the mechanical, thermal, thermodynamic, rotor dynamic and electromagnetic design as well as the control and the coupling of these domains. The results are verified on the basis of two prototype turbine generator systems and power and control electronics.

This research has also resulted in a miniature two-stage electrically driven turbocompressor system with a rotational speed of 500 000 rpm (tested up to 600 000 rpm) for a measured air pressure ratio of 2.25 and a mass flow of 0.5 g/s to 2.5 g/s at ambient conditions for temperature and inlet pressure. The system is the continuation of the development of the one-stage electrically driven turbocompressor and is designed for the cabin air pressurization system of the Solar Impulse airplane.

Kurzfassung

Allgemein geht bei Druckreduzierprozessen, z.B. bei Drosselventilen in Autos, Druckreduzierventilen in Gaspipelines oder Turboexpandern in Kälteanlagen die durch die Druckdifferenz vorhandene potentielle Energie durch Reibungsverluste verloren. Mit kompakten Entspannungsanlagen welche aus der vorhandenen potentiellen Energie elektrische Energie erzeugen, könnte diese zurückgewonnen werden die sonst als Reibungsverlust verpufft, und so die Effizienz solcher Anlagen beträchtlicht gesteigert werden. Eine weitere Anwendung ist in der Automatisierungstechnik, wo die Kommunikation zunehmend drahtlos erfolgt, und ein System, das aus sowieso vorhandener Druckluft lokal elektrische Energie erzeugt, die störanfällige Verkabelung ersetzen könnte.

Der Trend bei Kompressoren für Brennstoffzellen, Wärmepumpen, Heizungen, Klimaanlagen oder Lüftungen für z.B. die Luftfahrt oder den Automobilbereich ist hin zu kompakten Abmessungen, geringem Massedurchfluss bei hohem Kompressionsverhältnis und hoher Effizienz. Dies kann erreicht werden durch die Benützung von Turbokompressoren statt Scroll-, Kolben- oder Schraubenkompressoren. Daher wird in dieser Dissertation auch auf die Umkehrung, eines Systems welches Strom produziert während ein Gas expandiert, also auf die Nutzung elektrischer Leistung zur Komprimierung von Gasen näher eingegangen.

Applikationen im Automobilbereich oder auf Robotern in Fertigungsanlagen brauchen hochkompakte Systeme. Die Leistungsdichte von Turbomaschinen sowie elektrischen Maschinen steigt mit zunehmender Drehzahl, es sind daher möglichst hohe Drehzahlwerte zu wählen. Deshalb sind für Systeme mit höchster Leistungsdichte, in der Leistungsklasse von 100 W bis zu einigen Kilowatt, Drehzahlen an den technologischen Grenzen zwischen 100 000 U/min und 1 000 000 U/min zu wählen.

Der Schwerpunkt dieser Dissertation liegt in der Konzeption und theoretischen und experimentellen Analyse eines 100 W Turbinen-Generator-System welches aus Druckluft (300 kPa bis 600 kPa) unter Hinzunahme einer Leistungselektronik eine elektrische Gleichspannung erzeugt. Die Einzelteile Turbine, Generator, Elektronik, Ventil und Regelung werden mit dem Ziel eines optimalen, d.h. möglichst kompakten und effizienten Gesamtsystems evaluiert und analysiert. Dazu gehören die mechanische, thermische, aerodynamische, rotordynamische, elektromagnetische und regelungstechnische Modellierung und die Koppelung dieser Modelle. Die Resultate werden anhand zweier Prototypen von Turbinen-Generator-Systemen und einer Leistungs- und Steuerelektronik verifiziert.

In dieser Dissertation wird auch ein zweistufiger, elektrisch angetriebener Turboverdichter mit einer Nenndrehzahl von 500 000 U/min (bis zu 600 000 U/min getestet), einem gemessenem Druckverhältnis von 2,25 und einem Massenstrom von 0.5 g/s bis 2.5 g/s bei Umgebungsbedingungen für Temperatur und Eingangsdruck realisiert. Das System ist eine Weiterentwicklung eines einstufigen Turboverdichters und wurde speziell für die Regulierung des Luftdruckes in der Kabine des Solar Impulse Flugzeuges entwickelt.

Notation

Symbols

c	velocity
c_f	air friction coefficient
c_{m1}, c_{m2}	meridional component of the absolute velocities c_1, c_2
c_{th}	heat capacity
c_{u1}, c_{u2}	circumferential component of the absolute velocities c_1, c_2
c_p	specific heat capacity
d	diameter, duty cycle
d_h	rotor blade height
d_s	specific diameter
f	frequency
f_f	fundamental frequency
f_s	switching frequency
g	acceleration of gravity
h	enthalpy
i	current
l	length
m	mass
$\dot{m}$	mass flow
n	rotational speed or polytropic exponent
p	pressure
q	heat
r	radius

r_m	median radius
t	time
u	circumferential speed, internal energy or voltage
$\underline{u}$	voltage space vector
u_{rm}	circumferential speed at radius r_m
u_1	circumferential speed at radius r_1
u_2	circumferential speed at radius r_2
w	relative velocity
w_{m1}, w_{m2}	meridional component of the relative velocities w_1, w_2
w_{u1}, w_{u2}	circumferential component of the relative velocities w_1, w_2
w_{12}	specific work
z	altitude
A	area
A_{u1}	effective turbine inlet area
A_{u2}	effective turbine outlet area
B	magnetic flux density
B_{rem}	remanence flux density
C	capacitance
C_m	Steinmetz coefficient
D	angular momentum or diode
F	copper loss coefficient
G	copper loss coefficient
$G_{Pearson}$	attenuation of Pearson 2877 current probe
G_{LISN}	attenuation of LISN
$\hat{I}$	amplitude of block-type currents
J	inertia
L	inductance
M	Mach number or voltage transfer ratio
P	active power or power losses
P_{Cu}	copper losses
$P_{Cu,I}$	current dependent copper losses
$P_{Cu,p}$	proximity effect copper losses
$P_{Cu,s}$	skin effect copper losses

P_{Air}	air friction losses
$P_{d,dec}$	deceleration power losses
P_{el}	electric power
P_m	mechanical power
R	resistance or ideal gas constant
R_1	radius of the permanent magnet
R_2	outer radius of the rotor sleeve
R_3	inner radius of the stator winding
R_4	inner radius of the stator core
R_5	outer radius of the stator core
Re	Reynolds number
$R_{th,ax}$	heat flow in axial direction
$R_{th,rad}$	heat flow in radial direction
S	switch
T	transistor switching signals, torque or temperature
T_t	total temperature
$T_{d,dec}$	breaking torque
T_m	mechanical torque
V	voltage or volume
$\dot{V}$	volume flow
W	rotational energy
α	Steinmetz coefficient
α_1	angle of c_1
α_2	angle of c_2
β	Steinmetz coefficient
β_1	angle of w_1
β_2	angle of w_2
ϵ_m	rotor magnet angle
η_s	isentropic efficiency
η_m	electric machine efficiency
η_n	nozzle guide vane efficiency
κ	specific heat ratio
λ	work coefficient, power factor or heat conductance

λ_{Euler}	Euler's work coefficient
ν	Poisson's ratio or kinematic viscosity
ρ	density
ρ_t	total density
σ	conductivity
σ_r	radial stress
σ_θ	tangential stress
ϕ	flow coefficient
ψ	pressure rise coefficient or flux linkage
ω	angular frequency
ω_s	specific speed
Π	pressure ratio
Ψ	flow function or flux linkage

Subscripts

0	nozzle guide vane inlet
1	nozzle guide vane outlet / turbine inlet
2	turbine outlet
a, b, c	phase a, b, c
avg	average value
ax	axial direction
Cu	copper
d	direct-axis component
Fe	iron
m	meridional component
$meas$	measured value
n	negative
off	'off' state of a switch
on	'on' state of a switch
p	polytropic, proximity effect component or positive
pm	permanent-magnet
r	radial component or rated
ref	reference value
res	resonance
rms	root mean square value
rot	rotational energy
s	isentropic or skin effect
S	machine stator
t	total or terminal
θ	tangential/azimuthal component

Abbreviations

ADC	Analog-to-digital converter
BLDC	brushless dc machine
CFD	computational fluid dynamics
CISPR	Comité international spécial des perturbations radioélectriques
CM	common-mode
DC	direct current
DSP	digital signal processor
EMC	Electromagnetic Compatibility
emf	electromotive force
FE	finite element
HCBR	half controlled 3-phase PWM boost rectifier
HF	high frequency
HVAC	heating ventilation and air conditioning
IFR	inward-flow radial turbine
LISN	line impedance stabilization network
LUT	lookup-table
MEMS	micro-electro-mechanical systems
MOSFET	metal oxide semiconductor field effect transistor
PAM	pulse amplitude modulation
PCB	printed circuit board
PI	proportional-integral controller
PM	permanent magnet
PMSM	permanent magnet synchronous machine
PWM	pulse width modulation
rpm	revolutions per minute
VSI	voltage source inverter

Contents

Chapter 1

Introduction

1.1 Motivation

In pressure reduction devices, such as valves, conventional throttles or turbo expanders, the ability to obtain work from the pressure drop is usually sacrificed. However, this potential energy could be recovered by employing a system that removes energy from the pressurized gas flow and converts it into electrical energy. With such a new pressure reduction system that produces electricity while expanding a pressurized gas flow, the lost potential to obtain work output can be recovered.

The trend in compressors for fuel cells, heat pumps, aerospace and automotive heating, ventilation and air conditioning systems, is towards ultra-compact size, low massflow rate, high compressor ratio and high efficiency. This can be achieved by using turbocompressors instead of scroll, lobe or screw compressors and by increasing the rotational speed. Therefore, also the reversal of a compressed-air-to-electric-power system to an electric-power-to-compressed-air system is a promising research area.

Power density in both turbomachinery and electrical machines increases with increasing rotational speed [1], [2]. Therefore, for highest power density and ultra-compact systems, these systems are operating at rotational speeds between 100 000 rpm and 1 Mrpm at power levels of up to several kilowatts.

1.2 Applications

1.2.1 Replacement of Throttling Valves of Natural Gas Pipelines

While it is necessary to transport natural gas at high pressures, end-users require gas delivery at only a fraction of the main pipeline pressure. Therefore, energy can be recovered at pressure reduction stations if throttling valves are replaced by expanders driving electrical generators [3]. For power recovery, turbines are generally rated from 150 kW to 2.5 MW; however, the pressure reduction process is usually done in several stages, and an array of small turbine-generator modules could replace one large pressure reduction valve [4].

1.2.2 Replacement of Throttling Valves in Automotive Applications

In [5], the replacement of a conventional throttle with a turbine in combination with a generator which can actively throttle the intake air and thereby produce electrical power is presented for an automotive application (Figure 1.1). Measurements at constant speed have shown that up to 700 W of electric power could be extracted (turbine ∅ 40 mm) and an extrapolation with a 50% downsized turbine predicts that even more electric power could be produced. At very high engine power the turbine is not able to provide sufficient air to the engine while at very low power the pressure drop over the turbine is not sufficient. For these reasons a bypass valve and a downstream throttle valve are used in addition.

1.2.3 Energy Recovery from Exhaust Gas in Automotive Applications

Conventional combustion engines lose up to one-third of the energy contained in the fuel as heat through the exhaust pipe. An attractive solution to meet the increased electrical power demand of modern cars and trucks is to convert the thermal energy in the exhaust gas into electrical energy by means of a generator driven by a high-speed, exhaust-mounted turbine [6]. The partial recovery of this otherwise wasted energy offers significant benefits in terms of increasing the overall system efficiency. This

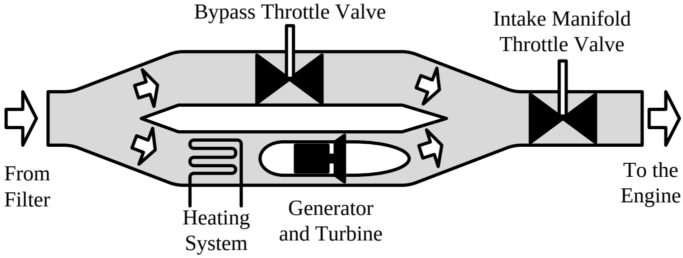

Figure 1.1: *Replacement of the conventional throttle by a turbine-generator-system in automotive applications.*

Turbo generator Integrated Gas Energy Recovery System (TIGERS) delivers a shaft power of up to 6 kW at speeds up to 80 000 rpm from the 900°C hot exhaust gases and a massflow of typically 50 g/s. The small turbo-generator is installed in a by-pass waste pipe fitted just below the engine exhaust manifold. A valve linked to the engine's control system allows some of the high-energy exhaust gases to pass through a turbine to drive the generator, depending on engine load conditions [7]. Compared with a conventional alternator at medium to high engine load, this is a more efficient way to generate electric power [8].

For the described applications in section 1.2.2 and section 1.2.3 light, compact and highly efficient turbine-generator systems including a power electronics are required.

1.2.4 Turbo Expanders in Cryogenic Plants

In cryogenic plants, output stage turbo expanders (in the kW range with speeds of several 100 krpm) are braked through a compressor. The compressed and hot fluid is cooled with a water cooler and expanded over a brake valve (Figure 1.2(a)). The three components compressor, cooler and valve could be replaced with an electric generator (Figure 1.2(b)) and thereby electricity could be produced, and the efficiency of such plants could be increased [9]. Since the turbo expander and the brake cooler are located near each other, the temperature gradient between the cold expander and the warm compressor is extremely high. With the use of an electrical brake no such high temperature gradient would occur, which

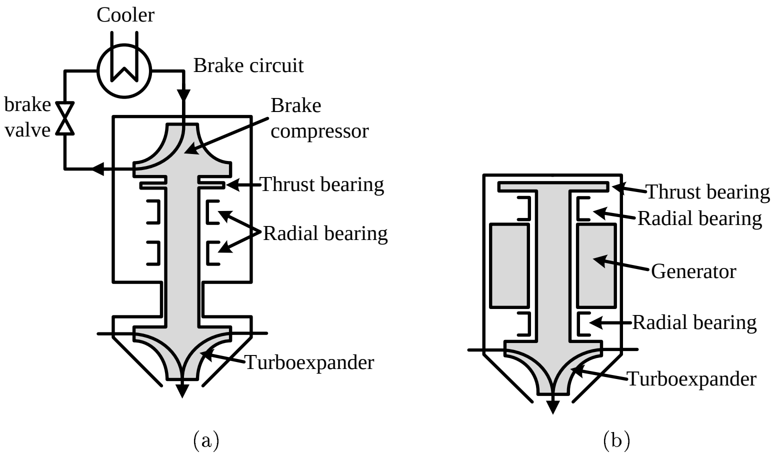

Figure 1.2: *State of the art output stage cryogenic turboexpander including brake compressor, cooler and brake valve Figure 1.2(a) or the replacement with an high-speed electric generator Figure 1.2(b).*

is a further advantage [10].

1.2.5 On-site Electric Power Generation on Industrial Robots

In state-of-the-art processing plants, sensors and actuators on industrial robots require electrical and compressed air connections. There are a few drawbacks in the distribution of electrical energy, like the wire attrition through mechanical exposure, loose connection problems, the limited mobility because of the complicated cable routing and the time-consuming wiring and therefore complex implementation and assembling. All this leads to high failure rates, frequent preventive maintenances and therefore an increase in costs. On the other hand, compressed air can be easily distributed and the hose connections of compressed air are less sensitive than electrical connectors. A light and compact device that generates electrical energy from compressed air, shown in Figure 1.3, for powering actuators and wireless sensors, can avoid the mentioned disadvantages of electrical power distribution [11].

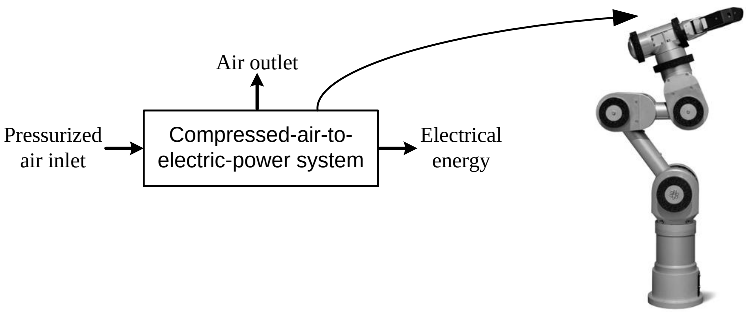

Figure 1.3: *Compressed-air-to-electric-power system mounted on industrial robots. Compressed air hose connections are more robust than electrical connections, therefore distribution of electrical energy could in future be replaced by local electric power generation.*

1.2.6 Organic Rankine Cycle Energy Recovery Systems

Conceivable applications for the Organic Rankine Cycle (ORC) (or more generally for the low temperature Rankine Cycle) are waste heat recovery, solar thermal power and geothermal plants. Using heat from one of the mentioned sources, a working fluid (organic fluids with low evaporating temperatures [12]) gets vaporized under pressure and is fed to the inlet of the expander. The exhausted working fluid is then sent through a regenerator to recover thermal energy, usually followed by an air-cooled condensation heat exchanger. To complete the cycle, the working fluid is passed through a pump and is fed back to the vaporiser (Figure 1.4). Utilizing a Rankine Cycle obtains the highest efficiency when converting low temperature thermal energy into electricity.

Using heat from a hot oil supply (183°C) and the working fluid R123, a small-scale regenerative Rankine power cycle using a scroll expander was built and tested in [13]. With an ambient air temperature of 22.5°C cooling the condenser, the system produced 256 W of gross power (not including the electrical input to run the fans and pumps) while the system efficiency was 7.2%. The critical component limiting the overall system efficiency was the scroll expander, which was measured at levels between

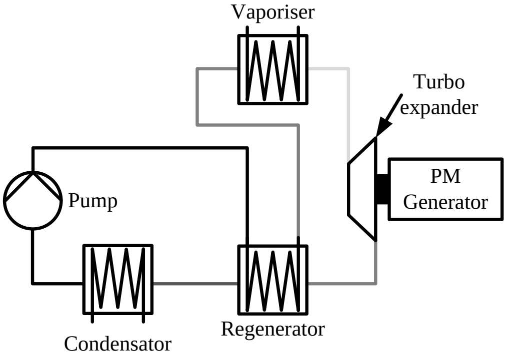

Figure 1.4: *Major components of an Organic Rankine Cycle energy recovery systems.*

45% and 50%. Replacing the scroll expander with a high-speed turboexpander would increase the overall system efficiency, and due to the speed increase, also a more compact and lightweight system could be built.

1.2.7 Further Throttling Applications

In theory, a turbine with attached generator could replace throttling devices (which decreases pressure and consequently temperature) as widely used in several systems such as refrigerator, air conditioner, heat pumps, etc., and thereby extract any potential work from the high pressure fluid and use it to recover some energy that could be used to drive the compressor. However, turbines would have to deal with the mostly liquid fluids at the cooler outlet and the added overall efficiency seldomly justifies the cost of the rather complex turbine generator system compared to a simple throttling device. Additionally, the overall system volume and complexity increases. However, especially where high efficiencies are required like in [14], where a vapor compression refrigeration system with isobutane as a working fluid for the cooling of high power components in a notebook PC is presented, a turbine generator instead of a throttling valve may be a good alternative.

1.2.8 Electrically Driven Turbocompressors

Although not the main topic of this thesis, turbocompressors can also be seen as an application of a reversed turbine-generator system. In future cars and airplanes more and more hydraulic, pneumatic and mechanical systems, also compressors will be replaced with electrically driven systems: the trend is towards more electric aircrafts and vehicles. Examples are compressors for heating, ventilation and air conditioning (HVAC) in cars or air pressurization for aircraft cabins. The power levels of these electrically driven compressors are from about 100 W up to a few kilowatts. Additionally, several car manufacturers have research projects or even prototypes of electric vehicles with fuel cell propulsion systems, or a fuel cell system as range extender. Also in trucks and aircraft, fuel cells are planned to be used as auxiliary power units. A manned aircraft with a fuel cell/lithium-ion battery hybrid system to power an electric motor coupled to a conventional propeller, successfully completed a flight in Spain [15]. At Georgia Institute of Technology, unmanned fuel cell-powered aerial vehicles (UAVs) have been designed and tested [16].

All these fuel cells usually need an electrically driven air compressor which consumes around 10-20% of the output power of the fuel cell, and the pressure levels are usually between 150 kPa and 250 kPa [17]. The electrically driven air compressor should be small, lightweight and efficient.

Other applications for electrically driven compressors are residential applications like heat pumps, in order to enable a more rational use of energy [18]. Also there, the trend is towards more compact systems with a higher efficiency. Distributed heat pump systems could be realized with smaller compressors and expanders. Turbocompressors have advantages concerning size and efficiency over other compressor types, such as scroll, lobe or screw compressors [17].

1.3 State of the Art

Besides common high power gas turbines for centralized power generation, micro-turbines with less than 100 W power output and very high rotational speeds have been reported in literature, usually for distributed and/or portable power generation.

In [19], a modular system consisting of an off-the-shelf air turbine from a dental drill, a PM generator and a rectifier has been realized, with a maximum power output of 1.11 W and a maximum speed of 200 000 rpm. Drawbacks of this system are the poor power density (0.02 W/cm^3) and the large inlet flow rate of 45 l/min at maximum output power. The power electronics of the system consists of a 3-phase transformer, a diode bridge rectifier and a 5 V linear regulator.

In [20] and [21], a single-stage axial turbine coupled to a commercial electrical machine with a maximum electric power output of 16 W at 160 000 rpm and 200 kPa supply pressure has been introduced for later use in a gas turbine system [22]. The maximum torque and mechanical power generated from the turbine is 3.7 mNm and 28 W, respectively. An improved turbine has been tested at temperatures up to 360°C and generates up to 44 W of electrical power with a total efficiency of 16%. The generator is connected to a variable 3-phase resistive load to measure the electric output power. The total system has a maximum efficiency of 10.5% at 100 000 rpm and achieves a power density of 1.6 W/cm^3, excluding power and control electronics.

A micro fabricated axial-flux PM generator has been reported in [23] and [24]. The generator has been manufactured using a combination of micro fabrication and precision machining. At a rotational speed of 120 000 rpm, the generator produced 2.5 W of electrical power. A second generation PM generator is presented in [25], capable of supplying 8 W of dc power to a resistive load at a rotational speed of 305 000 rpm. The stator uses interleaved, electroplated copper windings on a magnetically soft substrate. The rotor consists of an 8-pole SmCo PM, a back iron and a titanium sleeve to limit the centrifugal forces on the PM. The machine was characterized using an air-driven spindle. To provide a dc voltage, the ac generator voltages were first stepped up using a 3-phase transformer and then converted to dc using a 3-phase Schottky diode rectifier. The dimensions of the device are chosen with reference to a future integration into a micro turbine engine. This leads to a power density of the generator of 59 W/cm^3 and to a generator efficiency of 28%. The combination of [25] with a silicon turbine is presented in [26]. The generator of this fully integrated PM turbine generator system has delivered 19 mW to a resistive load at a rotational speed of 40 000 rpm.

A planar generator with a diameter of 8 mm consisting of a PM disc rotor cut out of bulk SmCo or NdFeB protected by a titanium sleeve, and a silicon stator with electroplated 3-phase planar coils is presented in [27]. The generator is driven by a planar turbine, etched into the opposite side of the rotor. Due to the turbine construction, the speed is limited to 100 000 rpm with 500 kPa compressed air supply. A maximum power output of 14.6 mW was measured at 58 000 rpm with three Y-connected 50 Ω resistors. Using a turbine of a dental drill, the rotor reached a maximum speed of 420 000 rpm. With this setup, the highest electric power output of 5 W (three Y-connected 12 Ω resistors) was reached at 380 000 rpm with an electrical efficiency of 66%.

In [10] the design of a super-high speed PMSM (200 000 rpm, 2 kW) operating at 77 K is described. Properties of most materials change significantly with temperature and thus many materials are unsuitable for cryogenic applications, i.e., some materials will become very brittle at such low temperatures. However the motor construction is very similar to the generator used for the compressed-air-to-electric-power system presented in this thesis. The rotor of the PM motor consists of a diametrically magnetized cylindrical SmCo PM encased in a retaining titanium sleeve while the slotless stator consist of a multi-strand litz-wire winding, to reduce the eddy current losses and thin laminated silicon steel.

[11] presents the details of the aero-thermodynamic and mechanical design of an air-to-power (A2P) device and outlines its assembly and experimental testing. The A2P system was designed and built around a 2-pole 3-phase Y-connected PM synchronous machine capable of operating at a speed of 500 000 rpm, and a torque of 1 mNm [28]. The turbine was manufactured with MEMS technology, while the housing was machined. Measurements at 360 000 rpm, a pressure ratio of 3.34 and a consumed physical mass flow of 0.87 g/s showed 30 W of electrical power, which results in a system efficiency of 39.3%.

In [29] the feasibility of a 100 W micro-scale gas turbine has been studied by experimentally verifying individual components like gas bearings, compressor, combustor and the isolation between compressor and turbine. The rotor is required to rotate at 870 000 rpm to generate the compressor pressure ratio of 3 at a mass flow rate of 2 g/s. It is supported by using hydroinertia gas bearings. The combustor has achieved stable self-sustained combustion with a combustion efficiency higher than 99.9%. [30] reports the demonstration of the Brayton cycle, which was established at 360 000 rpm using the components described in [29]. [31] describes the design and test results of an ultra-high-speed tape type radial foil bearing for the mobile gas turbine generator. The foil bearing was tested, and the maximum stable rotation speed of 642 000 rpm was recorded, with no significant deterioration of the bearing performance even after 300 start-and-stop cycles.

[32] presents a very-high-speed (VHS) slotless PMSM design procedure using an analytical model, used to design a 200 krpm and 2 kW motor. The multiphysics analytical model allows a quick optimization process, including the magnetic field, the mechanical stresses in the rotor, the electromagnetic power losses, the windage power losses, and the power losses in the bearings. At 200 krpm an efficiency of 87.0% and an output power of 2.19 kW has been measured, while a maximum speed of 206 krpm was achieved.

In [33] an overview of compact (less than a few cubic centimeters) magnetic power generation systems in the microwatts to tens of watts power range are discussed, including a comprehensive summary and comparative review of the different types (rotational, oscillatory, and hybrid devices) of experimentally measured small magnetic power generators.

1.4 Challenges

The design, construction and testing of compressed-air-to-electric-power systems and electrically driven compressors is not trivial. The main challenges are:

- The selection and design of high-speed turbines with small tip clearances.
- The reduction of the high-frequency losses in the machine design, mainly the eddy current losses in copper and iron and air friction losses.
- The selection of an ultra-compact and highly efficient power electronics topology to generate a constant dc voltage from a variable speed PM generator for the compressed-air-to-electric-power system and the selection of a proper power electronics topology for driving ultra-high-speed compressors.
- A suitable valve selection, for a compact size, low power consumption, fast response time, and accurate displacement.

- Modeling of the different parts of the compressed-air-to-electric-power system and the implementation of a digital control in order to provide a constant dc output voltage for variable loads.

- Integration of the turbine-generator assembly, the power electronics and the valve, including a sophisticated thermal design, and concepts for ensuring low mechanical stresses on the rotor, and the analysis of rotor dynamics.

1.5 Outline of the Thesis

In this thesis, bidirectional interfacing of compressed-air and electric power employing ultra-high-speed drives and turbomachinery is analyzed. The coupling of an impeller with an ultra-high-speed electric machine can be used as compressed-air-to-electric-power system (Figure 1.5) or as an electric-power-to-compressed-air system (Figure 1.6). For the sake of completeness, the two systems should be theoretically analyzed, designed and assembled and finally experimentally analyzed.

A main goal of this thesis is the theoretical and the experimental analysis of an ultra-compact, compressed-air-to-electric-power demonstrator that produces an electrical output of 100 W while operating from a compressed air input source with a pressure of 300 kPa to 600 kPa. The demonstrator, as block diagram in Figure 1.5, should supply a constant 24 Vdc output and must be able to follow load changes; this implies the integration of power electronics which transform the variable 3-phase output of the generator into a constant output voltage, a valve and a DSP based control system which modulates the air flow and controls the power electronics according to the load demand. With the goal of an optimal overall system, i.e. as compact and efficient as possible, the individual components of the compressed-air-to-electric-power demonstrator (turbine, generator, power electronics, valve and control system) have to be selected, designed and analyzed. This also includes mechanical, thermal, aerodynamic, rotor dynamic and electromagnetic models, the coupling of these models and the design of the different controllers. For making the overall volume as small as possible, the power and control electronics will be integrated into to the system. As a positive side effect no additional heat sink is needed if the electronics are thermally attached

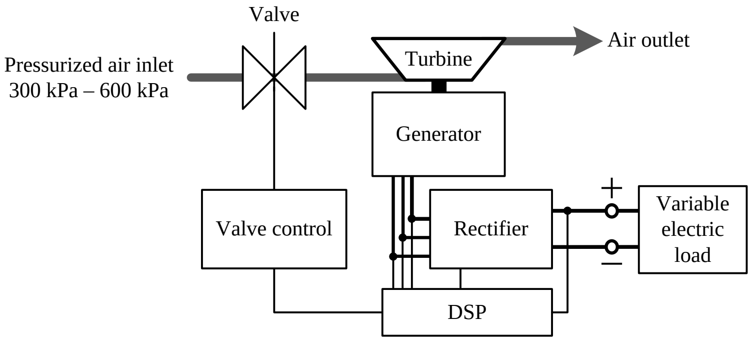

Figure 1.5: *Block diagram of the compressed-air-to-electric-power system including a valve for output power regulation and a rectifier for converting a variable 3-phase input voltage into a constant dc output voltage.*

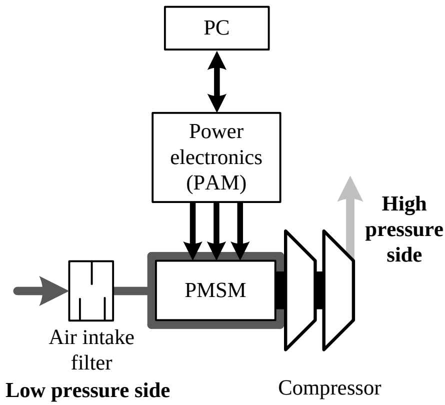

Figure 1.6: *Block diagram of the two-stage, electrically driven turbo-compressor including the pulse amplitude modulation (PAM) power electronics and control system for driving an ultra-high-speed PMSM.*

to the generator casing and thereby cooled by the air flow. Such a device could also be powered with portable compressed gas (i.e. cartridges).

A second goal of this thesis is the theoretical and experimental analysis of an ultra-compact, electrically driven two-stage turbocompressor with a rated rotational speed of 500 000 rpm for a calculated air pressure ratio of 2.25 and a mass flow of 1 g/s (Figure 8.2) and as block diagram in Figure 1.6.

After the introduction with a description of possible applications in chapter 1, chapter 2 presents a short overview of non-dimensional parameters and similarity relations of turbomachinery and geometrical restrictions in small size turbomachines followed by a comparison of different turbine types and the turbine selection for the compressed-air-to-electric-power demonstrator. A 1-D design and a CFD simulation of the turbine is undertaken.

Chapter 3 gives a short overview of the challenges in high-speed machine design, like mechanical rotor design including rotor dynamics and the minimization of high-frequency losses due to eddy currents, followed by the system integration of the turbine-generator system.

In chapter 4 different 3-phase ac/dc rectifiers for a turbine generator system are evaluated, and compared concerning losses, total efficiency, CM noise, volume, and control complexity. The most suitable topology the HCBR is selected and experimentally verified and tested. Furthermore a review of the HCBR topology and two different modulation methods are presented.

Chapter 5 starts with a description and experimental results of the valve of the compressed-air-to-electric-power system, continuing with simulation results of the remaining three major components (turbine, generator and power electronics), resulting in a simulation of the entire system.

In chapter 6 and in chapter 7 two hardware prototypes, a high-speed ultra-compact and fully integrated compressed-air-to-electric-power system with a rated rotational speed of 350 000 rpm and a rated power output of 60 W and a reversal of an existing electric motor-driven compressor system [34], are analyzed experimentally and compared between the simulation and measurements.

In chapter 8, a miniature two-stage electrically driven turbocompressor system is presented. It has a rated rotational speed of 500 000 rpm for a calculated air pressure ratio of 2.25 and a mass flow of 1 g/s at ambient conditions for temperature and inlet pressure. The system is designed for the cabin air pressurization system of the Solar Impulse airplane [35].

Finally, in chapter 9 the results of this thesis are concluded and an outlook is given.

1.6 Scientific Contributions

The following list summarizes the main contributions presented in this thesis.

- Design considerations for a radial turbine coupled to a high-speed generator including not only the evaluation and comparison of the major parts but also the system integration are given in [I] and verified with measurements in [III].
- Evaluation, comparison and selection methods for an axial turbine coupled to a high-speed generator are given and experimentally verified in [II].
- [IV] compares measured radial and axial impulse turbine efficiencies as well as the corresponding assembled turbine-generator system efficiencies. Also an overview of international research on high-speed turbine-generator systems is given.
- In [VI] and [VII] the selection process for an ultra-compact, highly efficient power and control electronics is presented, in order to generate a constant dc voltage from a variable high-speed PM generator. Because literature reports only limited information, the most suitable, i.e. the half controlled 3-phase PWM boost rectifier (HCBR), is reviewed concerning current stresses, CM characteristics, and operating principles. Furthermore a novel modulation scheme improving the power electronics efficiency is proposed and verified by integration into a compressed-air-to-electric-power system.
- A 500 000 rpm electrically driven turbocompressor for various applications in the area of air and gas pressurization for future automotive, aerospace and residential applications with a strong link to renewable energy systems is presented in [V] and [VIII]. Furthermore a sophisticated thermal design, suitable for two extreme operating points, is developed.

1.7 List of Publications

Publications originating from this Ph.D. project are:

[I] D. Krahenbuhl, C. Zwyssig, H. Weser, and J. W. Kolar, "Mesoscale Electric Power Generation from Pressurized Gas Flow," in *Proc. of the 7th International Workshop on Micro and Nanotechnology for Power Generation and Energy Conversion Applications (PowerMEMS 07)*, Freiburg, Germany, Nov. 2007, pp. 289–292.

[II] D. Krahenbuhl, C. Zwyssig, H. Horler, and J. W. Kolar, "Design Considerations and Experimental Results of a 60 W Compressed-Air-to-Electric-Power System," in *Proc. of the 2008 IEEE/ASME International Conference on Mechatronic and Embedded Systems and Applications (MESA 08)*, Beijing, China, Oct. 2008, pp. 375–380.

[III] D. Krahenbuhl, C. Zwyssig, H. Weser, and J. W. Kolar, "Experimental Results of a Mesoscale Electric Power Generation System from Pressurized Gas Flow," in *Proc. of the 8th International Workshop on Micro and Nanotechnology for Power Generation and Energy Conversion Applications (PowerMEMS 08)*, Sendai, Japan, Nov. 2008, pp. 377–380.

[IV] D. Krahenbuhl, C. Zwyssig, H. Weser, and J. W. Kolar, "Theoretical and Experimental Results of a Mesoscale Electric Power Generation System from Pressurized Gas Flow," in *Journal of Micromechanics and Microengineering*, vol. 19, no. 9, Sep. 2009, 094009 (6pp).

[V] D. Krahenbuhl, C. Zwyssig, H. Weser, and J. W. Kolar, "A Miniature, 500 000 rpm, Electrically Driven Turbocompressor," in *Proc. of the IEEE Energy Conversion Congress and Exposition (ECCE 09)*, San Jose, California, USA, Sept. 2009, pp. 3602–3608.

[VI] D. Krahenbuhl, C. Zwyssig, K. Bitterli, M. Imhof, and J. W. Kolar, "Evaluation of Ultra-Compact Rectifiers for Low Power, High-Speed, Permanent-Magnet Generators," in *Proc. of the 35th Annual Conference of the IEEE Industrial Electronics Society (IECON 09)*, Porto, Portugal, Nov. 2009, pp. 453–460.

[VII] D. Krähenbühl, C. Zwyssig, and J. W. Kolar, "Half Controlled Boost Rectifier for Low Power, High-Speed, Permanent-Magnet Generators," Accepted for publication in *IEEE Transactions on Industrial Electronics.*

[VIII] D. Krahenbuhl, C. Zwyssig, H. Weser, and J. W. Kolar, "A Miniature 500 000-r/min Electrically Driven Turbocompressor," *IEEE Transactions on Industry Applications*, vol. 46, no. 6, pp. 2459–2466, Nov.–Dec. 2010.

Chapter 2

Turbine Selection and Design

In this chapter a short overview of non-dimensional parameters, similarity relations of turbomachines and geometrical restrictions in small size turbomachines are presented. An overview and a general discussion of compressor characteristics, and the most important non-dimensional parameters are also presented in [36]. Using non-dimensional parameters in the description of turbomachinery reduces the number of parameters which represent the physical behavior. This is done by a few dimensionless parameters as a function of original measurable parameters, as listed by [37] based on experimental evidence and dimensional analysis. The advantages are an easy comparison and selection of turbomachines for a certain application and a convenient way to convert the measured overall performance (efficiency, power, pressure rise and volume flow rate) of a certain machine at a certain speed to other conditions, such as a different speed, different inlet conditions or a geometrically similar machine of a different size.

Going towards smaller size, a simple geometrical downscaling of high performance large gas turbines will not result in a good micro gas turbine. The main factors perturbing such a scaling are according to [38]:

- The large change in Reynolds number.

- Massive heat transfer between the hot and cold components.
- Geometrical restrictions related to material and manufacturing of miniaturized components.

A major implication for micro turbines is therefore the decrease of efficiency with decreasing dimensions. [38] shows that for a given pressure ratio, the efficiency decreases as the size and mass flow reduces, which is even further worsened by the effect of larger roughness resulting from materials and manufacturing techniques. In [39] fundamental aerothermodynamic differences between conventional, large scale and micro turbomachinery operation and performance are described and the implications on the design are discussed.

2.1 Similarity and Non-Dimensional Parameters

Essentially all of the following three similarities must be valid for the conversion of two turbomachines to be operating at similar non-dimensional conditions [36]:

- **Geometrical similarity** - the geometrical parameters of the two machines differ only through scaling in size with a certain scaling factor.
- **Fluid dynamic similarity** - the kinematic motion of the fluid and the dynamic forces acting on the blades are similar in non-dimensional terms.
- **Thermodynamic similarity** - the change in gas conditions (ratios of temperatures, pressures and densities) are similar in the two machines.

Each of these conditions leads to special non-dimensional similarity parameters.

2.1.1 Geometric Similarity

The geometrical similarity simply implies that all dimensions of the machine scale with the same factor. However even such an easy requirement may be difficult to fulfill in practice. When scaling a machine to a smaller size some features tend to remain the same size in absolute dimensions, such as the surface roughness or the absolute size of the fillet radii, or the size of small clearance gaps and leakage flow paths. Also the blade thickness cannot be reduced below a limit defined by the manufacturing method or mechanical robustness. For downscaled machines these terms become relatively larger, and therefore influence the overall efficiency negatively.

2.1.2 Fluid Dynamic Similarity

Fluid dynamic similarity requires similar non-dimensional velocity fields through the two turbomachines under investigation, and this implies certain fixed values of the non-dimensional flow coefficient (2.1), the work coefficient (2.4) and the pressure rise or head coefficient (2.8) [36]. The non-dimensional flow coefficient can be defined as

$$\phi = \frac{\dot{V}}{Au} = \frac{\dot{m}}{\rho A u} = \frac{c_m}{u} = \frac{c_m}{r\omega}. \tag{2.1}$$

A high flow coefficient implies that the meridian velocity c_m is higher than the impeller reference speed u. The impeller blades in this case spread a short way around the impeller circular line. Defining the flow coefficient as

$$\phi = \frac{\dot{V}}{d^2 u} = \frac{\dot{m}}{\rho d^2 u} \tag{2.2}$$

characterizes the swallowing capacity of different machines through a virtual area $A = d^2$ with the velocity of the reference blade speed and a reference density and considering the continuity equation $\dot{m} = A c_m \rho$.

The non-dimensional work coefficient characterizes the dynamic effects of the impeller rotational speed on the total enthalpy rise. It is based on the enthalpy change but is called a work coefficient. The first law of thermodynamics

$$w_{12} + q_{12} = h_2 - h_1 + \frac{1}{2}(c_2^2 - c_1^2) + g(z_2 - z_1) \tag{2.3}$$

shows that the total enthalpy change in an adiabatic flow ($q_{12} = 0$) is the same as the specific work ($w_{12} = h_{t2} - h_{t1}$), when neglecting the change in potential energy ($z_1 = z_2$). The work coefficient is defined by

$$\lambda = \frac{w_{12}}{u^2} = \frac{h_{t12}}{u^2}. \tag{2.4}$$

Based on change in angular momentum ($T_m = D_2 - D_1 = \dot{m}r_2c_{u2} - \dot{m}r_1c_{u1}$) the turbine's work (Euler's equation) can be written as follows

$$w_{12} = \frac{(D_2 - D_1)\omega}{\dot{m}} = u_2c_{u2} - u_1c_{u1} \tag{2.5}$$

where u_1 and u_2 are the circumferential speeds at radii r_1 and r_2 respectively and c_{u1} and c_{u2} are the circumferential components of the absolute velocities. Therefore, also a work coefficient based on Euler's equation (2.5) can be defined as

$$\lambda_{Euler} = \frac{w_{12}}{u_2^2} = \frac{c_{u2}}{u_2} - \frac{u_1}{u_2}\frac{c_{u1}}{u_2}. \tag{2.6}$$

In a real turbine the theoretical potential for doing work is reduced by the dissipation losses (mixing, secondary flows, leakage, friction on walls, etc.). The pressure rise coefficient or head coefficient is used to characterize this effect and is defined in a similar way to the work coefficient (2.4) whereby there are two common forms, the polytropic head coefficient 2.7 or the isentropic head coefficient 2.8.

$$\psi_p = \frac{\lambda}{\eta_p} \quad \text{Turbine polytropic head coefficient} \tag{2.7}$$

$$\psi_s = \frac{\lambda}{\eta_s} \quad \text{Turbine isentropic head coefficient.} \tag{2.8}$$

A higher pressure drop is needed to overcome the dissipation losses in turbines, so the pressure coefficient characteristic (2.8) lies above that of the work coefficient (2.4), while in compressors the frictional dissipation causes a lower pressure rise than that in the ideal machine. Accordingly the pressure rise characteristic lies below the work characteristic. Moving away from the turbines design point (i.e. point with highest efficiency), which means more or less mass flow through the system, the efficiency decreases in both directions, with can be seen in Figure 6.7 and Figure 7.9 and it is this feature that leads to the typical curvature of pressure versus flow performance characteristics, called turbine or compressor map.

2.1.3 Thermodynamic Similarity

Similar thermodynamic behavior means same temperature ratio T_{t2}/T_{t1}, same pressure ratio p_{t2}/p_{t1} and same density ratio ρ_{t2}/ρ_{t1} in two turbomachines. Assuming adiabatic flow ($q_{12} = 0$) the density and pressure ratio in a turbine can be described as

$$\frac{\rho_{t2}}{\rho_{t1}} = \left(\frac{T_{t2}}{T_{t1}}\right)^{\frac{1}{n-1}} = \left(1 - \frac{h_{t12}}{c_p T_{t1}}\right)^{\frac{1}{n-1}} \tag{2.9}$$

and

$$\frac{p_{t2}}{p_{t1}} = \left(\frac{T_{t2}}{T_{t1}}\right)^{\frac{n}{n-1}} = \left(1 - \frac{h_{t12}}{c_p T_{t1}}\right)^{\frac{n}{n-1}} \tag{2.10}$$

where c_p is the specific heat capacity, n is the polytropic exponent and $T_{t2} = T_{t1} - \frac{h_{t12}}{c_p}$. This shows that the relevant non-dimensional parameter for similar density and pressure ratios in two turbines is $h_{t12}/c_p T_{t1}$, which further can be simplified to

$$\frac{h_{t12}}{c_p T_{t1}} = \frac{\lambda u^2}{c_p T_{t1}} = \frac{(\kappa - 1)\lambda u^2}{\kappa R T_{t1}} \propto M_u^2 \tag{2.11}$$

where $\lambda = \frac{h_{t12}}{u^2}$ and $c_p = \frac{\kappa R}{\kappa - 1}$. For similar thermodynamic behavior of the flow in two turbomachines operating with dynamic similarity (i.e. same work coefficient), the tip-speed Mach number $M_u = u/\sqrt{\kappa R T_{t1}}$ is the relevant dimensionless parameter, whereby the isentropic and polytropic exponents also need to be the same in the two cases [36].

2.1.4 Further Non-Dimensional Parameters

Four mandatory parameters are required to define a single-stage turbomachinery application, namely volume flow rate, pressure rise, rotor diameter and rotational speed. On the basis of these four parameters, four different dimensionless coefficients can be defined. The volume flow rate has been introduced in (2.2) while the pressure rise coefficient has been defined in (2.8). The specific speed and specific diameter are alternative dimensionless coefficients based on the same data, which are chosen to represent the non-dimensional speed and size of the impeller for a certain pressure rise and volume flow rate.

The characteristic parameters volume flow $\dot{V}$, isentropic total head rise h_{ts} and angular velocity ω or the turbine diameter respectively can be fined in the non-dimensional parameters specific speed

$$\omega_s = 2\frac{\phi^{\frac{1}{2}}}{\psi^{\frac{3}{4}}} = \omega\frac{\sqrt{\dot{V}}}{(h_{t12})^{\frac{3}{4}}} \tag{2.12}$$

and specific diameter

$$d_s = \frac{\psi^{\frac{1}{4}}}{\phi^{\frac{1}{2}}} = d\frac{(h_{t12})^{\frac{1}{4}}}{\sqrt{\dot{V}}}. \tag{2.13}$$

These parameters are composed of the flow coefficient ϕ and pressure coefficient ψ and therefore are also non-dimensional. The combination of specific speed and specific diameter can be shown in the Cordier diagram. Well designed axial machines have high specific speed and low specific diameter, whereas good radial machines have low specific speed and high specific diameter [40]. There are no feasible designs of turbomachines with high specific speed and high specific diameter, and none with low specific speed and low specific diameter.

The work coefficient and the flow coefficient can be usefully combined to define the mechanical turbine power

$$P_m = \dot{m}h_{t12} = \frac{\dot{m}}{u_2 d_2^2}\frac{h_{t12}}{u_2^2}u_2^3 d_2^2 = \rho\phi\lambda u_2^3 d_2^2 = \frac{1}{8}\rho\phi\lambda\omega^3 d_2^5 \tag{2.14}$$

and the mechanical turbine torque

$$T_m = \frac{P_m}{\omega} = \frac{1}{8}\rho\phi\lambda\omega^2 d_2^5. \tag{2.15}$$

2.2 Scaling

There are two reasons for downscaling electrically driven turbomachines. Firstly, in high power applications the power density can be increased with modularization and secondly, new emerging applications demand compressors with lower mass flow at high pressure ratios.

2.2.1 Power Density of Electrically Driven Turbomachines

In 2.14 is shown that the power (P) in turbomachinery is proportional to the square of the rotor diameter (d)

$$P \propto d^2. \tag{2.16}$$

The power density (P/V) of turbomachinery is therefore inversely proportional to the rotor diameter (d)

$$\frac{P}{V} \propto \frac{1}{d}. \tag{2.17}$$

This implies that a conventional turbomachine with a certain output power can get replaced with a number of smaller units which have all together the same total output power but a smaller overall volume. This scaling implies constant surface speed, which means, that the rotational speed scales inversely proportional with the diameter d, shown in (2.19). However, this is not fully accurate, as a major condition for scaling of turbomachinery is a constant Reynolds number. The Reynolds number is proportional to the fluid velocity in the flow channel c and the height of the air flow channel d_h, and can be calculated as

$$Re = \frac{c d_h}{\nu} \tag{2.18}$$

where ν is the kinematic viscosity. In small machines the Reynolds number becomes so small that higher frictional losses occur and therefore scaling to small sizes inevitably causes a loss in efficiency. Correction equations for the effect of a change in Reynolds number on efficiency have been presented in [41], [42] and [43]. Since the Reynolds number decreases with miniaturization and does not remain constant, the power density increases with less than $1/d$. As an example, one large turbo-compressor can be replaced with 16 compressors, each with a volume of 1/64 of the conventional compressor, which together has the same output power but requires only a quarter of the volume of the conventional compressor. The diameter of the small units would be 1/4 of the original one and the rotational speed would therefore increase by a factor of at least 4. This scaling is only true under the assumption that only the active parts of the turbomachinery and the electrical machines are taken into account, but not the inactive parts, like housing of the turbomachinery and the electrical machine, the power electronics and air flow channels for cooling.

The power density of electrical machines scales with speed

$$\frac{P}{V} \propto n. \tag{2.19}$$

Therefore, the overall volume of the electrical machines in the example above is also $\frac{1}{4}$ of the original one. In contrast to electrical machines, the size of the power electronics mainly scales with the power rating and is minimized by choosing the correct topology, through efficiency improvements and the use of high switching frequencies in order to reduce the volume of passive components. For systems with high power ratings, the size of the control electronics is negligible compared to the power electronics. However, for ultra-high-speed machines with low power ratings (i.e. 100 W to few kilowatts), the control electronics size becomes significant. Generally, the size of the control electronics scales with the complexity of the control method selected and the complexity depends on the topology and the modulation schemes used.

2.2.2 Electrically Driven Turbomachines with High Pressure Ratios at Low Flow Rates

The requirements for turbocompressors, like the Solar Impulse cabin air pressurization system [34], but also for other applications such as heat pumps and fuel cell compressors, demand low flow rates (i.e. 1 g/s to 30 g/s) at relatively high pressure ratios (i.e. 1.3 to 3). Downscaling of a macro turbomachine for constant specific speed (2.12) and lower volume flow (assuming constant isentropic total head rise) therefore leads to an increase in rotational speed.

2.3 Turbine Comparison

There are several options for the turbine for a compressed-air-to-electric-power system which are compared concerning size, efficiency, rotational speed, and simplicity of manufacturing.

2.3.1 Single-Stage Axial Impulse Turbine (Laval Turbine)

In impulse turbines, the drop in pressure (expansion) of pressurized air takes place only in the stationary nozzles and not between the moving rotor blades ($p_1 \approx p_2$). This is obtained by making the blade passage of constant cross-sectional area. The nozzle vanes produce a jet of air of high velocity and the blades change the direction of the jet, thus producing a change in momentum and a force that propels the blades. Characteristic for this type of turbine is the big deflection in the nozzle guide vanes and therefore small angle α_1 and the same input and output rotor angle, e.g. $\beta_1 = \beta_2$ and $|w_1| = |w_2|$, see Figure 2.4. Advantages of an impulse turbine are the small leakage losses because of the small pressure gradient over the rotor blades, lower rotational speed compared to the reaction turbine and a minimal axial thrust which results in low friction losses in the bearings. A further advantage of this turbine type is the simple construction and the possibility to use a shrouding band, which would lead to a higher efficiency. Disadvantages of an axial turbine are the high losses in the nozzle guide vanes because of the high acceleration of the pressurized air, and the rotor blade losses because the air is highly deflected. These main disadvantages lead to lower efficiencies than for reaction and radial turbines. The specific work can be written with Euler's equation as

$$w_{12} = u_{rm}(c_{u2} - c_{u1}) = -u_{rm}c_{u1} = -2u_{rm}^2 \qquad (2.20)$$

while the theoretical non-dimensional Euler work coefficient (2.6) for an impulse turbine can be written as

$$\lambda_{Euler} = \frac{w_{12}}{u_{rm}^2} = \frac{c_{u2}}{u_{rm}} - \frac{c_{u1}}{u_{rm}} = -\frac{c_{u1}}{u_{rm}} = -2 \qquad (2.21)$$

where u_{rm} is the circumferential speed at radius r_m and $c_{u1} = 2u_{rm}$ and $c_{u2} = 0$ are the circumferential components of the absolute velocities.

2.3.2 Single-Stage Axial Reaction Turbine

In reaction turbines a part of the expansion of compressed air takes place between the rotor blades, e.g. the degree of reaction of a stage can be written as

$$r_k = \frac{\Delta h_{rotor}}{\Delta h_{stage}} = \frac{h_1 - h_2}{h_0 - h_2} = \frac{h_{t02} - 1/2(c_2^2 - c_1^2)}{h_{t02}}. \tag{2.22}$$

For a reaction of 50% the expansion takes place in equal shares in the stationary nozzle guide vanes and between the rotor blades, resulting in congruence of input and output velocity diagrams. Drawbacks of a reaction turbine are the additional friction losses in the bearings, because of additional axial thrust due to the pressure gradient over the rotor blades and the more complex construction. Advantages are the better efficiency and also the possibility of adding a shrouding band. The specific work for a reaction turbine of 50% can be written with Euler's equation

$$w_{12} = u_{rm}(c_{u2} - c_{u1}) = -u_{rm}^2 \tag{2.23}$$

while the theoretical non-dimensional Euler work coefficient (2.6) for a 50% reaction turbine can be written as

$$\lambda_{Euler} = \frac{w_{12}}{u_{rm}^2} = \frac{c_{u2}}{u_{rm}} - \frac{c_{u1}}{u_{rm}} = -\frac{c_{u1}}{u_{rm}} = -1 \tag{2.24}$$

where u_{rm} is the circumferential speed at radius r_m and $c_{u1} = u_{rm}$ and $c_{u2} = 0$ are the circumferential components of the absolute velocities. In order to get the same work, i.e. to meet the relationship $2u_{rm,r=0}^2 = u_{rm,r=0.5}^2$ the peripheral speed of the 50% reaction turbine must be $\sqrt{2}$ times the peripheral speed of the impulse turbine, which reduces the lifetime of the high-speed ball bearings.

2.3.3 Inward-Flow Radial Turbine

Concerning efficiency, the radial turbine is the best choice, but there are some major disadvantages: For low flow rates the blade height of the turbine (< 0.5 mm) or the turbine diameter (< 1 cm) gets very small. This leads to expensive turbines which are difficult to manufacture. Also the curved geometry of the rotor blades, the spiral casing and the radial outlet lead to a difficult production. Due to the higher rotational speed the lifetime of the bearing is reduced. A system with an inward-flow radial turbine based on the reversal of an existing electrically driven radial compressor is presented in section 7.

2.3.4 Reciprocating Systems

Theoretically, a reciprocating engine or a Wankel-type engine could be used instead of an axial- or radial turbine. However the disadvantages like the piston lining, lubrication, vibrations and the rather low speed (i.e. the big size of the generator) are dominant such that this approach is not a serious option.

2.3.5 Turbine Selection

Due to simplicity, size, lower rotational speed and a minimal axial thrust a single-stage axial impulse turbine has been chosen for the compressed-air-to-electric-power system. However, in section 7 also a system with a radial turbine and higher electric output power has been tested and characterized. The comparison, including systems reported in literature, is presented in section 7.5.

2.4 Turbine Design

The dimensioning of turbines as well as compressors starts with the preliminary design in which the required demands and the aerodynamic data of the compressor are studied, usually on a largely empirical and 1D basis, resulting in geometrical dimensions and efficiency estimation through correlations. The 1D design is then followed by a 2D iterative streamline curvature method as described in [44], based on fundamental design equations (continuity equation, energy equation, momentum equation, etc.) and empirical correlations to model friction losses, boundary layer displacement, and flow deviation relative to the blade. This allows a more rapid consideration of the design issues before moving on. For further aerodynamic improvements the dimensioning is then followed by extensive and time-consuming three-dimensional computational fluid dynamics (3D CFD) analysis and geometry optimization.

2.4.1 Enthalpy Entropy Diagram

Turbomachines are generally designed to work efficiently over only a relatively limited range of supply pressures and rotational speeds. Especially the rotational speed has a significant influence on the turbine efficiency, as can be seen in Figure 6.7. To be able to operate the turbine at highest efficiencies, the mass flow and therefore the rotational speed of the turbine must be controlled with a throttling valve, depending on the variable and unpredictable load.

A thermodynamic model in terms of an enthalpy entropy diagram is given in Figure 2.1, including a throttling valve. The y-axis indicates enthalpy h, or the temperature since $h = c_p T$, which represents the available internal energy plus flow work of the fluid to be converted into useful work ($h = u + c^2/2$). The x-axis indicates entropy s which, for an adiabatic system, is related to the work dissipated or lost due to irreversibility. Only the expansion through the turbine produces useful work, whereas the pressure drop through the throttle valve gives an increase of entropy, by generating a pressure drop by dissipation.

2.4.2 Free Nozzle Discharge

The mass flow through the nozzle guide vanes and the turbine can be modeled as a free discharge from a pressure-vessel like considered in [45] and schematically shown in Figure 2.2, thereby representing the compressed air flow as a huge reservoir, e.g. constant pressure p_0 and temperature T_0, from which air discharges trough a nozzle into the atmosphere. The equation for the velocity of the air at the cross-section of the nozzle where the pressure is p_1 can be found with the Bernoulli equation. In the case of a lossless consideration of a steady flow with significant change in volume and performing an external work, the Bernoulli equation can be written as

$$-\int_0^1 v dp = \frac{1}{2}\left(c_1^2 - c_0^2\right) + g(z_1 - z_0) + W_{01}. \tag{2.25}$$

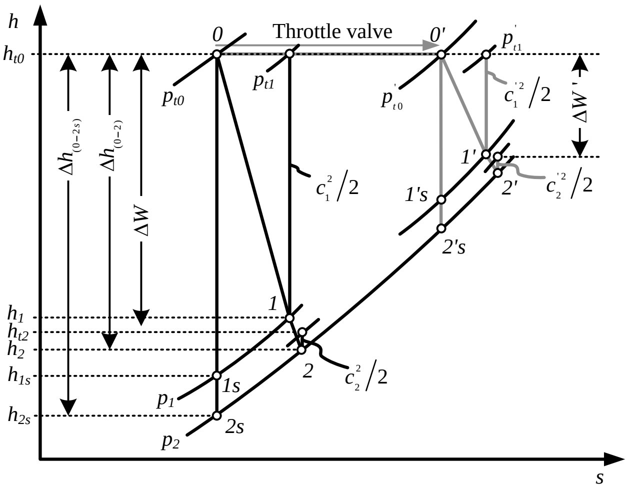

Figure 2.1: *Enthalpy entropy diagram (hs-diagram) of the compressed-air-to-electric-power system without valve (black) and with valve (grey). In the case of an impulse turbine the specific work can be written with Euler's equation* (2.5) *as:* $\Delta w = u_{rm}(c_{u2} - c_{u1}) = -u_{rm}c_{u1} = -2u_{rm}^2$.

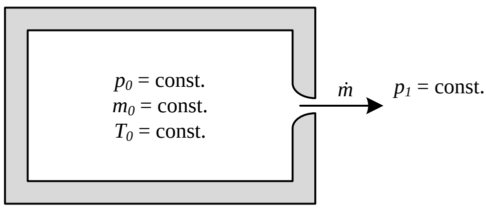

Figure 2.2: *Free discharge from a pressure-vessel from which air escapes into the atmosphere.*

The equation can be simplified for the special case of nozzle guide vanes, i.e. it can be assumed that no work is done ($W_{01} = 0$), the change in potential energy can be neglected ($z_0 = z_1$), further can be assumed that the velocity in the reservoir is zero, e.g. $c_0 = 0$. The assumption that there is no heat exchange ($q_{01} = 0$) and no losses, gives the isentropic relationship $p \cdot v^{\kappa} = const$, which can be substituted into $-\int_0^1 vdp$ in (2.25) which then can be solved for the velocity c_1.

The mass flow rate which describes the free discharge from a vessel can then be calculated with

$$\dot{m} = A\frac{p_0}{\sqrt{RT_0}}\Psi. \tag{2.26}$$

The derivation of (2.26) is described in appendix A. The function Ψ separates the cases of choked flow, i.e. when sonic conditions are reached in the flow channels, and subsonic condition, e.g. no choking occurs. The flow function Ψ for subsonic flow ($1 \geq \frac{p_1}{p_0} > \Pi_{crit}$) can be expressed as

$$\Psi = \sqrt{\frac{2\kappa}{\kappa - 1}\left[\left(\frac{p_1}{p_0}\right)^{\frac{2}{\kappa}} - \left(\frac{p_1}{p_0}\right)^{\frac{\kappa+1}{\kappa}}\right]} \tag{2.27}$$

and for choked flow ($\Pi_{crit} \geq \frac{p_1}{p_0}$) the flow function is given by

$$\Psi_{max} = \left(\frac{2}{\kappa + 1}\right)^{\frac{1}{\kappa-1}}\sqrt{\frac{2\kappa}{\kappa + 1}} = 0.685 \tag{2.28}$$

whereas the critical pressure ratio $\frac{p_{1max}}{p_0}$ is given by

$$\Pi_{crit} = \frac{p_{1max}}{p_0} = \left(\frac{2}{\kappa + 1}\right)^{\frac{\kappa}{\kappa-1}} = 0.528. \tag{2.29}$$

This pressure ratio is called the critical pressure ratio because the air velocity reaches sonic speed in the nozzle. A further reduction of the pressure ratio ($p_0 = const$) does not increase the velocity or the mass flow rate, the flow is choked. The flow function Ψ is plotted in Figure 2.3 for a constant vessel pressure p_0 and a varying outlet pressure $p_2 \leq p_0$.

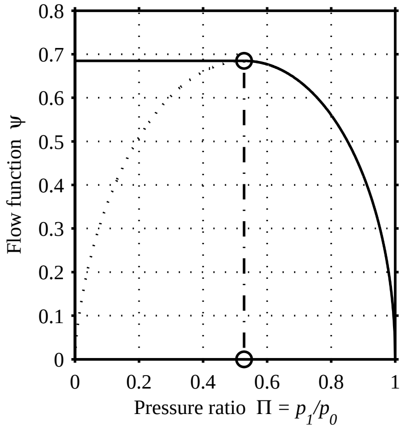

Figure 2.3: *Flow function Ψ for air with $\kappa = 1.4$, where p_0 is the inlet pressure and p_1 the pressure between nozzle and turbine. Marked are the critical pressure ratio $\Pi_{crit} = 0.528$ and the corresponding maximal flow function $\Psi_{max} = 0.685$.*

2.4.3 1D-Impulse Turbine Design

Assuming adiabatic and isentropic flow ($q_{02} = 0$ and $T \cdot p^{\frac{1-\kappa}{\kappa}} = const$) through the turbine, the corresponding ideal enthalpy temperature can be calculated as

$$T_{2s} = T_0 \left(\frac{p_{t0}}{p_2}\right)^{\frac{1-\kappa}{\kappa}} = 219.2 \text{ K} \tag{2.30}$$

and the ideal enthalpy temperature drop as

$$\Delta T_{(0-2s)} = T_0 - T_{2s} = T_0 \left[1 - \left(\frac{p_{t0}}{p_2}\right)^{\frac{1-\kappa}{\kappa}}\right] = 80.8 \text{ K} \tag{2.31}$$

with $p_{t0} = 300$ kPa, $p_2 = 100$ kPa and $T_0 = 300$ K. For the real expansion the increase of entropy, i.e. losses, must be considered. The isentropic efficiency η_s was assumed to be 30%, which leads to an actual temperature drop over the impulse turbine of

$$\Delta T_{(0-2)} = \Delta T_{(0-2s)} \eta_s = 24.2 \text{ K} \tag{2.32}$$

and to the theoretical mass flow of

$$\dot{m} = \frac{P_m}{c_p \Delta T_{(0-2s)} \eta_s} = 2.5\ \frac{\text{g}}{\text{s}} \tag{2.33}$$

where c_p is the specific heat capacity and the mechanical power $P_m =$ 60 W.

Although in an impulse turbine the pressure drop takes place only in the stationary nozzle and not between the moving rotor blades ($p_1 \approx p_2$) the pressure between nozzle and turbine (p_1) was assumed to be 120 kPa. Therefore the corresponding ideal enthalpy temperature drop $T_{(0-1s)}$ can be calculated as

$$\Delta T_{(0-1s)} = T_0 \left[1 - \left(\frac{p_{t0}}{p_1} \right)^{\frac{1-\kappa}{\kappa}} \right] = 69.1\ \text{K} \tag{2.34}$$

and the absolute nozzle outlet velocity c_1 as

$$c_1 = \eta_n \sqrt{\Delta T_{(0-1s)} c_p 2} = 335\ \text{m/s} \tag{2.35}$$

while the nozzle guide vanes efficiency η_n is assumed to be 90%. The relatively large absolute velocity $c_1 = 335$ m/s is near the sonic speed. The effective turbine inlet area A (and thereby the radii r_1, r_2 and r_3) can be calculated with the flow function, described in 2.27. Furthermore, the velocity diagram at rotor entry and rotor outlet can be calculated as shown in Figure 2.4.

Due to the fact that the selected turbine type is an impulse turbine, the pressure drop, i.e. the acceleration of the air, fully takes place in the nozzle guide vanes. This means that the outer inlet area decreases, i.e. the radius r_1 reduces to r_2, while r_3 remains constant, and the nozzle guide vanes output area equals the turbine inlet area. The second important function of the guide vanes is the deflection of the air stream to the correct angle (α_1), such that the velocity diagram is consistent as shown in Figure 2.4. In Table 2.1 the most important thermodynamic and turbine data are summarized.

All turbomachines suffer from losses associated with the leakage of some fluid around rotors and stators. Tip leakage is driven by the pressure difference between the blade suction and pressure side. Also the

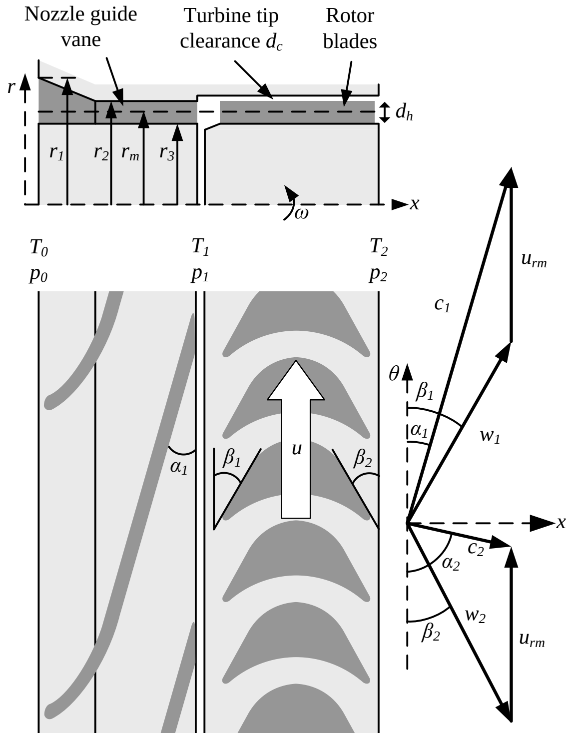

Figure 2.4: *Drawing of the single-stage axial impulse turbine (Laval turbine) with $r_m = 4.5$ mm and the corresponding nozzle guide vanes and velocity diagrams at rotor inlet and outlet for the rated rotational speed. c_1 and c_2 are the absolute velocities at the rotor inlet and outlet. w_1 and w_2 are the relative velocities at the rotor inlet and outlet. u_{rm} is the rotor speed at radius r_m and while $\alpha_1 = 14°$ and $\beta_1 = \beta_2 = 30°$.*

manufacturing tolerances cannot be decreased proportional with the turbine scaling, therefore the leakage losses become more dominant for small turbines. Due to the fact that the rotor blades are only 0.5 mm high, the tip clearance between rotor and casing must be as low as possible. In order to reach small tip clearances, the rotor-impeller assembly requires advanced mass balancing technology. The measurements have been made

Description	Parameter	Value
Inlet temperature	T_0	300 K
Inlet pressure	p_{t0}	300 - 600 kPa
Turbine inlet pressure	p_1	120 kPa
Outlet pressure	p_2	100 kPa
Nozzle guide vanes efficiency	η_n	90%
Isentropic efficiency	η_s	30%
Median radius	r_m	4.5 mm
Rotor blade height	d_h	0.5 mm
Rated speed	n_r	350 000 rpm
Rated stator speed at r_m	u_{rm}	165 m/s

Table 2.1: *Thermodynamic and turbine data.*

with a tip clearance of 0.1 mm ($d_c/d_h = 20\%$), which is clearly too much. For big turbomachinery the tip clearance is in the range of 1% to 2% of the rotor height. Therefore, for the further systems tip clearance must be reduced to values below 10%. As a consequence of miniaturization, the Reynolds number (2.18) will decrease, and therefore the flow will become more laminar. However, in the used axial turbine the Reynolds number is in the range of 11 000, which is still in the area of turbulent air flow.

2.4.4 Computational Fluid Dynamics Simulation

In order to verify the 1D-design from section 2.4.3 a computational fluid dynamics simulation (CFD) has been carried out using ANSYS. In Figure 2.5 the pressure distribution for an input pressure of 300 kPa and for different spans (10%, 50% and 95% of the rotor blade height d_h) in the nozzle guide vanes and the turbine is shown. Regarding the pressure (p_1) between nozzle and turbine, it can be recognized that the assumption ($p_1 = 120$ kPa) for (2.34) was appropriate. In the turbine the pressure side (≈ 150 kPa) and the suction side (100 kPa) can be recognized. The pressure reduction from 300 kPa to ≈ 120 kPa and therefore the increase of the velocity from 0 m/s to ≈ 330 m/s in the nozzle guide vanes can be seen in Figure 2.5 and Figure 2.6. Furthermore, the airflow at rotor outlet is not diverted by $\beta_2 = 30$, as supposed in the 1D-design in Figure 2.4.

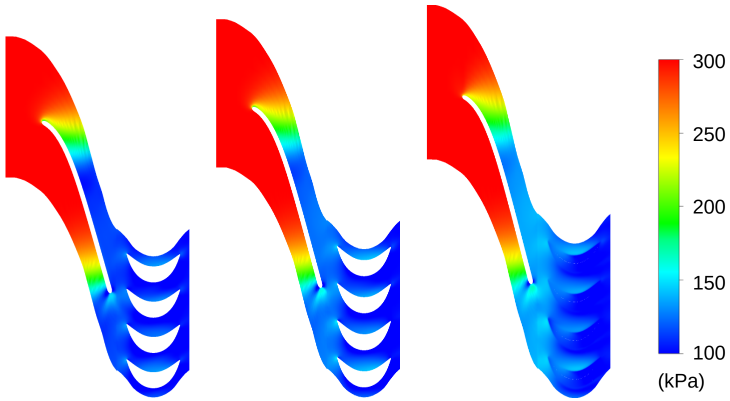

(a) (b) (c)

Figure 2.5: *CFD simulations: pressure span 10% 2.5(a), pressure span 50% 2.5(b), pressure span 95% 2.5(c).*

.

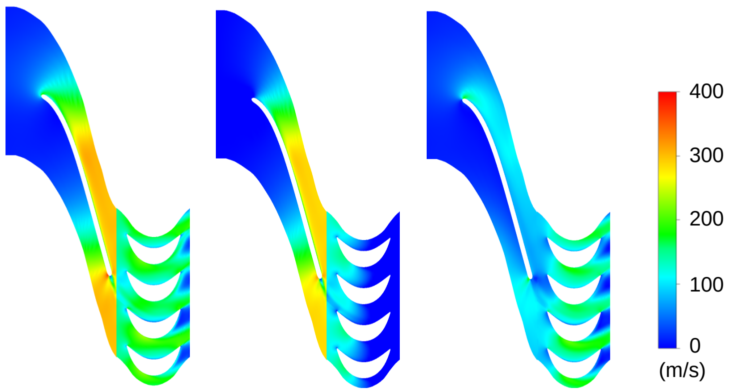

(a) (b) (c)

Figure 2.6: *CFD simulations (span 50%): velocity 2.6(a), circumferential velocity 2.6(b), meridional velocity 2.6(c).*

Chapter 3

Electrical Machine Design and System Integration

The challenges in ultra-high-speed machine design are the mechanical rotor design, especially the stresses in the PM, the minimization of high-frequency losses due to eddy currents and air friction. The additional high-frequency losses in rotor, winding and back-iron are due to increased eddy-current effects and are reduced with an according machine topology with low reaction and no slotting effects (rotor losses), a litz wire winding (copper losses) and a high-frequency stator core material (iron losses). The air friction losses however can only be reduced by decreasing the rotor radius and length, which influences the other loss components. An expanded analysis has been carried out in [46], therefore only a short overview is presented here.

3.1 Electrical Machine Topology

The rotor of the PM generator consists of a diametrically magnetized cylindrical SmCo PM encased in a retaining titanium sleeve ensuring sufficiently low mechanical stresses on the brittle magnet. For a proper rotor construction, the displacement, the radial stress σ_r and the tangential stress σ_θ on the cylindrical magnet and the retaining titanium sleeve must be limited by adjusting the dimensions and the interference fit according to [47]. The eccentricity is minimized by shrink fitting the sleeve onto the PM and grinding of the rotor. The PM generator utilizes two high-speed ball bearings due to its simplicity and small size (inner diameter: 3.175 mm, outer diameter: 6.35 mm, $l = 2.8$ mm). The back end ball bearing is assembled at the end of the rotor, while the front end ball bearing lies between the PM and the turbine. Because the turbine can easily be disassembled with a thread at the front end of the rotor, replacing the front end ball bearing can be carried out easily for the compressed-air-to-electric-power system in chapter 6, unlike the reversal of the one-stage radial compressor from section 7, where the turbine is shrink fitted or glued on the rotor. Replacing the front end ball bearing from that system implies drawing-off the impeller and reassembling it after changing the ball bearing.

The stator magnetic field rotates with high frequency (5.83 kHz); it is therefore necessary to minimize the losses in the stator core by using amorphous iron. In order to minimize the eddy current losses in the copper wires, the three-phase skewed air-gap winding is realized with litz wires. In Figure 3.1 a cross section view of the PMSM is shown, while in Figure 3.2 the non-casted stator and rotor is presented. The compressed-air-to-electric-power generator has a peak phase-to-phase voltage of 20.2 V at 350 000 rpm. The measured electrical machine efficiency η_m at rated power output is 88% including air friction and bearing losses. A detailed description of the generator has been presented in [48] and [28] while in Table 3.1 the rated and measured electrical data of the PM generator is summarized. In [49] the speed limitations of PM machines and the correlation between the limits and machine parameters are presented. The focus of [49] is on the thermal limits, the elastic properties of the materials used in the rotor (e.g. strength or stress limits), and rotordynamics limits.

The generator losses can be divided into the current dependent resistive copper losses $P_{Cu,s}$ (including the influence of the skin effect), the proximity effect losses $P_{Cu,p}$ (eddy-current losses due to an external magnetic field), the iron losses P_{Fe} and the air friction losses P_{Air}. A detailed explanation is presented in [50] and [46], therefore only a short overview including the main equations is shown here. The magnetic field is practically independent of the stator current, and therefore are eddy-current losses due to the external magnetic field (proximity effect losses) only dependent on speed. However, the current harmonics also influence the

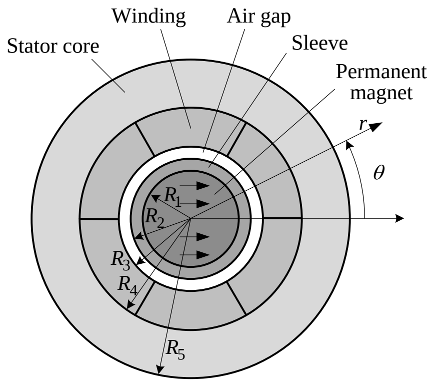

Figure 3.1: *Electrical machine cross-section: Diametrically magnetized cylindrical PM rotor encased in a retaining titanium sleeve inside a slotless stator existing of a three-phase skewed air-gap winding realized with litz wire and an amorphous iron stator core (*$R_1 = 5.9$ mm, $R_2 = 6.4$ mm, $R_3 = 6.8$ mm, $R_4 = 10$ mm, $R_5 = 14$ mm*).*

Figure 3.2: *Hardware realization: Rotor with PM encased in titanium sleeve, stator with amorphous iron core and litz-wire air-gap winding.*

magnetic field in the machine, this is referred as armature reaction, and especially high frequency harmonics can lead to additional eddy current losses in stator core and rotor sleeve. Due to the low armature reaction of this machine type, the rotor losses can be omitted [48]. Achieving low high-frequency current harmonics is not trivial as the phase inductance of the machine is very low due to the large air gap.

3.1.1 Copper Losses (Ferreira Method)

The copper losses consist of the current dependent resistive losses $P_{Cu,s}$ in the stator winding, which include the influence of the skin effect, and of the proximity effect losses $P_{Cu,p}$, which are mainly due to the eddy currents induced by the magnetic field of the PM. The copper losses can be expressed as

$$P_{Cu} = P_{Cu,s} + P_{Cu,p} = I^2 F + G \frac{\hat{H}^2}{\sigma_{Cu}} \tag{3.1}$$

where I is the rms stator current, $\hat{H}$ is the peak magnetic field strength in the winding, and σ_{Cu} is the conductivity of the conductors. The coefficients F and G include the effects of the eddy currents, and are calculated based on the frequency, the conductivity, and the geometry of the winding arrangement. The Ferreira method [51] was chosen for calculating the coefficients in this thesis.

3.1.2 Iron Losses

For high-frequency material, such as ferrites, soft-magnetic powders and amorphous or nanocrystalline iron-based alloys, the Steinmetz equation [52] is the most commonly used method to calculate the iron losses. The iron flux distribution and waveform is sinusoidal, such that the original Steinmetz equation can be used without correction factors, because armature reaction can be neglected. The iron losses are calculated as an integral over the iron volume with

$$P_{Fe} = \int_{V_{Fe}} C_m f^{\alpha} \hat{B}^{\beta} dV \tag{3.2}$$

Description	Parameter	Value
Rated speed	n_r	350 000 rpm
Maximal speed	n_{max}	500 000 rpm
Rated electric output	P_{el}	60 W
Rated torque	T_r	1.6 mNm
Permanent magnet diameter	R_1	5.9 mm
Rotor diameter	R_2	6.4 mm
Inner Winding diameter	R_3	6.8 mm
Outer Winding diameter	R_4	10 mm
Outer stator core diameter	R_5	14 mm
Permanent magnet length	l_{PM}	11 mm
Litz wire (strands/diameter)	–	158 / 0.03 mm
Inertia	J	$23 \cdot 10^{-9}$ kg m^2
Rated electrical machine temperature	T	60°C
Remanence flux density (Sm_2Co_{17})	B_{rem}	1.04 T
Magnet flux linkage	Ψ_{pm}	0.31 mVs
Back emf at rated speed	u_{emf}	11.4 V
Stator inductance	L_S	2.1 µH
Stator resistance	R_S	0.12 Ω
Rated copper losses	P_{Cu}	1.8 W
Rated iron losses	P_{Fe}	0.5 W
Rated air friction losses	P_{Air}	1.9 W
Rated bearing losses (per Bearing)	P_{Bng}	2 W
Rated total losses		
Without bearing	P_t	8.2 W
With bearing	P_t	12.2 W
Rated electrical machine efficiency		
Without bearing	η_m	93.5%
With bearing	η_m	88.0%

Table 3.1: *Rated and Measured compressed-air-to-electric-power generator data.*

where f is the frequency and $\hat{B}$ the peak magnetic flux density. The parameters for the amorphous iron used (Metglas 2605SA1) are: relative permeability $\mu_r = 35100$ and the Steinmetz coefficients $C_m = 0.94$ W/m^3, $\alpha = 1.53$ and $\beta = 1.72$. A calculated distribution of the flux density in the generator is presented in Figure 3.3, according to [53].

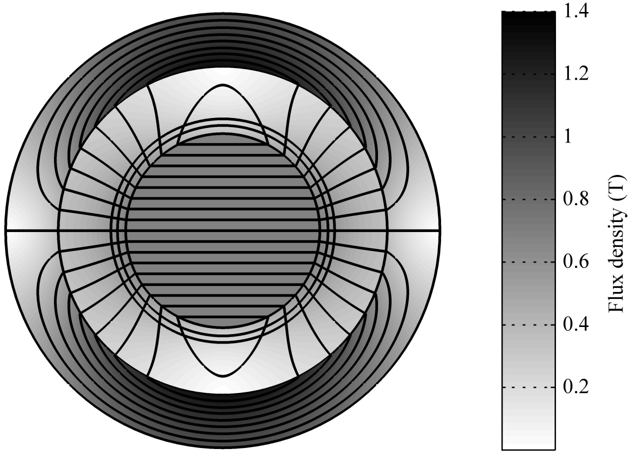

Figure 3.3: *Calculated distribution of the flux density in the generator, according to [53].*

3.1.3 Air Friction Losses

According to [54], the air friction losses of a long rotating cylinder encased in a stationary hollow cylinder are

$$P_{Air} = c_f \pi \rho_{air} \omega^3 R_2^4 L \tag{3.3}$$

where ρ_{air} is the density of the air, ω the angular speed, R_2 the radius of the cylinder, and L the length of the cylinder. The air friction coefficient c_f depends on the radius of the cylinder, the air gap δ, and the Reynolds and the Taylor number.

3.2 Optimization Process

The PMSM has been optimized for lowest losses, regarding several constraints, i.e. maximal active length, maximal iron outer diameter, minimal sleeve thickness, minimal air gap, etc. For this reason, an optimization method has been developed which takes air friction losses, iron losses, copper losses, and eddy current losses into account [53]. The electrical machine has been optimized for a rated power of 60 W at 350 000 rpm. In Figure 3.4 the computed efficiency (including bearing losses) of the generator in the entire power-speed plane is shown.

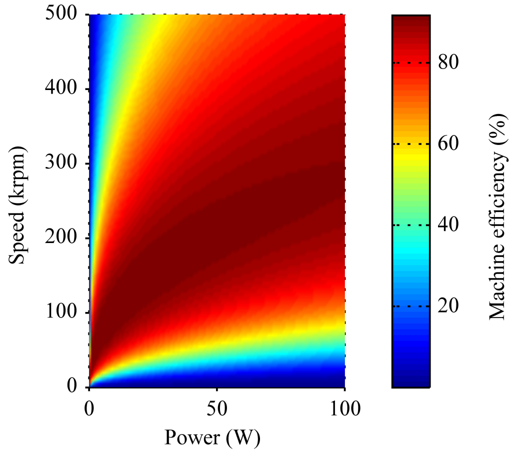

Figure 3.4: *Computed efficiency of the generator between an operating speed of 0 rpm and 500 000 rpm and an output power between 0 W and 100 W, while including bearing losses.*

In Figure 3.5 motor optimizations for five different electric output power values have been accomplished, namely for 20 W, 40 W, 60 W, 80 W and 100 W. It can be seen, that for a certain deviation from the optimized point, the design is still the best choice, but with increasing deviation the losses increase and a PMSM in the next following optimization point becomes more suitable. Since the PMSM should have lowest losses over a power range from zero to 100 W (this is especially important for an application like on industrial robots, section 1.2.5), the mean

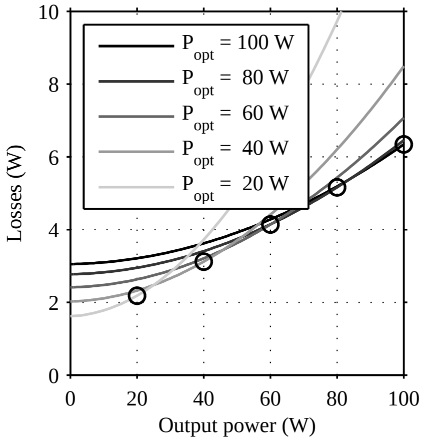

Figure 3.5: *Generator losses (neglecting bearing losses) for five different electric output power optimization points (20 W, 40 W, 60 W, 80 W and 100 W) and a rotational speed of 350 000 rpm.*

power losses of the mentioned range must be considered, which leads to a PMSM that is optimized for 60 W, which has in average 4 W total losses when neglecting bearing losses.

3.3 System Integration

The design of the compressed-air-to-electric-power system has been carried out in a modular approach; it is possible to operate the system with and without an additional throttling valve. In this section only the construction including turbine and generator is explained, while in section 5.1 the design and assembly of the used throttling valve is depicted, and in section 6.4 experimental results of the autonomous system including the valve are presented.

3.3.1 Air Flow

In Figure 3.6 a cut-away view of the of the compressed-air-to-electric-power system is presented. The compressed air enters through a com-

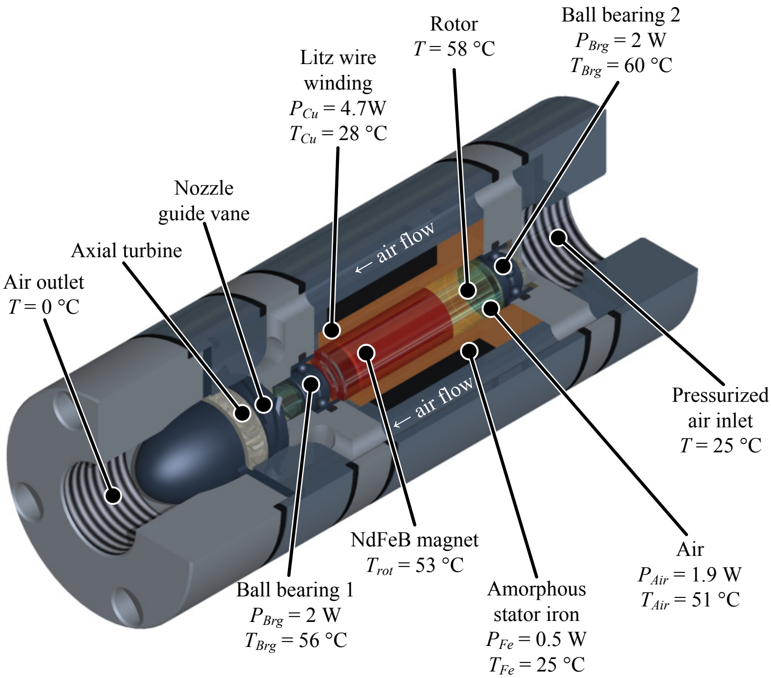

Figure 3.6: *3D-solid model of the ultra-compact (22 mm × 60 mm) high-speed compressed-air-to-electric-power demonstrator, indicating power losses and resulting temperatures (calculated with the thermal model presented in Figure 3.9) for an operating point of 350 000 rpm and 100 W electric output power.*

mon pneumatic connector that can be screwed into the system on one side. The pressurized air then gets diverted into eight channels that are arranged symmetrically in the generator casing and the ball bearing shields (indicated with arrows in Figure 3.6). This leads to higher effort in the construction of the casing, but the generator and the ball bearings can be cooled and as a positive side effect, the inlet air gets heated up which leads to higher outlet air temperature and therefore less problems with dew point and icing. Calculations show that the temperature rise due to waste heat from the generator is in the range of 5 K. The pressurized inlet air then reaches the nozzle guide vanes. In the first part of the nozzle guide vanes the area is decreased to the effective turbine area and thereby the pressurized air is accelerated and the pressure drops to almost outlet pressure. In the second part the accelerated air is diverged to the angle α_2. The air then passes through the turbine and leaves the system on the left hand side to the environment. A detailed view of the air flow in the nozzle guide vanes and the turbine can be seen in Figure 2.4 and Figure 6.2.

3.3.2 Rotor Dynamics

In order to run the system in between two critical speeds, the critical speeds of the rotor and turbine assembly are determined with finite element simulations. The spring constant of the bearing system is taken into account, which shifts the critical speeds to lower frequencies. The length of the shaft is adjusted such that rated speed (350 000 rpm, 5833 Hz) falls between the second (285 420 rpm) and the third (723 900 rpm) critical speed (Figure 3.7). In Figure 6.2 a picture of the axial impulse turbine and rotor with assembled high speed bearings is shown. Due to the gyroscopic effect the critical speeds, which are usually plotted in the Campbell diagram as function of the rotational speed, are speed dependent as presented in Figure 3.8. The resulting gyroscopic torque is either accelerating or breaking, which leads to the so called backward or forward whirl. The intersection of the speed dependent resonant frequency with the identity line leads to the critical speeds. Furthermore, the torsional vibration modes have much higher frequency than the critical speeds and therefore have not been added to the rotordynamic analysis.

3.3.3 Thermal Design

The thermal behavior of the compressed-air-to-electric-power system has been simulated with the analytical model shown in Figure 3.9 at an operating point of 350 000 rpm and 100 W electric output power. For the analytical analysis the casing is assumed to remain at a constant temperature of 25°C. The heat flow in axial direction can be calculated as

$$R_{th,ax} = \frac{l}{\lambda A} \tag{3.4}$$

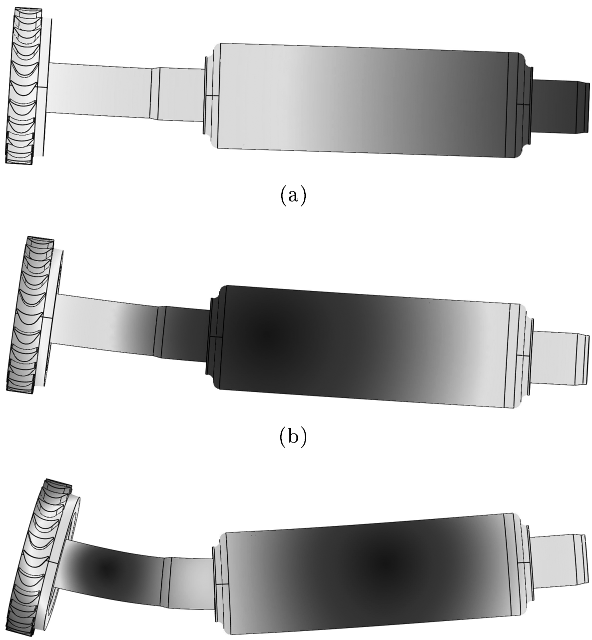

(a)

(b)

(c)

Figure 3.7: *Critical speeds of the compressed-air-to-electric-power rotor including the turbine. First critical speed at 198 840 rpm, 3314 Hz 3.7(a), second critical speed at 285 420 rpm, 4757 Hz 3.7(b) and third critical speed at 723 900 rpm, 12065 Hz 3.7(c). The grey scale shows the displacement: no displacement (black), maximal displacement (white).*

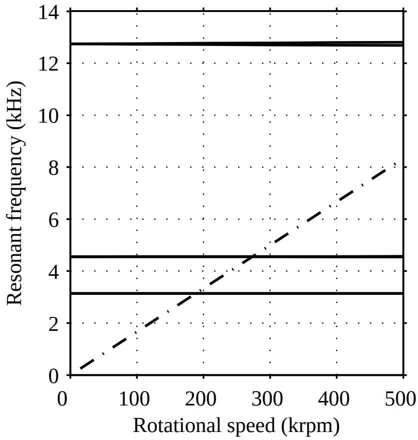

Figure 3.8: *Campbell diagram of the compressed-air-to-electric-power rotor including the turbine. The critical speeds are at the intersection of the rotational speed dependent resonant frequency with the identity line.*

while the heat flow for a hollow cylinder in radial direction can be calculated as

$$R_{th,rad} = \frac{ln(\frac{r_o}{r_i})}{2\pi\lambda l} \tag{3.5}$$

where λ is the heat conductance, l is the length, A is the cross section and r_o and r_i are the inner and outer radius of the hollow cylinder. The heat capacity can be calculated as the integral over the volume

$$C_{th} = \int_V c_{th} dV \tag{3.6}$$

where c_{th} is the specific heat capacity.

Temperature measurements under various load conditions have shown that this condition can be assumed. The main goal in the thermal design is to avoid temperatures above 200°C in the ball bearings, which are mounted with O-rings into two aluminum shields. They are most critical due to the high bearing losses and the poor thermal connection of the bearings to the machine stator. The loss components and the resulting temperatures of the nodes of the thermal model from Figure 3.9 can be found in Figure 3.6, it can be seen that due to the excellent cooling of the casing, also the ball bearing temperatures remain in convenient regions. Ball bearing 1 has a lower temperature (56°C) than ball bearing 2 (60°C) because of the low temperatures that appear while expanding the compressed air over the turbine. Operating the system at 500 000 rpm and 100 W electric output power increases the ball bearing and air friction losses and therefore also leads to higher temperatures in the two ball bearings (102°C and 110°C respectively).

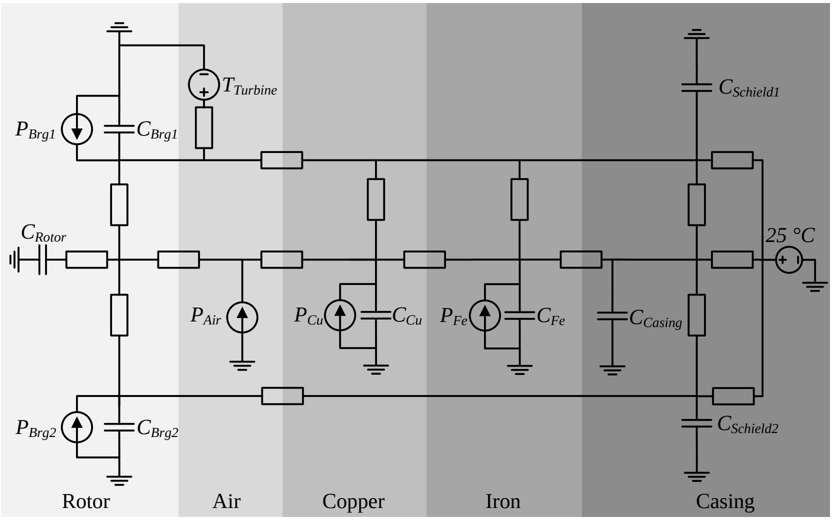

Figure 3.9: *Thermal model of the compressed-air-to-electric-power system. For an operating point of 350 000 rpm and 100 W electric output power the values are as followed:* $P_{Brg1,2} = 2$ W, $P_{Air} = 1.9$ W, $P_{Cu} = 4.7$ W, $P_{Fe} = 0.5$ W *and* $T_{Turbine} = 0$°C.

Chapter 4

Power and Control Electronics

Ultra-high-speed micro gas and air turbines with an electric output power of a couple of watts to a few kilowatts have recently been widely reported in literature [19], [21], [25], [26], [27], [30] and [55]. The main applications for such systems are power supplies in consumer electronics, automobiles, aircraft and robots, portable/back-up generators and domestic combined heat and power (CHP) units. For highest power density, these systems are operating at speeds between 100 000 rpm and 1 Mrpm at power levels of up to several kilowatts. A typical characteristic of all the systems is the variable speed depending on the load. In combination with a 3-phase generator this leads to a variable 3-phase output voltage, which has to be controlled to a constant dc voltage usually required for applications in this power range. However, in literature only systems with variable dc output voltage [19] and variable 3-phase ac voltages [21] have been presented. Since such a device should be able to follow unpredictable load changes, the output power can vary from no load to full load, while the output voltage must remain constant.

Besides ultra-high-speed micro turbine generator systems also other applications are employing a rectifier. In [56] a wearable power system is presented which can be carried easily on the human body and supplies an average of 20 W for 4 days (with a peak power of 200 W) and has a total system weight of less than 4 kg. Such a system is developed for power supply of infantry soldier's equipment but could also be used in civil applications.

In addition, mesoscale energy harvesting technologies like small-scale wind turbines and micro-hydro power systems for charging batteries, to supply consumer electronics or to provide electricity for lights need reliable power electronics to provide a constant output voltage [57] and [35]. All of these systems require a rectifier for supplying a constant dc voltage.

This chapter starts with the specifications for the rectifier, required for the compressed-air-to-electric-power turbine generator system. Then, different 3-phase rectifier concepts for such a turbine generator system are evaluated, and compared concerning losses, total efficiency, common mode (CM) noise, volume, and control complexity and finally the most suitable topology is selected and experimentally verified and tested with different modulation methods.

4.1 Rectifier Specifications

The power electronics must be able to convert a variable 3-phase input voltage with high frequency into a constant output dc voltage (Figure 1.5). The high fundamental phase current frequency (up to 8333 Hz), the aim to build the system as compact as possible and a high converter efficiency (in order not to compromise the overall system efficiency) are the main challenges. In [58], [59], [60], [61], [62], [63], [64], [65] and [66] several possible 1-phase and 3-phase ac-dc boost converters are summarized.

In a PM generator, the magnitude of the back emf is proportional to the speed. In order to supply a constant dc output voltage, in this case 24 Vdc, also at low speeds, boost functionality is required. The maximal power output is limited to 150 W, which leads to a dc current of 6.25 A.

In order to make the overall system volume as small as possible the rectifier should be integrated into the turbine generator system. This avoids an additional heat sink for the power and control electronics because the rectifier can be attached to the generator casing and thereby cooled by the air flow.

4.2 Topologies and Simulations

4.2.1 Active 3-Phase PWM Rectifier

An active 3-phase PWM rectifier with sinusoidal phase currents is the state of the art solution in drive systems (Figure 4.1). However, it is not naturally the best choice, because it leads to excessive switching frequencies (>500 kHz) or a large sinusoidal filter. To control the phase currents an encoder, two current measurements in the generator phases and an extremely high current control-loop bandwidth are required which presents challenges concerning current measurement, analog signal electronics, controller and gate driver design, and switching time. Finally, sinusoidal currents with a low ripple are not essentially required due to the special slotless generator topology and litz wire winding which allows a high ripple current without increased generator losses [67], and also the torque ripple is not relevant due to the inertia of the turbine. However, the active 3-phase PWM rectifier also has advantages. If a bidirectional power flow is necessary, i.e. for starting of a gas turbine, the active 3-phase PWM rectifier is an appropriate solution.

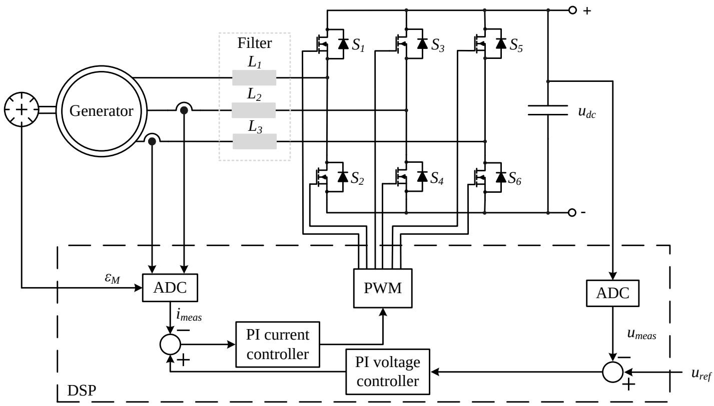

Figure 4.1: *Active 3-phase PWM rectifier with additional ac filter inductors (grey) and encoder.*

4.2.2 Active or Passive 3-Phase Rectifier with Boost Converter

The second option is a passive unidirectional 3-phase diode rectifier with additional boost converter (Figure 4.2), in order to ensure a constant output voltage. The diodes are conducting for 120° and are commutating with fundamental frequency. Considering the loss calculations in Table 4.2, the rather high rectifier diode on-state losses can be reduced by exchanging them with MOSFETs, i.e. by active rectification, but then an encoder or a 60° sector detection unit (Figure 4.10) is required.

The main disadvantages of the full bridge rectifier with additional boost converter are the large number of semiconductors, the rather large dc inductor and the higher conduction losses due to three semiconductors in the current path. If a dc-link capacitor is used, the phase currents show the well known double pulse shape, while if the dc-link capacitor is omitted one can achieve a 120° block-type waveform. When bidirectional operation is required, the diodes must be exchanged with switches (indicated in Figure 4.2). Simulation results of the system (no dc-link capacitor and with active bridge) are presented in Figure 4.3.

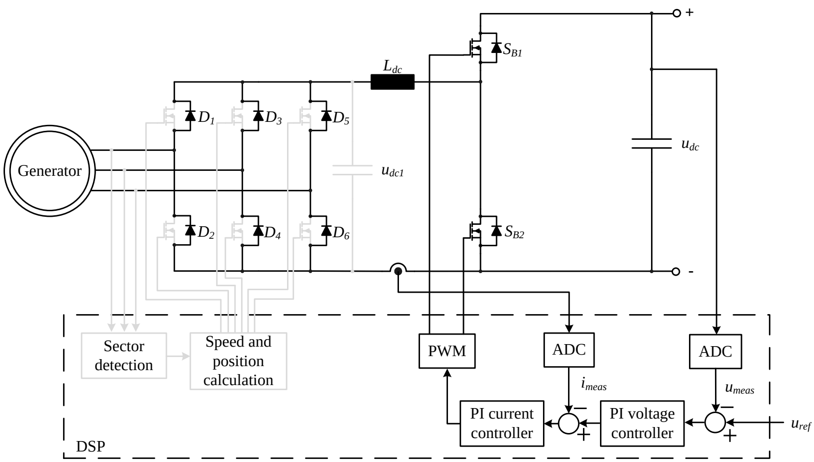

Figure 4.2: *Full bridge rectifier with additional boost converter ($L_{dc} = 10\ \mu\text{H}$). The 3-phase diode rectifier can be realized with MOSFETs (grey) and/or synchronous rectification, in order to reduce conduction losses.*

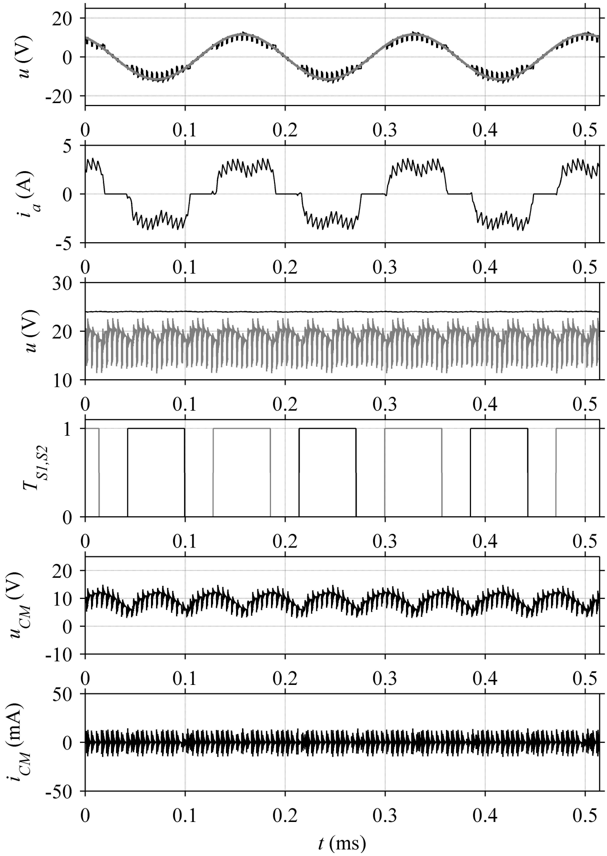

Figure 4.3: *Simulation results of the 3-phase full bridge rectifier with boost converter (L_{dc} = $10\mu H$). Generator back emf $u_{emf,a}$ (grey) and terminal voltage $u_{t,a}$ (black), phase current i_a, output voltage u_{dc} (black) and u_{dc1} (grey) and switching signals for one half bridge of the rectifier $T_{S1,S2}$ as well as CM voltage u_{CM} and current i_{CM} are shown. The switching frequency of the boost converter is f_s = 200 kHz and the fundamental frequency is f_f = 5833 Hz (350 000 rpm) while C_{Y-GND} was assumed to be 48 pF (cf. Figure 4.12).*

4.2.3 Half Controlled 3-Phase PWM Boost Rectifier

The half controlled 3-phase PWM boost rectifier (HCBR or 3-phase bridgeless boost rectifier topology) has been introduced in [58], [59], [60], [62], [63] and [64], and as single-phase system in [61], [66] and [68] respectively. It is a simple and economic circuit for applications where a maximal power factor of $\lambda = 3/\pi = 0.955$ and a total harmonic distortion of THD $\approx 30\%$ (when neglecting the current ripple and assuming block-type phase current waveform) is sufficient.

An advantage of the HCBR compared to the passive diode rectifier with series connected boost converter (Figure 4.2) is that the inductor current flows through only two semiconductors, which reduces conduction losses and therefore increases efficiency. Further advantages of the HCBR compared to an active 3-phase rectifier (Figure 4.1) are the simple structure, the shoot through free bridge leg structure, and that only one current sensor and current control loop is required. Also, only three controlled switches and gate drivers with a single power supply (common source) are needed. Compared with a diode rectifier a better performance, an actively controlled output voltage and a lower input current THD can be achieved. Considering the overall volume, the HCBR can be built much smaller than the system in Figure 4.2 because no additional dc inductor is required and the number of semiconductors can be significantly reduced. Instead of using three additional ac filter inductors the stator inductance of the generator can be used. If the inductance is too small or no high switching frequency is tolerated, only small additional ac filter inductors are required (indicated in Figure 4.4).

When replacing the high side diodes with switches, and therefore increasing control complexity, bidirectional operation and further reduction of the diode conduction losses can be achieved. Then, with a brushless-dc machine modulation method [69], a gas turbine can be started. In order to avoid a high switching frequency and large ac inductors for the HCBR the maximum ripple current is chosen to be a large value of 2 A (compared to the maximum current of 6 A), and this results in a switching frequency of approximately 200 kHz to 400 kHz.

In previous literature, there is only limited information available on the HCBR topology, especially concerning modulation, current stresses and common mode characteristics. Therefore, the topology is analyzed in detail in the following section 4.3.

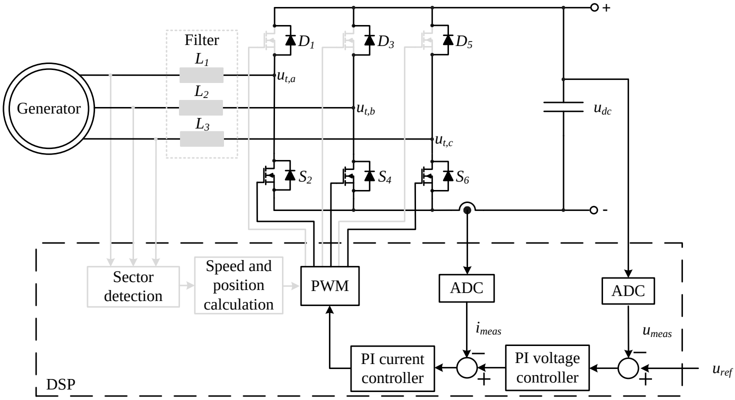

Figure 4.4: *Half controlled 3-phase PWM boost rectifier (HCBR) ($L_{1,2,3}$ = 3.3μH). For the modulation scheme with synchronous switching the sector detection must not to be implemented (grey), see section 4.2.3. The high side diodes can be exchanged with MOSFETs in order to reduce conduction losses or if bidirectional operation is required (grey).*

4.3 Review of HCBR

4.3.1 HCBR Space Vector Representation

The functionality of the HCBR can be analyzed with space vector representation of the 3-phase quantities. Assuming continuous conduction in all three phases and currents $i_{a,b,c}$ in phase with the back emf voltages $u_{emf,a,b,c}$, two different phase current patterns must be considered (Figure 4.5 and Figure 4.6).

For assuming two positive phase currents and one negative phase current, i.e. $i_a > 0$, $i_b > 0$, $i_c < 0$ (interval *II* in Figure 4.5(b)): The current in phases a and b can flow through the diode D_1/D_3 to the high side (MOSFET S_2/S_4 off, solid line in Figure 4.5(a)) or to ground (MOSFET S_2/S_4 on, dashed line in Figure 4.5(a)), while the current in phase c must flow through the MOSFET S_6 or its body diode (solid line in Figure 4.5(a)). In this case, four of eight possible space vectors are available, namely $\underline{u}_{u,(100)}$, $\underline{u}_{u,(010)}$, $\underline{u}_{u,(110)}$ and, $\underline{u}_{u,(000)}$, which implies

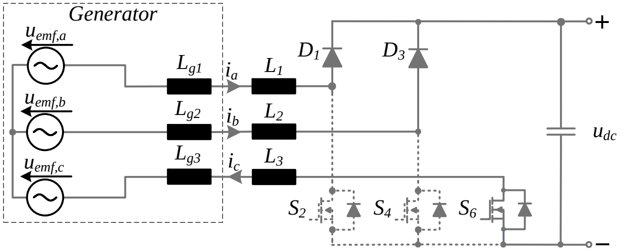

(a)

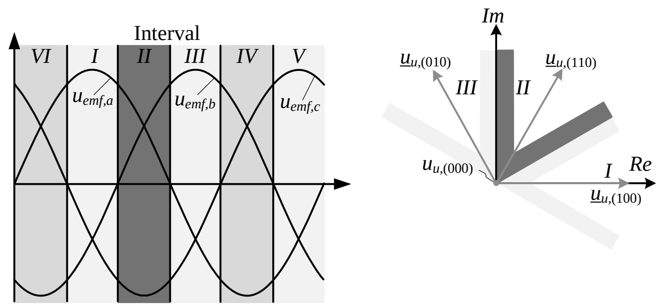

(b)

Figure 4.5: *Voltage space vector representation assuming two positive phase currents and one negative phase current, i.e. $i_a > 0$, $i_b > 0$, $i_c < 0$ (interval II).*

that sinusoidal currents can be formed in interval *II*. With the same approach it can be seen that also in interval *IV* and interval *VI* all necessary space vectors for sinusoidal current formation are available.

Assuming now two negative phase currents and one positive phase current, i.e. $i_a < 0$, $i_b > 0$, $i_c < 0$ (interval *III* in Figure 4.6(b)), the current in phase b can flow through the diode D_3 to the high side (MOSFET S_4 off, solid line in Figure 4.6(a)) or to the negative dc rail (MOSFET S_4 on, dashed line in Figure 4.6(a)), while the currents in phases a and c flow through the MOSFETs S_2/S_6 or their body diodes (solid line in Figure 4.6(a)). In this case only two space vectors are available, namely $\underline{u}_{u,(100)}$ and $\underline{u}_{u,(000)}$, which implies that no sinusoidal

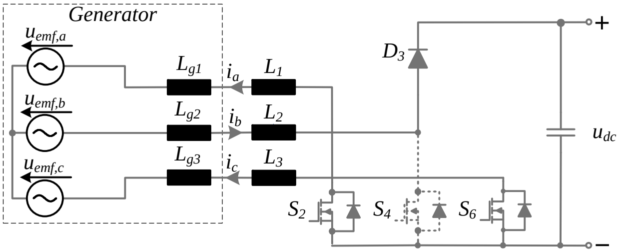

(a)

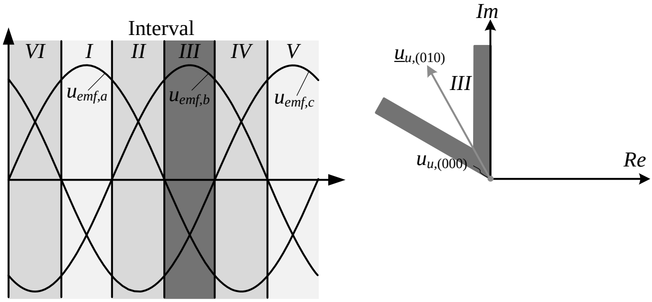

(b)

Figure 4.6: *Voltage space vector representation assuming one positive phase current and two negative phase currents, i.e.* $i_a < 0$, $i_b > 0$, $i_c < 0$ *(interval III).*

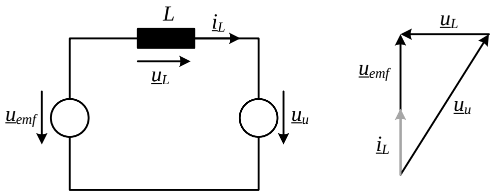

Figure 4.7: *Space vector equivalent circuit and space vector diagram of half controlled 3-phase PWM boost rectifier (HCBR).*

currents can be formed in interval *III*. It is immediately obvious that also in interval *I* and interval *V* only two space vectors are available and therefore no sinusoidal phase currents can be formed in these intervals.

Sinusoidal phase currents $i_{a,b,c}$ in phase with $u_{emf,a,b,c}$ would require an average converter voltage vector $\underline{u}_u$ lagging the induced voltage vector $\underline{u}_{emf}$ as shown in Figure 4.7. However if only one voltage vectors besides the zero voltage vector is available, like in intervals *I*, *III* and *V*, this is not possible and therefore no sinusoidal currents can be formed with a HCBR over the entire fundamental period. Furthermore, space vector $\underline{u}_{u,(111)}$ cannot be applied, because of the high side diodes and the condition $i_a + i_b + i_c = 0$.

In the following two sections two modulation methods are described, i.e. the synchronous modulation scheme and the novel sector detection modulation scheme.

4.3.2 Synchronous Modulation Scheme

When using the synchronous modulation scheme, the same PWM signal is used for setting all three switches [66], which leads to a periodic short-circuit of the generator phases during the turn on time of the switches (Figure 4.4), which causes an increase of the currents, depending on the stator inductance and the external inductors. The generator short-circuit is an admissible operating state and corresponds to the space vector $\underline{u}_{u,(000)}$ in (Figure 4.5).

The advantages compared to more complex modulation schemes are the lower hardware and computation effort, while as negative effect the phase current waveform cannot be controlled and high losses in the anti-parallel low side diodes appear. Furthermore, no speed information can be computed, because no sector detection unit is implemented (Figure 4.9).

To reduce complexity, the current measurement is done with a single sensor on the dc side instead of two current measurements in the generator phases. The current must therefore be measured during the off interval ($DT_s < t < T_s$) of the PWM period (indicated in Figure 4.12), which means in every space vector state except $\underline{u}_{u,(000)}$. The output voltage can be controlled with a voltage controller with underlying current controller. Simulation results can be seen in Figure 4.8.

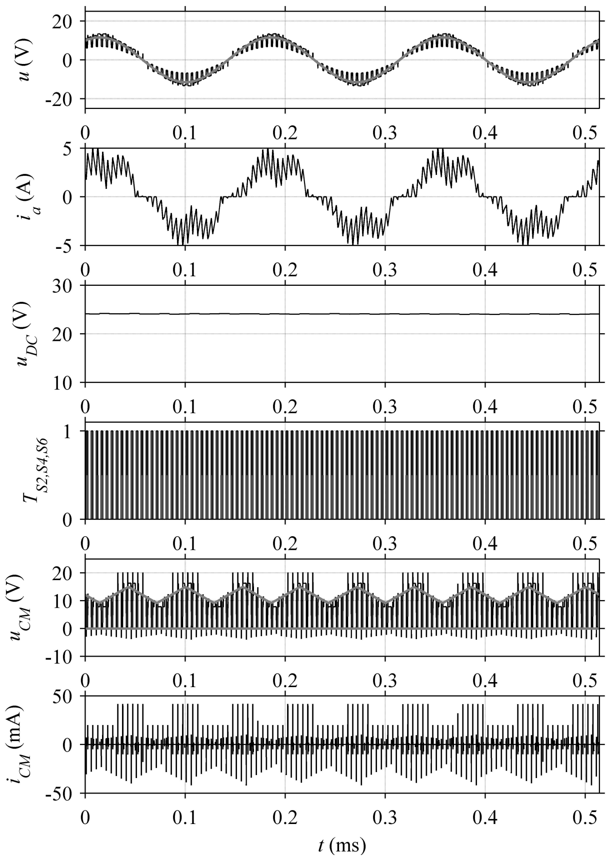

Figure 4.8: *Simulation results of the HCBR with synchronous modulation scheme ($L_{1,2,3}$ = 3.3 μH). Generator back emf $u_{emf,a}$ (grey) and terminal voltage $u_{t,a}$ (black), phase current i_a, output voltage u_{dc}, switching signals for the 3-phase legs $T_{S2,S4,S6}$ as well as CM voltage u_{CM} (including the envelope cf. 4.31 and 4.32) and current i_{CM} are shown. The switching frequency is f_s = 200 kHz and the fundamental frequency is f_f = 5833 Hz (350 000 rpm) while C_{Y-GND} was assumed to be 48 pF (cf. Figure 4.12).*

4.3.3 Sector Detection Scheme

With detecting sectors 1-6 according to Figure 4.10, a novel modulation scheme, named sector detection scheme, can be realized. The sectors can be determined without position sensor but with measuring the machine terminal voltages. In contrary to the synchronous modulation scheme the PWM signal is now only connected to the switch of the phase showing the highest terminal voltage, and therefore changing to the next phase every 120° (Figure 4.10). During this 120° interval the switch corresponding to the lowest terminal voltage is continuously turned on, while the terminal voltage which lies in between does not carry any current and therefore the corresponding switch is turned off (Figure 4.10). This modulation scheme leads to a short circuit of pulsing generator phases showing highest and lowest potential during the turn on time of the PWM switch which causes an increase of the generator currents, depending on the inductance of the stator and the external inductors. During turn-off of the according PWM switch the current is charging the capacitor over the upper diode. This leads to block shaped phase currents similar to six-step BLDC motors [69]. In Figure 4.9 simulation results are shown, the block shaped current with an amplitude variation of six times fundamental frequency due to the limited bandwidth of the current controller and a conduction angle of 120° in positive and negative direction can be seen.

The advantages of this novel modulation scheme compared to the previously reported modulation scheme in section 4.3.2 are the lower switching and conduction losses, the lower CM voltage and current and the higher power factor and lower phase current THD. As a side effect, the generator speed can be calculated with the sector detection unit, which can be used for monitoring and for controlling of the entire compressed-air-to-electric-power system.

4.3.4 Voltage Space Vector Simulation for Different Modulations

In Figure 4.11 the simulated voltage space vectors for the half controlled 3-phase PWM boost rectifier (HCBR) for synchronous modulation (Figure 4.11(a)) and sector modulation (Figure 4.11(b)) are shown. It should be pointed out that not only the six possible active space vectors are applied, but also the vectors lying on the hexagon are present. This is

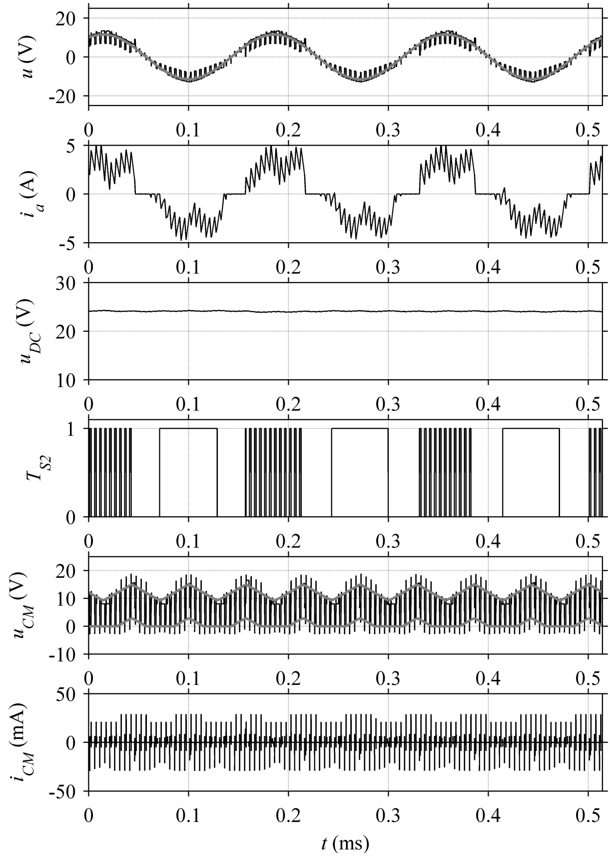

Figure 4.9: *Simulation results of the HCBR with sensorless 60° sector detection modulation scheme ($L_{1,2,3}$ = 3.3 μH). Generator back emf $u_{emf,a}$ (grey) and terminal voltage $u_{t,a}$ (black), phase current i_a, output voltage u_{dc}, switching signal for one phase leg T_{S2} as well as CM voltage u_{CM} (including the envelope cf. 4.29 and 4.30) and current i_{CM} are shown. The switching frequency is f_s = 200 kHz and the fundamental frequency is f_f = 5833 Hz (350 000 rpm) while C_{Y-GND} was assumed to be 48 pF (cf. Figure 4.12).*

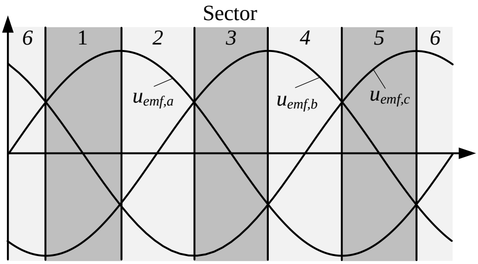

MOSFET S_2	PWM	PWM	off	on	on	off
MOSFET S_4	on	off	PWM	PWM	off	on
MOSFET S_6	off	on	on	off	PWM	PWM

Figure 4.10: *Sector definition for the HCBR and the according MOSFET operation states for the sector detection modulation scheme.*

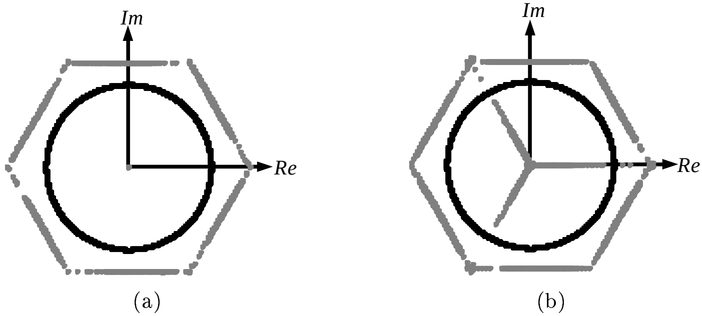

Figure 4.11: *Simulation of space vectors for the HCBR for synchronous modulation scheme (Figure 4.11(a)) and sector modulation scheme (Figure 4.20(b)). Back emf: black, terminal voltage: grey.*

due to the floating phase (off interval of the MOSFET) which is not connected to the positive nor the negative dc voltage bus. The potential of this phase changes over a 60° interval (Figure 4.10) from 0 V to u_{dc} or vice versa. This happens because the high side diode of the phase with potential in between the values of the other two phases cannot conduct within the MOSFET turn off period and therefore changes over a 60° interval until the corresponding phase shows the highest or lowest potential for the next 120°.

In the sector modulation scheme the space vector $\underline{u}_{u,(000)}$ is not applied because all three MOSFETs are not closed simultaneously. Instead of the short circuit space vector, a vector lying on the main axis in direction of $\underline{u}_{u,(100)}$, $\underline{u}_{u,(010)}$, or $\underline{u}_{u,(001)}$ is applied, the amplitude varies due to a floating phase with a potential between 0 V and u_{dc}.

4.3.5 Current Stresses

The losses in different components of the HCBR can be calculated with the according rms current for components with a resistive behavior or average current for components with a current independent forward voltage drop, respectively.

Assuming block-type currents, Table 4.1 presents the current stresses on the phase inductors, the power transistors (MOSFETs or IGBTs), the freewheeling diodes and the output capacitor of the HCBR in dependency on the modulation method, where M is the voltage transfer ratio

$$M = \frac{U_{dc}}{\widehat{U}_{emf(l-l),i}} \tag{4.1}$$

and where the duty cycle can be defined as

$$d(t) = 1 - \frac{U_{emf(l-l),i}(t)}{U_{dc}} = 1 - \frac{1}{M}\left|sin(\omega t)\right|. \tag{4.2}$$

In steady-state the output current I_{out} is the mean value of the pulse-shaped current i_{meas} (shown in Figure 4.12) and can be calculated as

$$I_{out} = \frac{3}{\pi}\int_{\pi/3}^{2\pi/3} \widehat{I}_i(1-d)d(\omega t) \tag{4.3}$$

$$= \frac{3}{\pi}\int_{\pi/3}^{2\pi/3} \widehat{I}_i \frac{1}{M}\left|sin(\omega t)\right| d(\omega t) \tag{4.4}$$

$$= \frac{3\widehat{I}_i}{M\pi} \tag{4.5}$$

where $\widehat{I}_i$ is the amplitude of the block-shaped phase inductor current i_{meas}. $\widehat{I}_i$ therefore can be expressed as

$$\widehat{I}_i = I_{out}\frac{M\pi}{3}. \tag{4.6}$$

The rms current in the phase inductors are independent on the modulation method and can be calculated as

$$I_{i,rms} = \frac{1}{\pi}\int_{\pi/6}^{5\pi/6} \widehat{I}_i^2 d(\omega t) = \widehat{I}_i\sqrt{\frac{2}{3}}. \tag{4.7}$$

The current stresses on the high-side freewheeling diodes are also independent of the modulation method and can be calculated as

$$i_{D,avg} = \widehat{I}_i(1-d(t)) \tag{4.8}$$

$$I_{D,avg} = \frac{1}{\pi}\int_{\pi/3}^{2\pi/3} \frac{\widehat{I}_i}{M} sin(\omega t)d(\omega t) = \frac{\widehat{I}_i}{M\pi} = \frac{I_{out}}{3} \tag{4.9}$$

$$I_{D,rms} = \sqrt{\frac{1}{\pi}\int_{\pi/3}^{2\pi/3} \frac{\widehat{I}_i^2}{M} sin(\omega t)d(\omega t)} = \frac{\widehat{I}_i}{\sqrt{M\pi}}. \tag{4.10}$$

The current stresses for the power transistors with synchronous modulation can be calculated as

$$i_{S,avg} = \underbrace{\widehat{I}_i d(t)}_{positive\ current} + \underbrace{\widehat{I}_i d(t)}_{negative\ current} \tag{4.11}$$

$$I_{S,avg} = \frac{2}{\pi}\int_{\pi/3}^{2\pi/3} \widehat{I}_i \left(1 - \frac{1}{M} sin(\omega t)\right) d(\omega t) \tag{4.12}$$

$$= \widehat{I}_i \left(\frac{2}{3} - \frac{2}{M\pi}\right) \tag{4.13}$$

$$I_{S,rms} = \sqrt{\frac{2}{\pi}\int_{\pi/3}^{2\pi/3} \widehat{I}_i^2 \left(1 - \frac{1}{M} sin(\omega t)\right) d(\omega t)} \tag{4.14}$$

$$= \widehat{I}_i \sqrt{\left(\frac{2}{3} - \frac{2}{M\pi}\right)}. \tag{4.15}$$

For the antiparallel diodes with synchronous modulation the current stresses can be calculated as

$$i_{DS,avg} = \underbrace{\widehat{I}_i (1 - d(t))}_{negative\ current} \tag{4.16}$$

$$I_{DS,avg} = \frac{1}{\pi}\int_{\pi/3}^{2\pi/3} \frac{\widehat{I}_i}{M} sin(\omega t) d(\omega t) = \frac{\widehat{I}_i}{M\pi} = \frac{I_{out}}{3} \tag{4.17}$$

$$I_{DS,rms} = \sqrt{\frac{1}{\pi}\int_{\pi/3}^{2\pi/3} \frac{\widehat{I}_i^2}{M} sin(\omega t) d(\omega t)} = \frac{\widehat{I}_i}{\sqrt{M\pi}}. \tag{4.18}$$

Assuming sector modulation the current stresses in the power transistors can be calculated as

$$i_{S,avg} = \underbrace{\widehat{I}_i d(t)}_{positive\ current} + \underbrace{\widehat{I}_i}_{negative\ current} \tag{4.19}$$

$$I_{S,avg} = \frac{1}{\pi}\int_{\pi/3}^{2\pi/3} \widehat{I}_i \left(2 - \frac{1}{M} sin(\omega t)\right) d(\omega t) \tag{4.20}$$

$$= \widehat{I}_i \left(\frac{2}{3} - \frac{1}{M\pi}\right) \tag{4.21}$$

$$I_{S,rms} = \sqrt{\frac{1}{\pi}\int_{\pi/3}^{2\pi/3} \widehat{I}_i^2 \left(2 - \frac{1}{M} sin(\omega t)\right) d(\omega t)} \tag{4.22}$$

$$= \widehat{I}_i \sqrt{\frac{2}{3} - \frac{1}{M\pi}}. \tag{4.23}$$

The average and rms currents for the antiparallel diodes with sector modulation are zero. $I_{DS,avg} = 0$ and $I_{DS,rms} = 0$, because the current can always flow back through a turned on power transistor.

The rms value of the output capacitor current can be calculated from the rms and average value of the high-side freewheeling diodes currents

$$I_{C,rms} = \sqrt{I_{D,rms}^2 - I_{D,avg}^2} = \widehat{I}_i \sqrt{\frac{3}{M\pi}\left(1 - \frac{3}{M\pi}\right)}. \tag{4.24}$$

4.3.6 Common-Mode Characteristics

The HCBR is also analyzed concerning the CM characteristics. The generator terminals are connected to the rectifier, which can be modeled as switching frequency voltage sources. These voltage sources charge and discharge the parasitic capacitance C_{Y-GND} between output ground (generator casing) and generator star point (Figure 4.12), which leads to a CM noise current flow that could disturb other sensitive electronic parts close-by [61] and [66].

Due to the high switching frequency directly at the terminals of the generator, the HCBR causes a large CM noise current (Figure 4.8 and Figure 4.9). The full bridge rectifier with additional boost converter causes less CM noise problems, because the high frequency switching voltage is

Phase inductors	$I_{i,avg} = 0$	$I_{i,rms} = \widehat{I}_i\sqrt{\frac{2}{3}}$
Freewheeling diodes	$I_{D,avg} = \frac{\widehat{I}_i}{M\pi} = \frac{I_{out}}{3}$	$I_{D,rms} = \frac{\widehat{I}_i}{\sqrt{M\pi}}$
Power MOSFETs [1]	$I_{S,avg} = \widehat{I}_i\left(\frac{2}{3} - \frac{2}{M\pi}\right)$	$I_{S,rms} = \widehat{I}_i\sqrt{\frac{2}{3} - \frac{2}{M\pi}}$
Antiparallel diodes [1]	$I_{DS,avg} = \frac{\widehat{I}_i}{M\pi} = \frac{I_{out}}{3}$	$I_{DS,rms} = \frac{\widehat{I}_i}{\sqrt{M\pi}}$
Power MOSFETs [2]	$I_{S,avg} = \widehat{I}_i\left(\frac{2}{3} - \frac{1}{M\pi}\right)$	$I_{S,rms} = \widehat{I}_i\sqrt{\frac{2}{3} - \frac{1}{M\pi}}$
Antiparallel diodes [2]	$I_{DS,avg} = 0$	$I_{DS,rms} = 0$
Output capacitor	$I_{C,avg} = 0$	$I_{C,rms} = \widehat{I}_i\sqrt{\frac{3}{M\pi}\left(1 - \frac{3}{M\pi}\right)}$

[1] Synchronous modulation scheme
[2] Sector modulation scheme

Table 4.1: *Current stresses depending on the modulation method of the HCBR and assuming block-shaped currents, where M is the voltage transfer ratio 4.1 and and $\widehat{I}_i$ is the amplitude of the block-shaped phase inductor currents 4.6.*

not directly applied to the terminals of the generator and therefore only small CM currents can be observed (Figure 4.3).

The relevant capacitance C_{Y-GND} (Figure 4.12) has been measured with an impedance analyzer. The total capacitance of the three short-circuited power cables of the assembled generator and the generator casing is 48 pF. With this value, the CM currents have been determined with Gecko Circuits simulations [70]. In Figure 4.15 the simulated quasi-peak CM conducted emission for sector detection modulation, a C_{Y-GND} of 48 pF and a switching frequency of $f_s = 200$ kHz is shown.

4.3.7 Envelope of the HF Common-Mode Voltage

Assuming $u_{emf,a} > u_{emf,b} > u_{emf,c}$ (sector 2 in Figure 4.10), $i_a + i_b + i_c = 0$ and all three switches in the turn-on state, the CM voltage is

$$\left| \begin{aligned} u_{CM} &= -u_{emf,a} + L\frac{di_a}{dt} \\ u_{CM} &= -u_{emf,b} + L\frac{di_b}{dt} \\ u_{CM} &= -u_{emf,c} + L\frac{di_c}{dt} \end{aligned} \right|$$

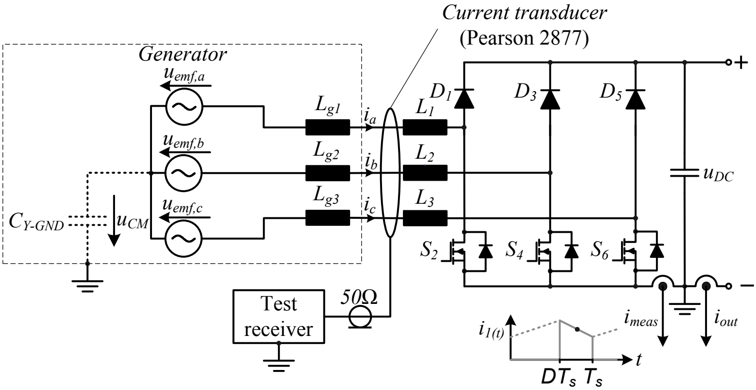

Figure 4.12: *Generator equivalent circuit including the parasitic CM capacitance C_{Y-GND} and the half-controlled 3-phase PWM boost rectifier (HCBR). A Pearson 2877 current transducer was used to determine the conducted CM noise emissions.*

$$\begin{aligned}\Rightarrow 3u_{CM} &= -\left(u_{emf,a} + u_{emf,b} + u_{emf,c}\right)\\ &\quad + L\left(\frac{di_a}{dt} + \frac{di_b}{dt} + \frac{di_c}{dt}\right)\\ \Rightarrow u_{CM} &= 0. \end{aligned} \tag{4.25}$$

If all three switches are off, the CM voltage is

$$\left| \begin{array}{l} u_{CM} = -u_{emf,a} + L\frac{di_a}{dt} + u_{dc} \\ u_{CM} = -u_{emf,b} + L\frac{di_b}{dt} \\ u_{CM} = -u_{emf,c} + L\frac{di_c}{dt} \end{array} \right|$$

$$\begin{aligned}\Rightarrow 3u_{CM} &= -\left(u_{emf,a} + u_{emf,b} + u_{emf,c}\right)\\ &\quad + L\left(\frac{di_a}{dt} + \frac{di_b}{dt} + \frac{di_c}{dt}\right) + u_{dc}\\ \Rightarrow u_{CM} &= \frac{u_{dc}}{3}. \end{aligned} \tag{4.26}$$

Still assuming $u_{emf,a} > u_{emf,b} > u_{emf,c}$ (sector 2 in Figure 4.10), but only two conducting phases, i.e. $i_a + i_c = 0$ and all three switches in the turn-off state, the CM voltage is

$$\begin{vmatrix} u_{CM} = -u_{emf,a} + L\frac{di_a}{dt} + u_{dc} \\ u_{CM} = -u_{emf,c} + L\frac{di_c}{dt} \end{vmatrix}$$

$$\begin{aligned} \Rightarrow 2u_{CM} =& u_{emf,b} + L\left(\frac{di_a}{dt} + \frac{di_c}{dt}\right) + u_{dc} \\ \Rightarrow u_{CM} =& \frac{1}{2}\left(u_{emf,b} + u_{dc}\right). \end{aligned} \tag{4.27}$$

If all three switches are on but only two switches are conducting the CM voltage is

$$\begin{vmatrix} u_{CM} = -u_{emf,a} + L\frac{di_a}{dt} \\ u_{CM} = -u_{emf,c} + L\frac{di_c}{dt} \end{vmatrix}$$

$$\begin{aligned} \Rightarrow 2u_{CM} =& u_{emf,b} + L\left(\frac{di_a}{dt} + \frac{di_c}{dt}\right) \\ \Rightarrow u_{CM} =& \frac{1}{2}u_{emf,b}. \end{aligned} \tag{4.28}$$

Resulting from 4.25-4.28 the CM voltage envelope for sector detection modulation is

$$u_{CM} = max\left(\frac{1}{2}u_{emf,i}, 0\right) \qquad \text{PWM switch = on} \tag{4.29}$$

$$u_{CM} = \frac{1}{2}\left(u_{emf,i} + u_{dc}\right) \qquad \text{all switches off} \tag{4.30}$$

illustrated with two grey curves in Figure 4.9. For synchronous switching the envelope is

$$u_{CM} = 0 \qquad \text{all switches on} \tag{4.31}$$

$$u_{CM} = \frac{1}{2}\left(u_{emf,i} + u_{dc}\right) \qquad \text{all switches off} \tag{4.32}$$

illustrated with two grey curves in Figure 4.8. $u_{emf,i}$ is the back emf of the phase which is not conducting, changing every 60°.

4.4 Comparision and Topology Selection

The different rectifier topologies are compared concerning efficiency, volume, control complexity and CM characteristics. The results are compiled in Table 4.2. For a fair comparison, a total inductor volume of 800 mm^3 is defined for the topologies requiring additional inductors on the dc or ac side. Special attention has been given to the switching losses in the semiconductors, as they have a main influence on the total losses. The switching losses of the semiconductors (MOSFET: IRF6644 and of Diode: IR 12CWQ03FNPbF) have been measured with a test bench setup. The resulting loss coefficients were then used in Gecko Circuits [70] to simulate the total losses of the circuit (i.e. switching and conduction losses of the MOSFETs, diode losses, inductor losses and current measurement shunt losses) at the rated operation point of the system for a speed of 350 000 rpm and an electric power output of 25 W, 50 W, 75 W and 100 W. The constant DSP losses (1.1 W) and gate driver losses (0.4 W) have been added as no-load losses to the simulation results. The passive 3-phase rectifier has clearly the lowest efficiency due to the high diode losses, while the active rectifier reaches as high efficiencies as the HCBR. On the other hand, replacing the high side diodes of the HCBR with switches does not significantly lower the overall losses.

Based on the comparison in Table 4.2, the HCBR is selected for further evaluation. The main advantages of this topology are the low number of switches and diodes and the high efficiency, and compared to the active 3-phase PWM rectifier the low control complexity. Also for the compressed-air-to-electric-power system no bidirectional operation is required. The advantage of the synchronous modulation scheme compared to the sector detection scheme is the lower hardware and computation effort, while as negative effect higher losses in the antiparallel low side diodes appear which lowers the efficiency significantly. Using higher switching frequency instead of additional ac-inductors gives higher efficiencies at high output power levels and reduces the volume.

	3-phase rectifier with boost converter[1]		HCBR				Active 3-phase PWM rectifier	
			Three ac inductors[2]		No inductors[3]		Three ac inductors[2]	No inductor[3]
	Passive	Active	Sector	Synchronous	Sector	Synchronous	Sector	Sector
Number of switches	2	8	3	3	3	3	6	6
Number of diodes	6	0	3	3	3	3	0	0
Volume	-	-	0	0	+	+	0	+
Sector detection	no	yes	yes	no	yes	no	yes	yes
Control complexity	+	0	0	+	0	+	-	-
Bidirectional	no	(yes)	no	no	no	no	yes	yes
Common-mode (CM)	+	+	-	-	-	-	-	-
MOSFET losses	2.8 W	4.0 W	2.4 W	4.5 W	3.5 W	5.8 W	3.9 W	5.4 W
Diodes losses	6.0 W	0 W	2 W	1.9 W	2.0 W	2.0 W	0 W	0 W
Inductor losses	1.5 W	1.4 W	4.7 W	4.8 W	0 W	0 W	4.5 W	0 W
Current measurement shunt	0.6 W	0.6 W	0.4 W	0.4 W	0.4 W	0.4 W	0.4 W	0.4 W
No-load losses	1.5 W	1.5 W	1.5 W	1.5 W	1.5 W	1.5 W	1.5 W	1.5 W
Total losses	12.4 W	7.5 W	11 W	13.1 W	7.4 W	9.7 W	10.3 W	7.3 W
Efficiency	89.0%	93.0%	90.1%	88.4%	93.1%	91.2%	90.7%	93.2%

[1] $L_{dc} = 10\ \mu$H, $f_s = 200$ kHz
[2] $L_{1,2,3} = 3.3\ \mu$H, $f_s = 200$ kHz
[3] $f_s = 400$ kHz

Table 4.2: *Comparison of converter topologies for $n = 350\ 000$ rpm, $P_{out} = 100$ W and $T = 25\,^{\circ}C$. The no-load losses represent the DSP and gate driver losses.*

4.5 Measurements

The hardware realization of the ultra-compact (⌀22 mm × 60 mm) air-to-power demonstrator [71] and the HCBR power electronics (90 × 30 × 9 mm^3) are shown in Figure 6.2 and Figure 4.17, respectively. The hardware was realized such that low frequency operation with ac inductors and high frequency operation without ac inductors is possible.

4.5.1 CM Measurements

In order to verify the proposed CM propagation model and the simulation shown in Figure 4.15, CM measurements have been carried out, employing a HF current transducer Pearson 2877 with a nominal bandwidth of 200 MHz. The current transducer produces an output signal of 1 V/A at an external 50 Ω termination, which lies in parallel to the internal 50 Ω termination of the sensor. As shown in Figure 4.13, the measured voltage can be expressed as

$$u_{meas} = u_{Pearson} = 1\frac{V}{A} i_{CM}, \tag{4.33}$$

which corresponds to an attenuation $G_{Pearson}$ of

$$G_{Pearson} = 20 \cdot log(1) = 0 \text{ dB}. \tag{4.34}$$

In order to compare the CM measurements carried out with the Pearson 2877 with the standard CISPR 11 [72], the measurements must be shifted by a factor. The simplified LISN high-frequency CM equivalent circuit is shown in Figure 4.14, the measured voltage can be expressed as

$$u_{meas} = \frac{50}{3} \cdot i_{CM}, \tag{4.35}$$

which corresponds to an attenuation G_{LISN} of

$$G_{LISN} = 20 \cdot log(50/3) = 24.4 \text{ dB}. \tag{4.36}$$

Therefore, the gain of the measurement result with the Pearson 2877 current transducer G_{total} is given by

$$G_{total} = G_{LISN} - G_{Pearson} = 24.4 \text{ dB}. \tag{4.37}$$

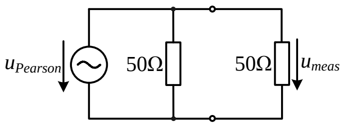

Figure 4.13: *HF current transducer Pearson 2877 (output signal of 1 V/A) with 50 Ω output resistance and an external 50 Ω-termination.*

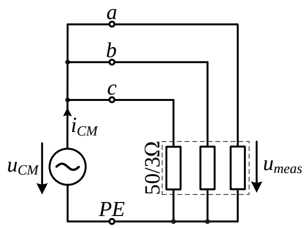

Figure 4.14: *Simplified LISN high-frequency CM equivalent circuit. The rectifier is replaced by the CM equivalent u_{cm} and the LISN plus test receiver are modeled as* 50 Ω *resistors.*

Accordingly, the measurement curves are located 24.4 dB below the measurement level detected by an EMC test receiver. Therefore all conducted emission measurements have this correction factor considered for an equitable comparison with the performance requirements.

The standard CISPR 11 [72] was chosen for establishing the performance requirements, where the frequency range of 0.15 MHz to 30 MHz is considered for class A equipment. The limits for this performance test are represented through a grey curve in Figure 4.15 and Figure 4.16.

In Figure 4.16 a quasi-peak CM conducted emission measurement when using sector detection modulation and a switching frequency of $f_s =$ 200 kHz, measured with a spectrum analyzer with an input impedance of 50Ω, is presented. Considering the rough model of the CM behavior the simulation (Figure 4.15) and the measurement (Figure 4.16) are in good agreement. The first peak at 200 kHz is related to the rectifier switching frequency. Only one measurement is shown, but also simulations and measurements with synchronous switching and with switching frequency of $f_s = 400$ kHz are in good agreement.

4.5.2 Waveforms and Efficiency Measurements

In Figure 4.20(a) and Figure 4.20(b) measurements of the active 3-phase rectifier with boost converter (no dc-link capacitor) are presented, while

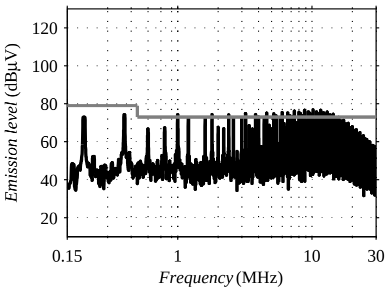

Figure 4.15: *Simulated quasi-peak CM conducted emission when using the sector detection modulation scheme and a switching frequency of* $f_s = 200$ kHz.

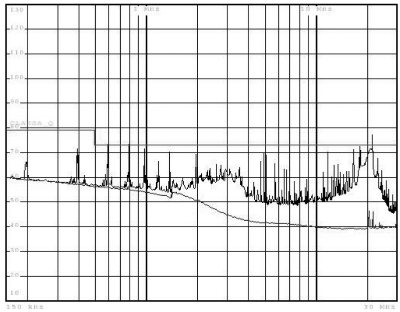

Figure 4.16: *Measured quasi-peak CM conducted emission when using the sector detection modulation scheme and a switching frequency of* $f_s = 200$ kHz. *The lowest grey signal represents the quasi-peak noise floor.*

in Figure 4.18(a) / Figure 4.18(c) and in Figure 4.19(a) / Figure 4.19(c) measurements with a HCBR at 350 000 rpm and a switching frequency of 200 kHz and 400 kHz are shown. With the sector detection modulation scheme (Figure 4.19(a)) the 120° block-type waveform for positive phase current and the rather high current ripple of approximately 2 A can be seen, while the waveform for the modulation scheme with synchronous modulation (Figure 4.18(a)) slightly differs from a 120° block type for positive phase current. All measurements show good agreement with the simulation results in Figure 4.3, Figure 4.8 and Figure 4.9 respectively. In Figure 4.20(b), Figure 4.18(b) / Figure 4.18(d) and Figure 4.19(b) / Figure 4.19(d) a step change of the dc side load and the resulting dc voltage and phase current waveform are shown.

In Figure 4.21 simulated and measured efficiencies of the HCBR with sector detection modulation scheme and with synchronous modulation scheme for different output power levels and different switching frequencies; the measured and simulated data show good agreement. Using higher switching frequency instead of additional ac inductors increases the efficiency by up to 3% at high output power levels and reduces the total inverter volume. Compared the the standard modulation scheme, the novel sector detection modulation schemes results in an efficiency increase of about 2% over the entire operating area.

4.6 Conclusion

The two most common rectifiers, the active 3-phase PWM rectifier with sinusoidal phase currents (cf. section 4.2.1) and the active or passive 3-phase rectifier with an additional boost converter (cf. section 4.2.2) for constant dc voltage supply, are not naturally the best choices for low power, variable-speed PM generators, especially for high rotational speeds. A rectifier topology comparison considering losses, CM noise, control complexity and volume identifies the HCBR (cf. section 4.2.3) as the best option. Using higher switching frequency instead of ac inductors leads to higher efficiency at minimum volume. Therefore, the HCBR with no additional ac inductors is found to be the best choice to convert a variable 3-phase input voltage with high frequency into a constant output dc voltage. Furthermore, a novel modulation scheme lowering the switching and conduction losses and therefore increasing the efficiency is presented in this thesis. Integration into a compressed-air-to-electric-power turbine generator system verifies the theoretical considerations. A drawback of the HCBR is the large CM noise current, mainly because of the high switching frequency directly at the terminals of the generator. On the other side causes the full bridge rectifier with additional boost converter less CM noise problems, because the high frequency switching voltage is not directly applied to the terminals of the generator and therefore only small CM currents can be observed. During operation the HCBR has turned out to be a simple and robust 3-phase ac-dc boost converter that has no negative influence on the operation of the turbine or the generator, e.g. no speed variation could be observed.

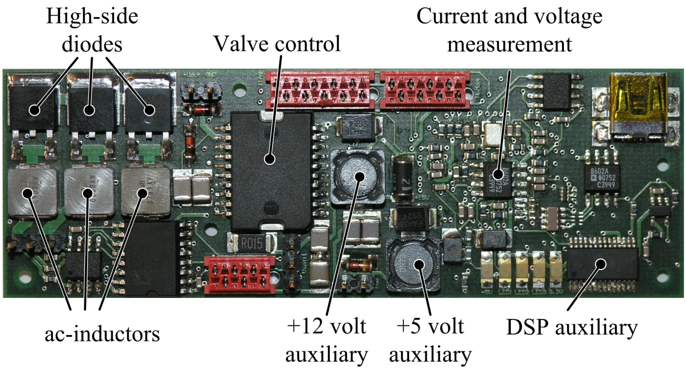

(a) Front side

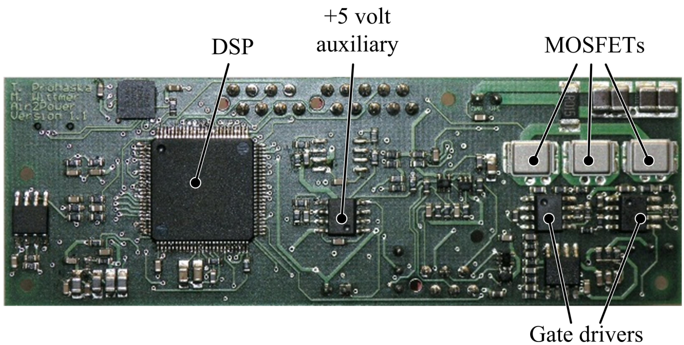

(b) Back side

Figure 4.17: *Half controlled 3-phase PWM boost rectifier electronics, including the valve control electronics (90 × 30 × 9* mm^3*).*

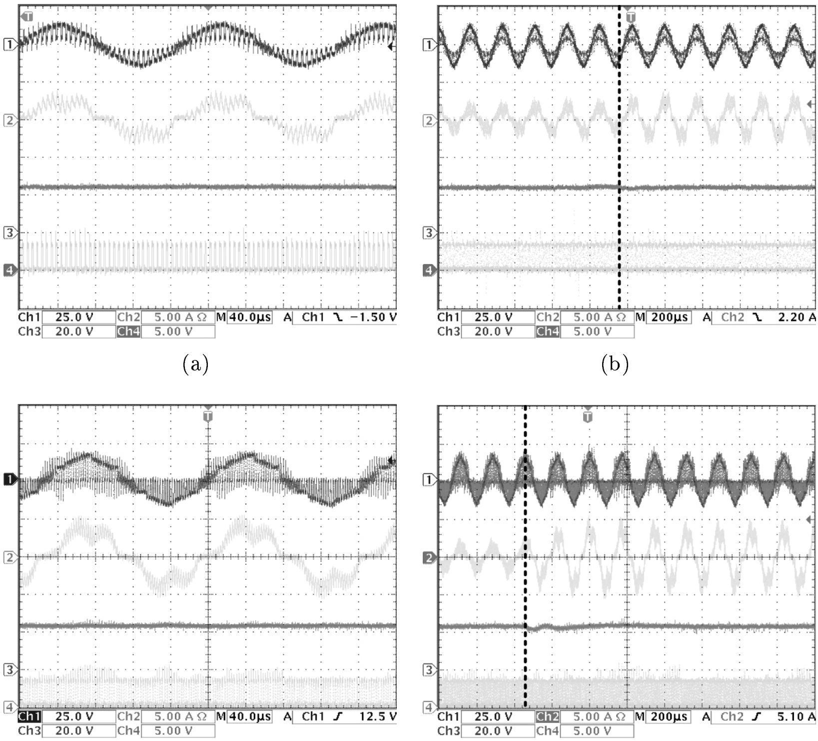

(a) (b) (c) (d)

Figure 4.18: *Measurement results of the HCBR with synchronous modulation scheme at 350 000 rpm, a switching frequency of $f_s = 200$ kHz (4.18(a)/4.18(b)) and of $f_s = 400$ kHz (4.18(c)/4.18(d)) and an output power of 40 W (4.18(a)) and 50 W (4.18(c)) and an output power step change (dashed vertical line) from 15 W to 40 W (4.18(b)) and from 15 W to 50 W (4.18(d)). Channel 1: terminal voltage, channel 2: phase current, channel 3: output voltage, channel 4: PWM signal for all three switches.*

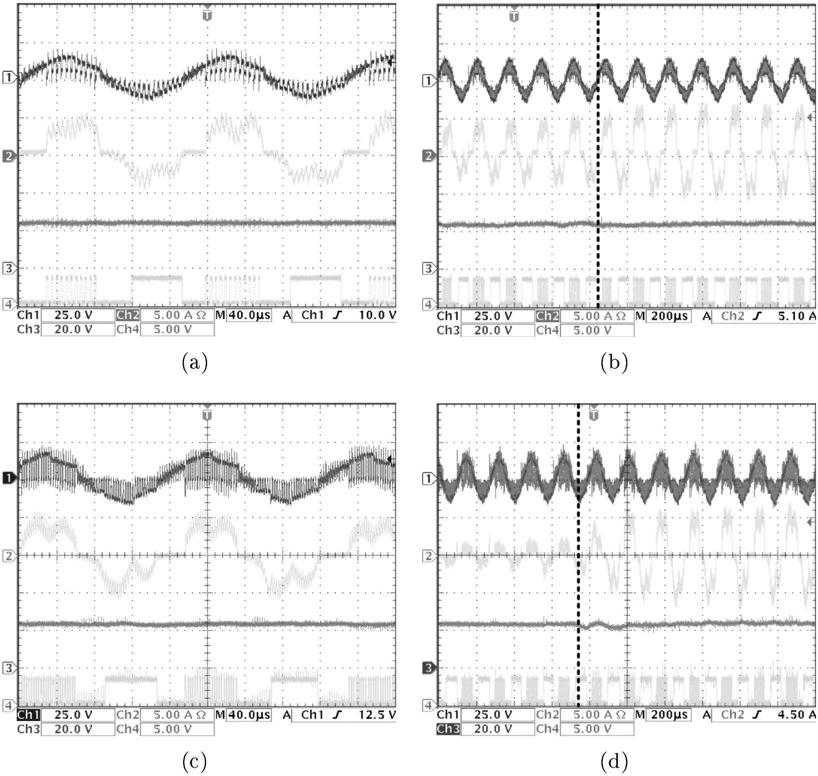

Figure 4.19: *Measurement results of the HCBR with sector detection modulation scheme at 350 000 rpm, a switching frequency of $f_s = 200\ kHz$ (4.19(a)/4.19(b)) and of $f_s = 400\ kHz$ (4.19(c)/4.19(d)) and an output power of 50 W (4.19(a)/(4.19(c)) and an output power step change (dashed vertical line) from 30 W to 60 W (4.19(b)) and from 15 W to 75 W (4.19(d)). Channel 1: terminal voltage, channel 2: phase current, channel 3: output voltage, channel 4: PWM signal for one switch.*

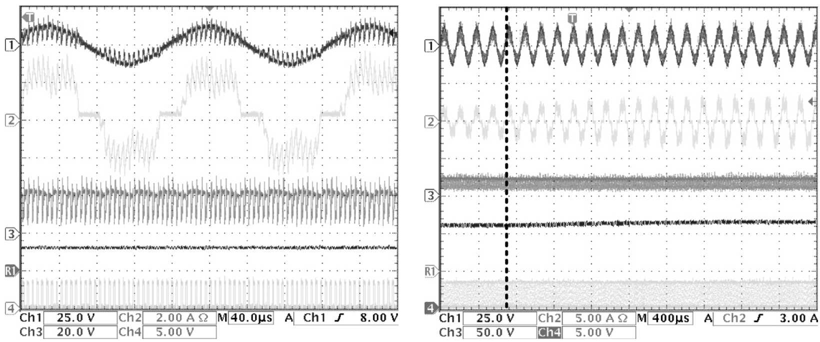

(a) (b)

Figure 4.20: *Measurement results of the active 3-phase rectifier with series connected dc-dc boost converter (no dc-link capacitor) at 350 000 rpm, a switching frequency of f_s = 200 kHz and an output power of 33 W (4.20(a)) and an output power step change from 17 W to 33 W (4.20(b)). Channel 1: terminal voltage, channel 2: phase current, channel 3: DC-link voltage, channel R1: output voltage, channel 4: boost converter PWM signal.*

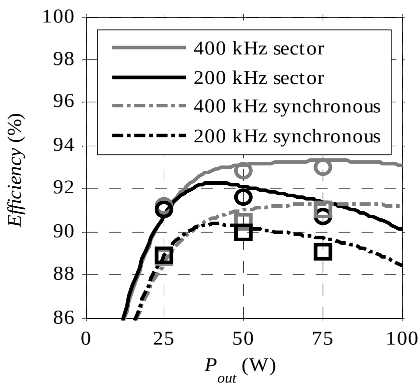

Figure 4.21: *Comparison of simulated (lines) and measured efficiencies (circles/squares) with the HCBR with sensorless 60°sector detection modulation scheme (circles) and with synchronous modulation scheme (squares) at different output power levels and different switching frequencies.*

Chapter 5

Modeling of the Compressed-Air-to-Electric-Power System

This chapter starts with the description and experimental results of the self-made throttling valve, followed by the simulation of the entire compressed-air-to-electric-power system. Also the individual system components are explained and the mathematical model is derived in detail.

5.1 Valve Construction

The need for a valve is especially important for an application like on industrial robots, cf. section 1.2.5, where unpredicted load changes can occur whereby the turbine should remain operating at highest possible efficiency. As shown in Figure 5.1, the valve determines the massflow through the turbine and can be calculated employing (2.26) using the flow function defined in (2.27). Therefore, to determine the massflow

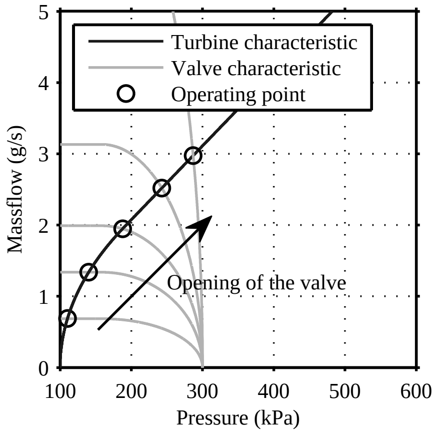

Figure 5.1: *Visualization of the operating point (circle) using an input pressure of 300 kPa and almost fully open valve, e.g. almost choked conditions.*

through the valve, the flow area A of the valve can be calculated as

$$A = d\pi \frac{\alpha}{360} p \tag{5.1}$$

where d is the valve diameter, α is the opening angle of the valve and p is the thread pitch. The used valve consist of a small Faulhaber BLDC-μ-motor (smoovy: 0515G006B) combined with a linear planetary drive with a gear transmission ratio of 125:1 (06A-125:1-S2). With this planetary drive an economical, and in small steps adjustable valve has been built.

In Figure 5.2 a cut-away view of the assembled valve can be seen, while in Figure 5.3 a picture of the different valve parts is shown and in Figure 5.4 a cut-away view of the fully assembled compressed-air-to-electric-power system is shown. The linear planetary drives a pivot on a fine pitch thread up and down, thereby increasing or decreasing the minimal valve area and consequently influencing the massflow through the entire compressed-air-to-electric-power system.

In Figure 5.5 simulation and experimental results of the massflow during opening and closing of the valve in 15° steps is presented. The input pressure remains constant at 300 kPa, while the output pressure

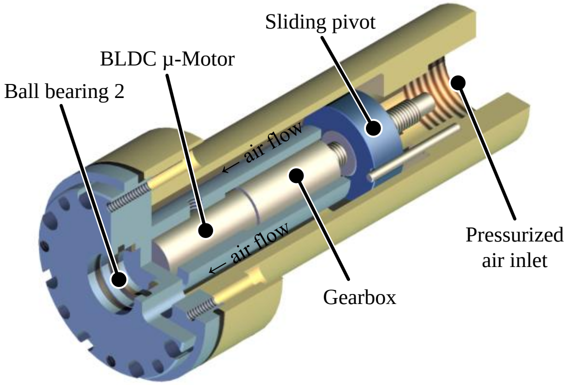

Figure 5.2: *3D-solid model of the assembled valve using the Faulhaber BLDC-μ-motor and the linear planetary drive with a gear transmission ratio of 125:1.*

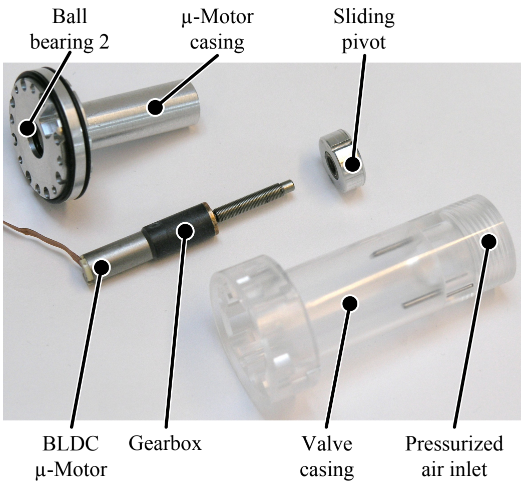

Figure 5.3: *Picture showing different valve parts for the compressed-air-to-electric-power demonstrator (∅ 22 mm × 11 mm and ∅ 15 mm × 37 mm).*

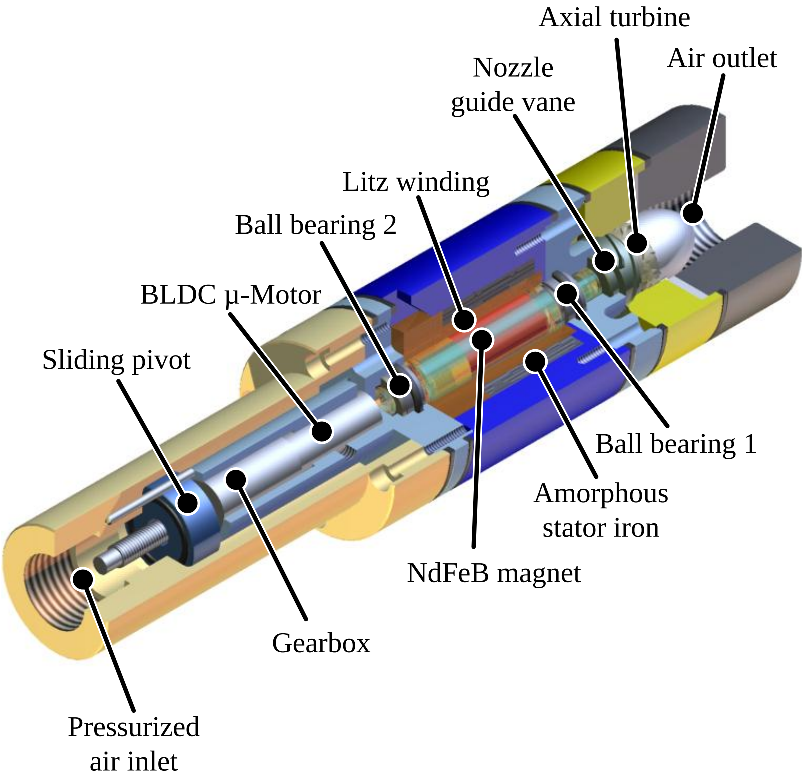

Figure 5.4: *3D-solid model of the compressed-air-to-electric-power system with assembled Faulhaber valve.*

and the massflow increases. When opening the valve, one can observe a delay during the first quarter of a turn followed by a linear increase and a flattening (choking) when reaching the maximum massflow. The delay during the first quarter can be explained with the use of O-rings in order to seal the valve, while the linear increase and the flattening comes from the flow function (2.27). With this construction an appropriate control of the overall system can be achieved. In Figure 5.1 the operating point (circle) when using an input pressure of 300 kPa and an almost fully open valve, e.g. almost choked conditions is visualized. The operating point is defined by the intersection of the turbine characteristics (dark grey curve) and the valve characteristics (light grey curve), while the valve characteristic depends on the opening angle of the valve.

5.2 System Simulation and Control

5.2.1 Valve

As described in section 5.1, the valve determines the massflow through the entire compressed-air-to-electric-power system. To determine the massflow through the valve, the cross section area, which is a function of the piston position, must be calculated. The intersection point of the valve and turbine characteristics gives the operating point and therefore the turbine inlet pressure p_0 and the massflow. The valve and turbine characteristics can be calculated with the flow function described in (2.26) and (2.27).

The valve position is determined by a PI valve position controller which has as input the actual speed, from the sensorless sector detection unit from section 4.3.3 and a reference speed defined from the actual output power utilising a LUT. The black curve in Figure 5.6 represents the stability bound and the maximum electrical power generated by the turbine and generator system as a function of speed and supply pressure. The grey curve represents the reference speed (depending on the output power) for the LUT used for the valve controller. The grey crosses in Figure 5.6 represent the supporting points for the implemented LUT for the valve controller. It can be seen that for low output power the reference speed is rather far away from the optimal efficiency point. This has to be done because of high unpredicted load changes that might

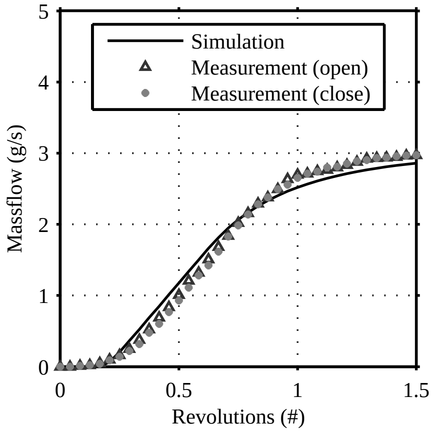

Figure 5.5: *Simulation and experimental results of the massflow during opening and closing of the valve in 15° steps, with a input pressure of 300 kPa.*

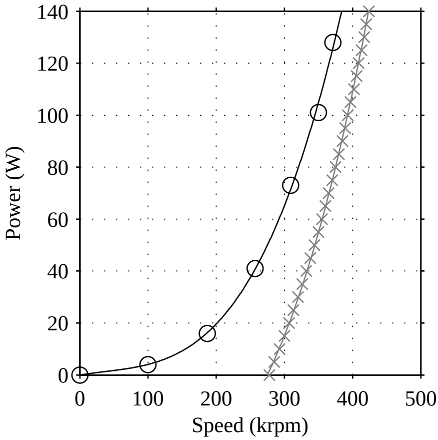

Figure 5.6: *The grey curve represents the reference speed (depending on the output power) for the LUT used for the valve controller, shown in Figure 5.9. The black curve represents the stability bound and the maximum electrical power generated by the turbine-generator-system as a function of speed and supply pressure.*

occur. The major part of the energy in the system is stored as rotational energy in the rotor, e.g. for 300 000 rpm and an inertia of $23 \cdot 10^{-9}$ kg m^2 including the turbine (Table 3.1), the rotational energy is

$$W_{rot} = \frac{J\omega^2}{2} = 11.4 \text{ J}. \tag{5.2}$$

In comparison the energy stored in the capacitors (17.3 mJ) and inductors (21.6 μJ) for an output power of 50 W is negligible. When an output power change occurs, the rotor starts to decelerate, before the valve controller can open and deliver more massflow and higher input pressure and finally start to reaccelerate the rotor. So, for low output power and in order to guaranty a stable operation during output load changes, the operating point must be chosen far enough away from the stability bound shown in Figure 5.6.

The PI valve controller is executed with an interrupt frequency of $f_{Valve} = 30$ Hz, accordingly in the worst case the output power change has to be covered for 33.3 ms by the rotational energy stored in the rotor. Assuming an output power change of $\Delta P = 50$ W and a rotational speed of 300 000 rpm the worst case rotational speed decrease can be computed with

$$\Delta W_{rot} = \frac{J(\omega_0^2 - \omega_1^2)}{2} = \frac{\Delta P_{out}}{f_{Valve}} \tag{5.3}$$

ending at a rotational speed of

$$\omega_1 = \sqrt{\omega_0^2 - \frac{2\Delta P_{out}}{f_{Valve} J}} = 277\ 000 \text{ rpm}. \tag{5.4}$$

Since the valve has a maximum opening or closing speed of 120 rpm (2 rotations per second), the rotational speed will decrease even further.

5.2.2 Turbine

The maximal mechanical turbine power $P_{m,max}$ without considering the isentropic turbine efficiency can be computed with

$$P_{m,max} = \dot{m}\Delta h_t = \dot{m} c_p \Delta T_{(0-2s)} \tag{5.5}$$

where the massflow $\dot{m}$ and the turbine inlet pressure p_0 come from the intersection point of the valve and turbine characteristics (section 5.2.1). $\Delta T_{(0-2s)}$ represents the ideal temperature drop over the turbine and can be calculated with (2.31) and c_p is the specific heat capacity.

The mechanical turbine power P_m can be calculated with

$$P_m = P_{m,max}\eta_T \tag{5.6}$$

where $P_{m,max}$ is the maximal mechanical turbine power and η_T is the turbine efficiency, which is shown in the measurement in Figure 6.7. η_T depends on the rotational speed n and turbine supply pressure.

5.2.3 Generator and Mechanical System

The mechanical performance of the turbine is reduced by the losses of the generator, therefore the electric generator output power P_{el} can be calculated as

$$P_{el} = P_m - (P_{d,dec} + P_{Cu}) \tag{5.7}$$

where $P_{d,dec}$ are the deceleration power losses (described in 6.2) and P_{Cu} are the copper losses. $P_{d,dec} + P_{Cu}$ are thus the generator losses. The generator efficiency can be computed as

$$\eta_{gen} = \frac{P_{el} + P_{rot}}{P_m + P_{rot}} = \frac{P_m + P_{rot} - (P_{d,dec} + P_{Cu,I})}{P_m + P_{rot}} \tag{5.8}$$

where P_{rot} is rotational power

$$\begin{aligned} P_{rot} &= -T_J\omega && (5.9)\\ &= -J\dot{\omega}\omega && (5.10)\\ &= -\frac{1}{2}J\frac{d}{dt}\omega^2. && (5.11) \end{aligned}$$

The negative sign can be explained when looking at transitions, e.g. $\dot{\omega} \neq 0$ and $P_{rot} \neq 0$: During intervals with decreasing turbine speed, the derivative $\dot{\omega}$ is negative, which implies that rotational energy from the rotor is flowing to the generator and therefore P_{rot} is positive. During acceleration, e.g. if the turbine speeds up, the derivative $\dot{\omega}$ is positive and therefore rotational energy is stored in the rotor and P_{rot} must be negative.

As shown in section 3.1 the main machine losses are the current dependent resistive losses (including the skin effect losses), the proximity effect losses, the iron losses, the air friction losses and the ball bearing losses. The proximity effect losses, the iron losses, the air friction losses and the ball bearing losses were measured with a deceleration test ($P_{d,dec}$) as shown in Figure 6.3 and explained in detail in section 6.2. Not included in the deceleration test are the copper losses depending on the phase currents, which can easily be added to determine the total losses and are calculated with

$$P_{Cu,I} = 3I_{rms}^2 R_S \tag{5.12}$$

where I_{rms} is rms phase current and R_S is the resistance of a generator winding.

Assuming an electrical output load step from 10 W to 40 W, ΔP in Figure 5.9 is negative, which would lead to a collapse of the speed if the valve controller would not open the valve within a certain time. In the opposite case, the turbine speed would increase until it has reached a stable operating point again, but at lower turbine and generator efficiencies. It is therefore necessary to close the valve in order to have the turbine efficiency and therefore the system efficiency as high as possible. In order to determine ω and the speed n, the dynamics of the mechanical system must be considered. The angular velocity ω is computed as

$$\omega = \int \frac{\Delta T}{J} dt = \int \frac{\Delta P}{\omega J} dt \tag{5.13}$$

with

$$\Delta P = P_{el} - P_{out}. \tag{5.14}$$

5.2.4 Power Electronics

The power electronics has been modeled using the dc/dc state-space averaging method, described in [73]. There are two state variables that must be calculated for the modeling of the HCBR, namely the current i_L through the generator and the HCBR inductors $L = 2(L_{gen} + L_{HCBR})$ (two phases are always energized) and the voltage u_C over the output capacitor.

In order to calculate the two state variables the equivalent circuit must be divided into two parts, e.g. one for closed (Figure 5.7(a)) and one for open switches (Figure 5.7(b)). The voltage across the inductor and the current into the output capacitor during the period dT_s can be described as

$$\frac{di_L}{dt} = \frac{u_L}{L} = \frac{u_1 - R_L i_L}{L} \tag{5.15}$$

$$\frac{du_C}{dt} = \frac{i_C}{C} = -\frac{u_2}{R_{Load}C} \tag{5.16}$$

and during the rest of the period $(1-d)T_s = d'T_s$

$$\frac{di_L}{dt} = \frac{u_L}{L} = \frac{u_1 - R_L i_L - U_{Diode} - u_2}{L} \tag{5.17}$$

$$\frac{du_C}{dt} = \frac{i_C}{C} = \frac{i_L}{C} - \frac{u_2}{R_{Load}C} \tag{5.18}$$

where u_2 represents the output voltage, u_L the inductor voltage, i_C the output capacitor current, R_{Load} the output load resistance, R_L the resistance of the conducting inductances $2(L_{gen} + L_{HCBR})$ and u_1 the mean input voltage (i.e. the mean back emf voltage Figure 5.9),

$$u_1 = \frac{3}{\pi}\int_{\pi/3}^{2\pi/3} \sqrt{3}\hat{u}_{ind} sin(\omega t) d(\omega t) = \frac{3\sqrt{3}}{\pi}\hat{u}_{ind}. \tag{5.19}$$

The averaged voltage and current form for a switching period T_s then follows as

$$\begin{aligned}\frac{di_L}{dt} =& d\left(\frac{u_1 - R_L i_L}{L}\right) \\ &+ d'\left(\frac{u_1 - R_L i_L - U_{Diode} - u_2}{L}\right) \\ =& \frac{u_1 - R_L i_L}{L} - d'\left(\frac{u_2 + U_{Diode}}{L}\right)\end{aligned} \tag{5.20}$$

$$\begin{aligned}\frac{du_C}{dt} =& -d\frac{u_2}{R_{Load}C} + d'\left(\frac{i_L}{C} - \frac{u_2}{R_{Load}C}\right) \\ =& d'\frac{i_L}{C} - \frac{u_2}{R_{Load}C}\end{aligned} \tag{5.21}$$

where d represents the duty cycle and T_s the clock period of the switching frequency.

Integration of (5.20) and (5.21) finally leads to the state variables

$$i_L = i_1 = \int \frac{u_1 - R_L i_1 - d' \left(u_2 + U_{Diode}\right)}{L} dt \tag{5.22}$$

$$u_C = u_2 = \int \frac{d' i_1 - i_{out}}{C} dt. \tag{5.23}$$

From (5.22) and (5.23) the block diagram for the HCBR is formed, see Figure 5.8.

The disturbances of the boost converter are the input voltage u_1 and the output current i_{out}, the duty cycle d is the control input. The output current is calculated as

$$i_{out} = \frac{u_2}{R_{Load}}. \tag{5.24}$$

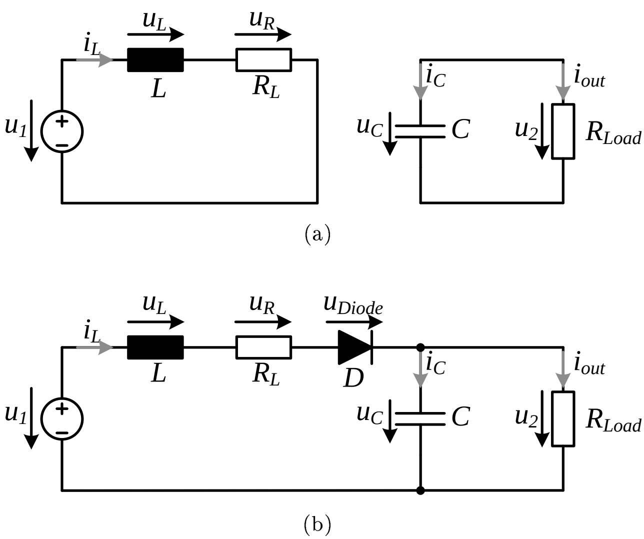

Figure 5.7: *Equivalent circuit for the half controlled 3-phase PWM boost rectifier for closed switch 5.7(a) and open switch 5.7(b) with* $L = 2(L_{gen} + L_{HCBR})$ *and* $R_L = 2(R_{gen} + R_{HCBR})$.

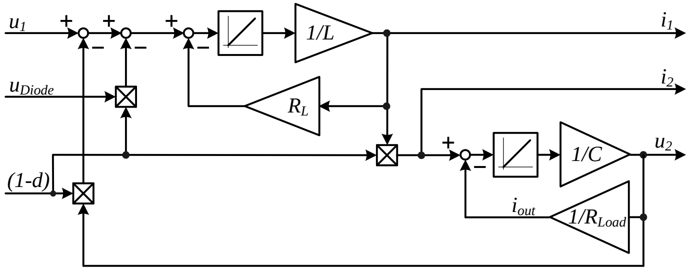

Figure 5.8: *Block diagram for the HCBR implemented in the Matlab/Simulink model shown in Figure 5.9.*

5.2.5 Compressed-Air-to-Electric-Power Model

In Figure 5.9 the structure of the Matlab/Simulink model of the overall system is shown schematically. The model is structured in two parts: The first part is the mechanical model which comprises the valve controller, valve, turbine, generator and the mechanical model. The second part is the electrical model consisting of the half controlled 3-phase PWM boost rectifier (HCBR) with the voltage controller and underlying current controller including the electric output power calculations. Simulation results and their comparison with measurements are presented in section 6.4.

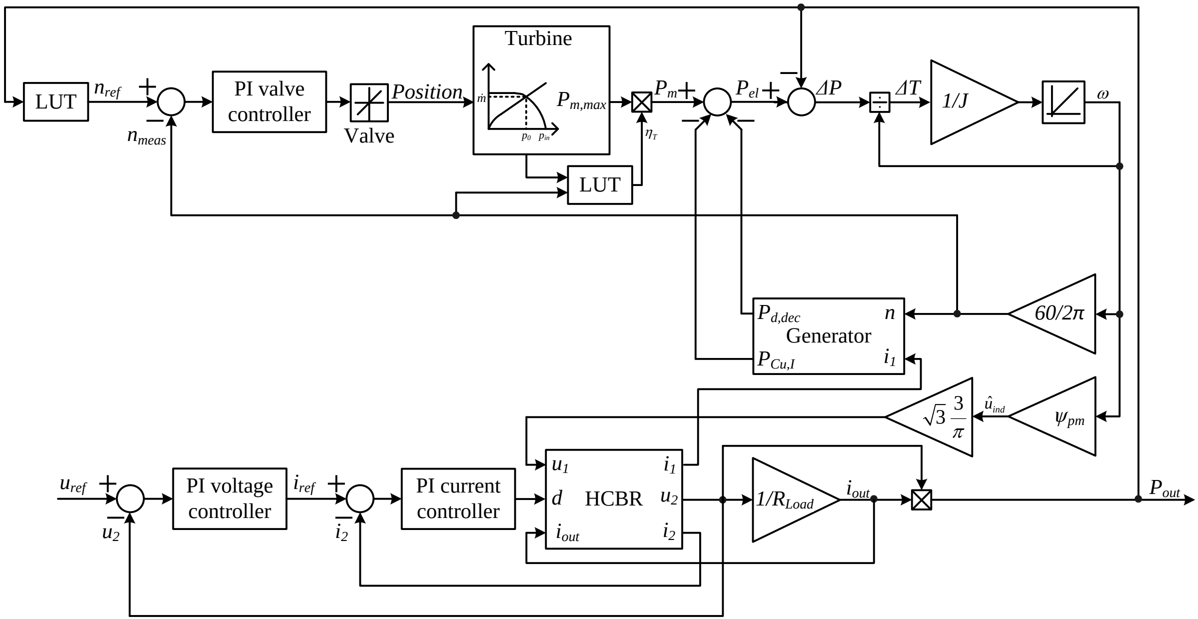

Figure 5.9: *Block diagram of the complete compressed-air-to-electric-power simulation model for Matlab/Simulink including the mechanical model and the electrical model.*

5.3 Control Electronics Implementation

The software, written in C-code on the DSP (TMS320F2808), can be subdivided into two parts; part one for the controlling of the HCBR, part two for the opening and closing of the valve. The setting of the operation point gets carried out by a state machine with six states, namely Idle, HCBR with sector modulation scheme, HCBR with synchronous modulation scheme, valve control and autonomous run (combination of valve control and the two HCBR modulation schemes).

For the control of the HCBR four interrupts with different execution frequencies and triggers have been implemented (light grey boxes in Figure 5.10):

- Analog-to-digital converter module A (ADC A) with an execution frequency of 200 kHz, samples the phase current, output voltage and output current and is triggered from the enhanced pulse width modulator module 1 (ePWM 1).
- PI current controller with an execution frequency of 200 kHz triggered from ADC A.
- PI voltage controller with an execution frequency of 100 kHz triggered from ePWM 1.
- Enhanced capture module 4 (eCAP 4) for sensorless sector detection and speed calculation with an execution frequency of six times the fundamental frequency and therefore triggered from zero crossing of the back emf.

The distribution of the calculated duty cycle to the three HCBR switches is executed in the function named `HCBRcontrol()`, regarding the modulation scheme and if necessary the sector.

For the valve control three interrupts with different execution frequencies and triggers have been implemented (dark grey boxes in Figure 5.10):

- Analog-to-digital converter module B (ADC B) with an execution frequency of 25 kHz. It samples the BLDC μ-motor phase current and is triggered from the enhanced pulse width modulator module 4 (ePWM 4).

- PI current valve controller with an execution frequency of 25 kHz triggered from ADC A.
- PI valve controller with an execution frequency of 30 Hz triggered from eCAP 1.

The proper distribution of the calculated duty cycle to the six switches used to control the BLDC μ-motor is executed in the function named `ValveControl()`.

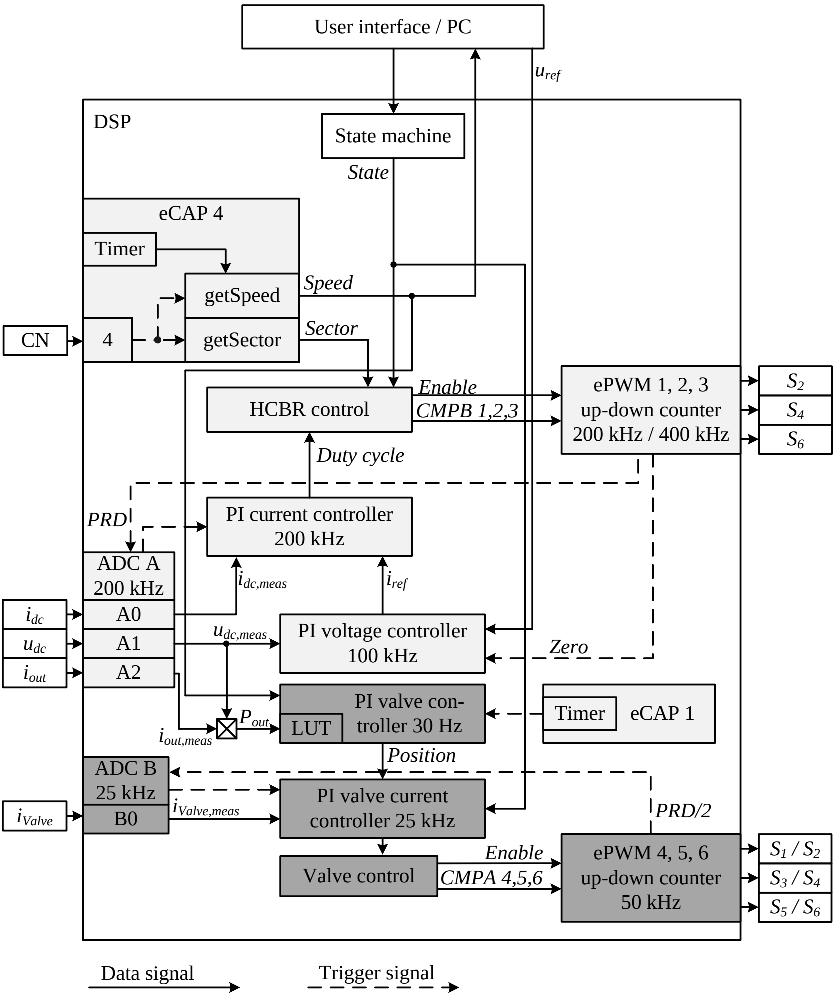

Figure 5.10: *Block diagram of the implemented Software.*

Chapter 6

Experimental Results of the Compressed-Air-to-Electric-Power System

In this chapter, experimental results of the the compressed-air-to-electric-power system from chapter 2 are presented, starting with measurements to characterize the axial Laval turbine and the generator, followed by measurements that show autonomous operation of the entire compressed-air-to-electric-power system including unpredicted load changes.

6.1 Experimental Setup

In order to verify theoretical considerations and the compressed-air-to-electric-power system concept, an experimental test bench, shown in Figure 6.1, was built. The goal of this first test bench setup was to characterize the axial Laval turbine and the generator, shown in Figure 6.2. It includes a mass flow sensor and several temperature and pressure sensors and a 3-phase variable resistive load. The compressed-air-to-electric-power system has been tested up to an inlet pressure of 600 kPa and a maximum outlet electric power of 124 W. For the measurements, the operating point is changed by varying the resistive 3-phase load and the supply pressure. The turbine and generator speed can be determined from the current waveform in the resistive load. With a 3-phase power analyser, the electric output power can be measured. In addition to input and output pressure, the input and output temperature of the air flow is measured. As expected, the efficiency can not be measured depending on the temperature drop because the turbine is not isolated well enough from the thermal losses of the generator and ball bearings. Assuming adiabatic flow through the turbine, the system efficiency can be calculated using

$$\eta_{system} = \frac{P_{el}}{\dot{m} c_p \Delta T_{(0-2s)}} \tag{6.1}$$

where c_p is the specific heat capacity, P_{el} is the electric output power and $\Delta T_{(0-2s)}$ is taken from (2.31). With the knowledge of the generator efficiency, the turbine efficiency can now be calculated as

$$\eta_T = \frac{\eta_{system}}{\eta_{gen}}. \tag{6.2}$$

The generator efficiency η_{gen} can be determined from the measured losses shown in Figure 6.3 plus the calculated copper losses

$$\eta_{gen} = \frac{P_{el}}{P_{el} + P_{d,dec} + P_{Cu,I}}. \tag{6.3}$$

6.2 Deceleration Test

Since the rotor critical speeds (section 3.3.2), and the interference fit of rotor sleeve and PM have been designed for a maximal speed of 500 000 rpm, the generator is first tested as a motor up to maximum speed. Thereby, the no-load losses $P_{d,dec}$ at the rated speed of 350 000 rpm (6.2 W) and at 500 000 rpm (13 W) were measured with the deceleration test (Figure 6.3). This method is based on the fact that in no-load operation (no electrical drive or break) the rotational energy is consumed by the losses, decreasing the rotational speed accordingly. The gradient of this deceleration is a measure of the losses. The dynamical equation for the

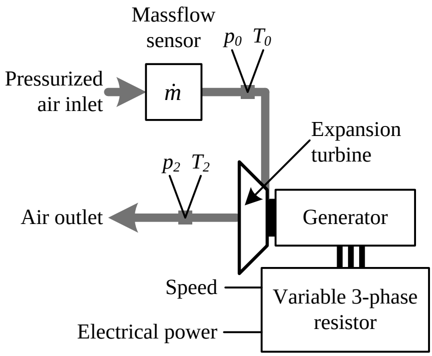

Figure 6.1: *Test bench setup used to characterize the axial Laval turbine and the generator.*

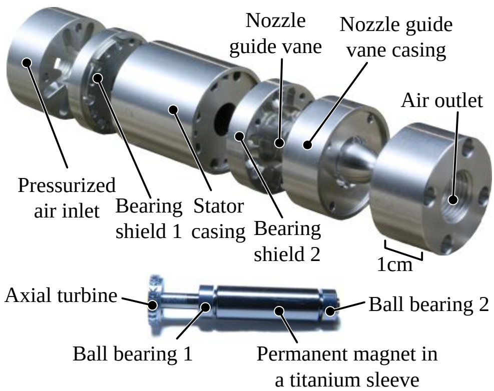

Figure 6.2: *Rotor with attached turbine and generator stator of the ultra-compact ($\varnothing$ 22 mm $\times$ 60 mm) compressed-air-to-electric-power demonstrator.*

rotor is

$$J\frac{d\omega}{dt} = -T_{d,dec} = -\frac{P_{d,dec}}{\omega} \tag{6.4}$$

where ω is the angular frequency, J the calculated rotor inertia ($23 \cdot 10^{-9}$ kg m^2, Table 3.1), $T_{d,dec}$ the no-load friction or breaking torque and $P_{d,dec}$ the no-load power losses. Not included in the deceleration test are the copper losses depending on the phase currents $P_{Cu,I}$. For determining the total losses the copper losses can be added according to (5.7) if the phase currents are measured during generator operation.

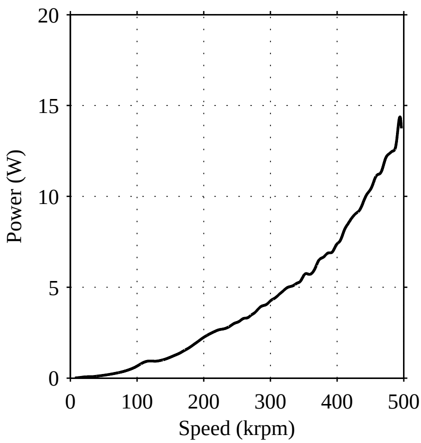

Figure 6.3: *Measured losses of the high-speed motor versus speed. The measured power losses include bearing losses, windage losses and core losses. For the total generator losses, the calculated copper losses must be added.*

6.3 Turbine Characteristics

In Figure 6.4 the measured and calculated mass flow through the turbine is plotted. It can be seen that the measured mass flow can be very well calculated with the flow function described in [45] and in (2.27). Also, the predicted dependence of mass flow (2.26) (and therefore input power) and supply pressure can be verified; the mass flow does not depend on

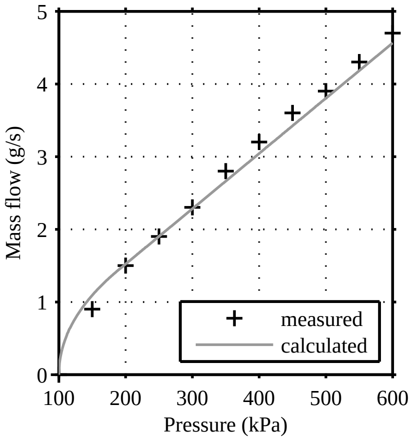

Figure 6.4: *Measured and calculated mass flow as a function of the inlet pressure.*

speed or load (2.33). Furthermore, it can be seen that the massflow increases linearly with input pressure after the pressure ratio ($p_2 = 100$ kPa, ambient pressure) is higher than the critical pressure ratio (2.29) $p_0/p_2 \geq 1.894$, which means that the flow mode is choked in the majority of the operating points. A maximal mass flow of 4.7 g/s at 600 kPa inlet pressure is achieved.

Figure 6.5 and Figure 6.6 show the electric output power and torque as a function of speed and supply pressure. The maximal electric power output is 124 W at 370 000 rpm and the maximal measured torque is 5 mNm at 240 000 rpm. An increase of the resistive load causes a decrease of the torque and therefore an increasing speed at a constant supply pressure. The turbine generator system has been tested up to 455 000 rpm and 600 kPa supply pressure. The operating point has been changed by varying the passive resistive 3-phase load and the supply pressure. The grey dashed line in Figure 6.5 represents the point with highest output power and therefore highest turbine efficiency.

Figure 6.7 and Figure 6.8 show the turbine and the system efficiency as a function of speed and supply pressure. The maximum turbine efficiency is about 28%, while the maximum system efficiency is 24%. The maximum turbine efficiency is not as high as assumed in section 2.4.3.

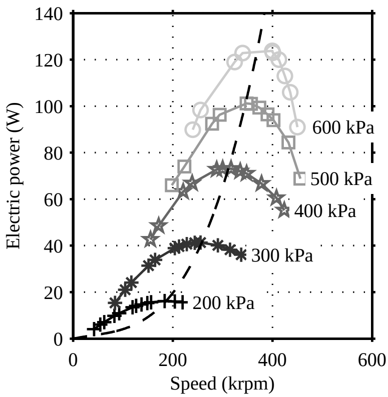

Figure 6.5: *Measured electrical power generated by the turbine and generator system as a function of speed and supply pressure.*

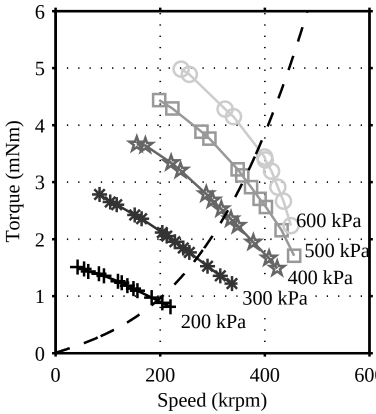

Figure 6.6: *Measured torque generated by the turbine as a function of speed and supply pressure.*

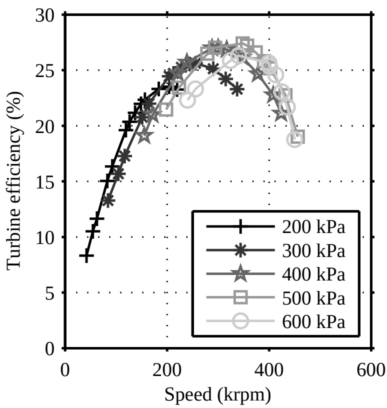

Figure 6.7: *Turbine efficiency as a function of speed and inlet pressure.*

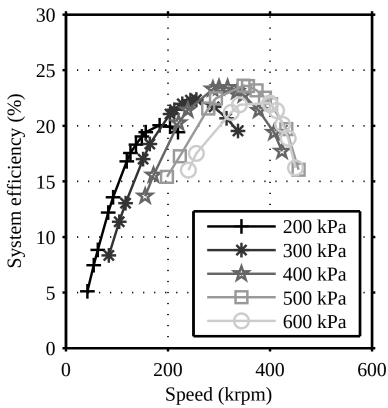

Figure 6.8: *System efficiency as a function of speed and inlet pressure.*

This is mainly due to the large tip clearance and the absence of a shrouding band. It can be seen that the highest turbine efficiency lies between 300 000 rpm and 350 000 rpm, which is near the design point, and an input pressure between 400 kPa and 500 kPa.

Exchanging the variable 3-phase load by a rectifier controlling the output to a fixed dc voltage takes significant influence on stable working points. Only working points on the right hand side of the line indicating highest efficiencies in Figure 6.5 are stable.

6.4 Autonomous Operation

For the autonomous operation measurements a similar test bench as in Figure 6.1 has been used. Additional to the measured pressures, temperatures, speed, electric output power and massflow, the valve position, the dc-output voltage and the pressure between valve and turbine were measured. Also the 3-phase variable resistive load was exchanged with a variable resistor connected to the rectifier output. During steady-state operation of the compressed-air-to-electric-power system the valve is at a constant position and therefore not consuming any power. More interesting are the unpredicted load ramp or steps. In Figure 6.9 simulated and experimental data with an unpredicted load ramp (duration of 3 s) starting from 5 W and ending at 40 W electric output power is presented. The compressed-air-to-electric-power system was simulated using the Matlab/Simulink model shown in Figure 5.9. In the simulated valve position curve and the simulated speed curve, seven steps can be noticed, occurring when the reference speed, defined by the output power and the corresponding LUT (cf. Figure 5.6 and Figure 5.9) is set to a higher value. The output voltage was controlled with the HCBR using the sector modulation scheme (cf. section 4.3.3).

In Figure 6.10 simulated (black) and experimental (grey) data with an unpredicted load step change from 10 W to 40 W electric output power is presented. The measured and simulated systems show good agreement; however, the valve opening speed is slightly slower than the predicted valve speed and has a dead time, which occurs from the lowpass filter used for the speed measurement. Also the measured speed shows a higher speed decrease than predicted. Reasons for this are the not well known and lifetime dependent bearing losses as well as the measured turbine efficiency which may have decreased during lifetime. Also the predicted pressure drop over the valve, and therefore turbine input pressure, may differ from the calculated. The output power is calculated from the output current i_{out}, measured with an additional shunt (cf. Figure 4.12). The experimental output power was controlled with the HCBR using sector modulation scheme (cf. section 4.3.3).

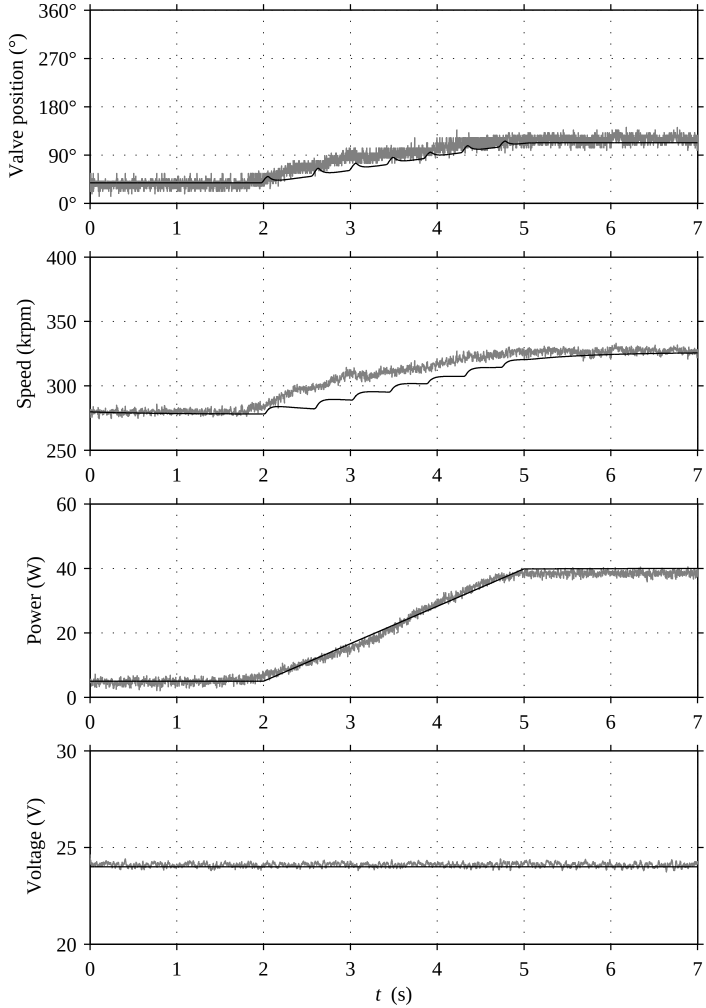

Figure 6.9: *Simulated (black) and experimental (grey) data with an unpredicted load ramp (duration of 3 s) starting from 5 W and ending at 40 W electric output power. Shown are the valve position, speed, electric output power and the constant output voltage of 24 V.*

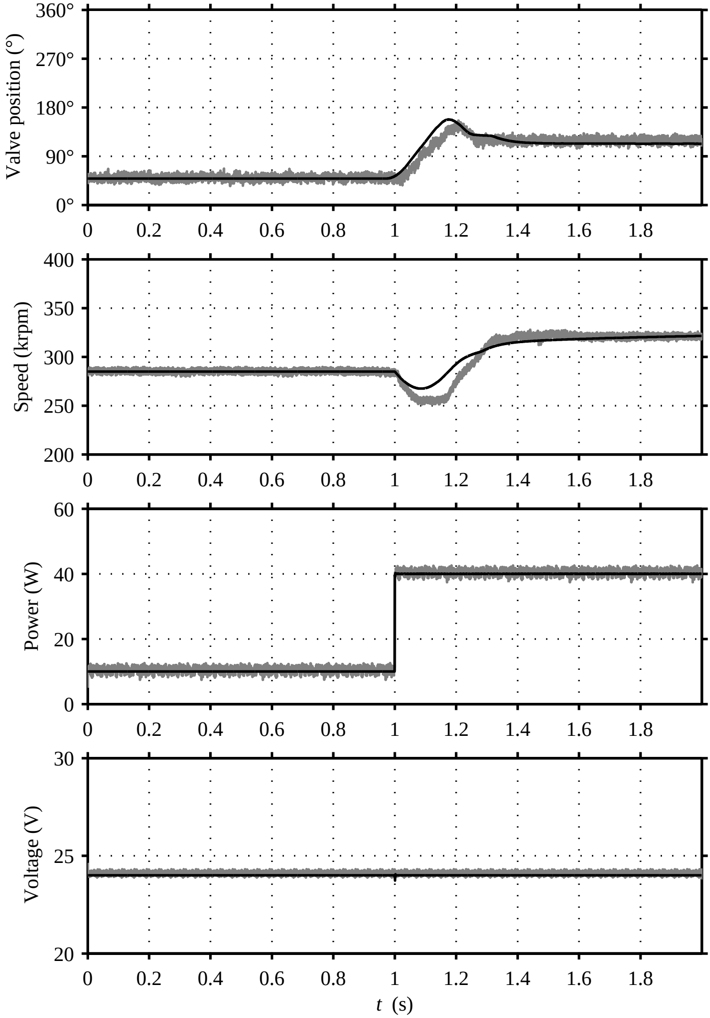

Figure 6.10: *Simulated (black) and experimental (grey) data with an unpredicted load step change from 10 W to 40 W electric output power. Shown are the valve position, speed, electric output power and the constant output voltage of 24 V.*

Chapter 7

Reversal of One-Stage Radial Turbocompressor

In order to compare radial turbines and axial turbines for a compressed-air-to-electric-power system an existing radial turbocompressor [34] is reversed. In this chapter, experimental results of the reversal of an existing electric motor-driven compressor system is presented.

7.1 System Description

The compressed-air-to-electric-power system under investigation is shown in Figure 7.1 and Figure 7.2 respectively, and has a rated rotational speed of 490 000 rpm and a rated power output of 150 W. It is based on the reversal of an existing electric motor-driven compressor system [34], which reaches a maximum pressure ratio of 1.6 at a maximum rotational speed of 550 000 rpm with a power input of 150 W.

Replacing the vane-less compressor diffuser with guide vanes, the electrically driven compressor system can be reversed and operated as a turbine-generator system. The original inward-flow radial (IFR) compressor is thereby running backwards as a turbine. The system further includes a similar PM generator as described in section 3.1, while in Table 7.1 the rated and measured electrical data of the PM motor are

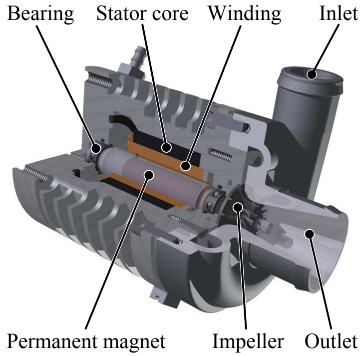

Figure 7.1: *Cut-away view of the compressed-air-to-electric-power generation system: diametrically magnetized cylindrical PM rotor inside a slotless stator. Outer dimensions: 33 × 43 mm.*

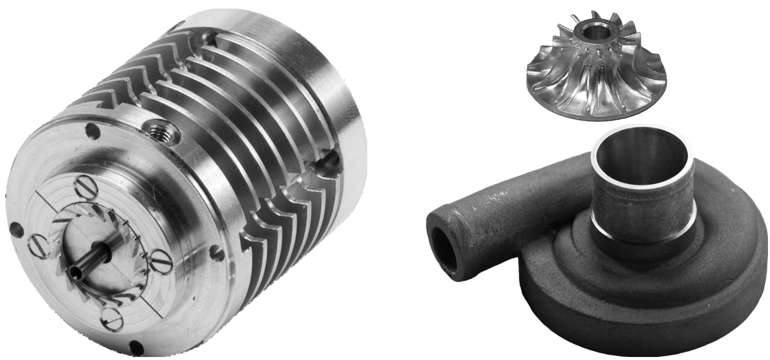

Figure 7.2: *PM generator with stator guide vanes, spiral casing and radial turbine (impeller diameter = 10.5 mm).*

summarized.. The PM generator and turbine have a total volume of 36.8 cm^3 (d = 3.3 cm, l = 4.3 cm), which leads to a power density of 4 W/cm^3. A detailed analysis and description is given in [74] and [75].

For the existing turbo compressor system, a detailed electromagnetic machine design, an analysis of the mechanical stresses and rotor dynamics and a thermal design have already been performed [34]. These design considerations are also valid for the compressed-air-to-electric-power system, and only the thermodynamic design and the guide vanes have to be modified.

Description	Parameter	Value
Rated speed	n_r	490 000 rpm
Rated electric output	P_{el}	150 W
Magnet flux linkage	Ψ_{PM}	0.22 mVs
Back emf at rated speed	u_{emf}	11.2 V
Stator inductance	L_S	2.25 µH
Stator resistance	R_S	0.125 Ω
Machine efficiency	η_m	87%

Table 7.1: *Electrical data of the IFR turbine-generator system.*

7.2 Turbomachinery Considerations

The system was originally designed as an electrically driven compressor. Therefore, the dimensions of the impeller are given, especially the inlet and outlet angle of the rotor blades. For this reason, the stator guide vanes have to be adjusted to meet optimum efficiency at a rated rotational speed of 490 000 rpm. Since the inlet angle of the turbine blade is zero, the relative velocity w_1 has to be orthogonal to the rotational speed u_1 (Figure 7.3(a)).

The complete adiabatic expansion process for a turbine is represented by the enthalpy-entropy diagram (Mollier diagram), shown in Figure 7.4. The ideal enthalpy change ($\Delta h_{(0-2s)}$), i.e. the ideal or reversible expansion, is in between the inlet and outlet pressure, but at constant entropy (line $0 - 1s - 2s$). Assuming adiabatic flow through the turbine, the

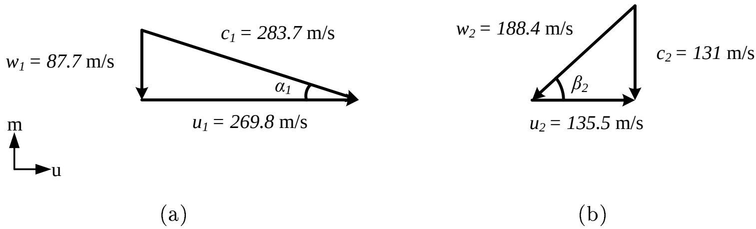

Figure 7.3: *Velocity diagrams at rotor entry (7.3(a)) and outlet (7.3(b)) for the rated rotational speed.* c_1/c_2 *absolute velocity at rotor inlet/outlet.* w_1/w_2 *relative velocity at rotor inlet/outlet.* u_1/u_2 *stator speed at radius* r_3 *and* $\bar{r}_{4,5}$.

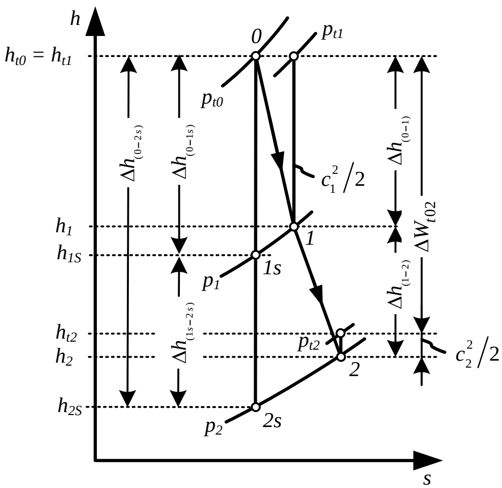

Figure 7.4: *Enthalpy entropy diagram (hs-diagram); The specific work can be written with Euler's equation* (2.5) *as:* $w_{12} = u_1 c_{u2} - u_2 c_{u1} = -u_1^2$.

corresponding temperature drop $\Delta T_{(0-2s)}$ can be calculated as

$$\Delta T_{(0-2s)} = T_0 \left[1 - \left(\frac{p_{t0}}{p_2} \right)^{\frac{1-\kappa}{\kappa}} \right] = 73.6 \text{ K} \tag{7.1}$$

where κ is the ratio of specific heats. The non-dimensional Euler work coefficient can be calculated as

$$\lambda_{Euler} = \frac{u_2}{u_1} \frac{c_{u2}}{u_1} - \frac{c_{u1}}{u_1} = -1 \tag{7.2}$$

where u_1 and u_2 are the circumferential speed at radii r_1 and r_2 respectively while $c_{u1} = u_1$ and $c_{u2} = 0$ are the circumferential component of the absolute velocities. The actual expansion follows the line $0-1-2$. The temperature drop ΔT_2 can be calculated with the assumed isentropic efficiency η_s, which can be estimated from correlations of experimental data and is supposed to be 70%

$$\Delta T_2 = \Delta T_{(0-2s)} \eta_s = 51.5 \text{ K} \rightarrow \mathrm{T}_2 = 248.5 \text{ K}. \tag{7.3}$$

In an adiabatic turbomachine, the flow work determines the change of enthalpy. The losses (dissipation work) are uniquely caused by the increase in entropy of the fluid. The stator temperature drop T_{0-1} can be calculated via the specific kinetic energy of the absolute velocity at rotor entry c_1

$$\Delta T_{(0-1)} = \frac{\Delta h_{(0-1)}}{c_p} = \frac{c_1^2}{2 c_p} = 40.1 \text{ K} \tag{7.4}$$

where c_p is the specific heat capacity. As a result of miniaturization, and therefore a larger influence of side friction, the guide vane efficiency η_n was assumed to be 90%. Therefore the isentropic stator temperature drop T_{0-1s} can be calculated as

$$\Delta T_{(0-1s)} = \frac{\Delta h_{(0-1)}}{c_p \eta_n} = \frac{c_1^2}{2 c_p \eta_n} = 44.5 \text{ K}. \tag{7.5}$$

The pressure p_1 in between the stator and rotor can now be calculated as

$$p_1 = p_{t0} \left(1 - \frac{T_{(0-1s)}}{T_0} \right)^{\frac{\kappa}{\kappa-1}} = 171 \text{ kPa}. \tag{7.6}$$

Description	Parameter	Value
Inlet temperature	T_0	300 K
Inlet pressure	p_{t0}	300 kPa
Outlet pressure	p_2	112 kPa
Guide vane efficiency	η_n	90%
Isentropic efficiency	η_s	70%
Effective turbine inlet area	A_{u1}	17 mm^2
Effective turbine outlet area	A_{u2}	19.5 mm^2

Table 7.2: *Thermodynamic and turbine data.*

In Figure 7.5, the layout of the stator and the rotor is plotted. From the rotor inlet (r_3), the rotor blades extend radially inward and turn the flow the axial direction. The exit part of the blades is curved to remove the absolute tangential component of velocity. In Figure 7.3(b), the velocity diagram for the turbine outlet is drawn. The air gap between the radial turbine and the spiral casing has to be as thin as possible, in order to minimize the tip leakage losses. The mass flow rate through the turbine can be written as

$$\dot{m} = \rho_1 c_{m1} A_{u1} = \left(\frac{p_1}{RT_1}\right) w_1 A_{u1} = 3.4\ \frac{\text{g}}{\text{s}} \tag{7.7}$$

where R is the ideal gas constant. The effective turbine inlet area A_{u1} also accounts for the rotor blade thickness. The maximum mechanical output power of the turbine can now be calculated as

$$\begin{aligned} P_m =& \dot{m}\frac{1}{2}\left[\left(c_1^2 - c_2^2\right) + \left(u_1^2 - u_2^2\right) + \left(w_2^2 - w_1^2\right)\right] \\ =& \dot{m}\left(u_2 c_{u2} - u_1 c_{u1}\right) \\ =& -\dot{m}u_1^2 = -248\ \text{W} \end{aligned} \tag{7.8}$$

where $c_{u1} = u_1$ and $c_{u2} = 0$ m/s. From this value, the leakage losses, the tip clearance losses and the side friction of the turbine back disc are deducted, leading to a maximum measured turbine power output of 212 W. In Table 7.2, the calculated thermodynamic and turbine data are summarized.

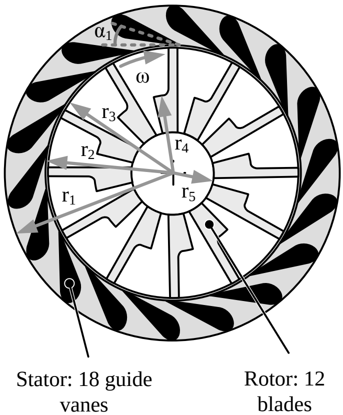

Figure 7.5: *Radial turbine* (r_1 : 7 mm, r_2 : 5.335 mm, r_3 : 5.25 mm, r_4 : 3.3 mm, r_5 : 1.75 mm, α_1 : 18).

7.3 Test Bench Setup

The test bench setup for the reversal of the electric motor-driven compressor system has been described in section 6.1 and is shown in Figure 6.1. The system has been tested up to an inlet pressure of 300 kPa and a maximum outlet electric power of 170 W. The pressurized-air-to-electric-power efficiency has been calculated using (6.1) while $\Delta T_{(0-2s)}$ is taken from 7.1.

7.4 Measurements

First, the motor has been tested without load up to a maximum speed of 550 000 rpm, and the bearing, windage and core losses were measured with the deceleration test, described in section 6.2 (Figure 7.6). Not included in the deceleration test are the copper losses depending on the phase currents, but they can be calculated accurately with the measured phase resistance R_s (Table 7.1) and added to the measured generator losses. With this, the generator efficiency is determined.

In the second step, the impeller and inlet housing are mounted. Figure 7.7 and Figure 7.8 show the torque and the electric output power as a function of speed and supply pressure. The maximum electric power output is around 170 W at 495 000 rpm, and the maximum measured torque is 5.2 mNm at 295 000 rpm. An increase in the 3-phase resistance causes a decrease in the torque and therefore an increasing speed at a constant supply pressure. Figure 7.9 shows the turbine efficiency as a function of speed and supply pressure. The maximum turbine efficiency is around 52%, while the maximum system efficiency (turbine and generator) is 43%.

7.5 Comparison

Comparing radial turbines (chapter 7 and [76]) with axial impulse turbines such as in chapter 6 and in [21], the turbine efficiency (52% versus 28% and 18% respectively) and the system efficiency (43% versus 24% and 10.5% respectively) are higher for the radial turbine. This is because radial turbines generally have higher efficiency than axial impulse turbines. However, the drawbacks are the manufacturing and the controlling of tolerances, which are more difficult. The maximum generator efficiency in chapter 6 is 83% and significantly higher compared to the generator efficiency presented in [25] (28%). In order to further increase the efficiency of the used radial or axial turbine the tip clearance could be further reduced, which implies increased requirements to the concentricity of the turbine, turbine casing and the generator casing. Besides this the use of a shrouding band for tha axial turbine could be investigated.

In [25] and [27], µ-generators are driven with simple air-driven turbines and therefore only the generator power density is presented. Therefore, comparing the generator power densities of the different systems, it can be seen that the traditionally fabricated generators, as in chapter 6 and chapter 7 have power densities in the same range (11 $\frac{W}{cm^3}$ versus 6 $\frac{W}{cm^3}$), while generators that have electroplated surface windings and are made using deep lithography or silicon etching, as in [25], [26] and [27] have power densities up to 59 $\frac{W}{cm^3}$. On the other hand, the maximum electric output is clearly higher with traditionally fabricated systems (124 W and 170 W versus 5 W and 8 W). Also the generator efficiencies of [25] and [27] (28% and 66%) are much lower than that in the high-speed generator used in the system presented in this thesis (83%).

In summary for power outputs higher than 20 W, traditionally fabricated generator systems consisting of a radial 2D- or, for higher power, 3D-turbine are the only choice. A 2D-turbine has also advantages in manufacturing (etching or milling) and simple tip clearance control.

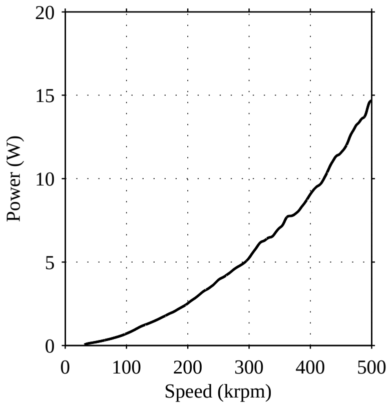

Figure 7.6: *Measured losses of the high-speed motor versus speed. The measured power losses include bearing losses, windage losses and core losses. For the total generator losses, the calculated copper losses are added.*

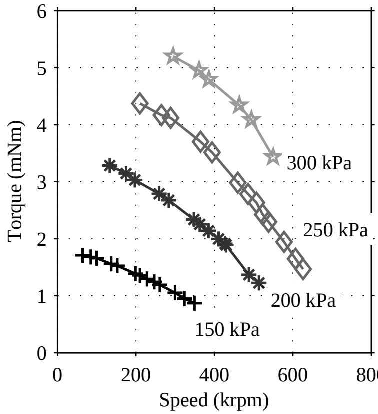

Figure 7.7: *Measured torque generated by the turbine as a function of speed and supply pressure.*

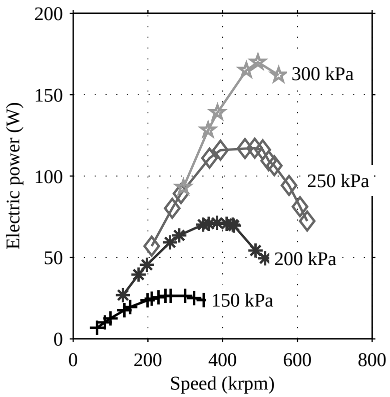

Figure 7.8: *Measured electrical power generated by the turbine and generator system as a function of speed and supply pressure.*

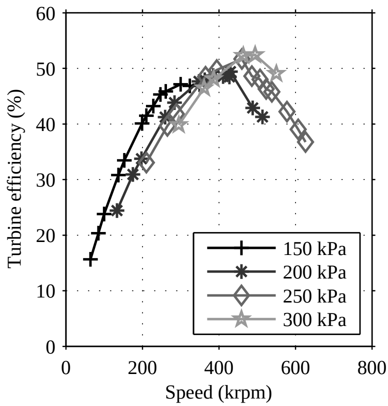

Figure 7.9: *Measured turbine efficiency as a function of speed and inlet pressure.*

Chapter 8

Two-Stage, Electrically Driven Turbocompressor

The reversal of a compressed-air-to-electric-power system to an electric-power-to-compressed-air system is a promising research area. In this chapter, a miniature two-stage electrically driven turbocompressor system designed for the application in the Solar Impulse airplane is presented [77].

8.1 Introduction

The Solar Impulse project, initiated in the year 2003, has the ambitious goal to construct and build an airplane that can fly around the world, purely powered through sun energy. The Solar Impulse airplane will fly in altitudes above 10 000 m, mainly because of two reasons: Firstly, the solar radiation is less influenced through the atmosphere and through less clouds also less shadowing effects and therefore higher electric output power of the photovoltaic cells. Secondly, due to the higher altitude more potential energy and thus a longer gliding flight during the night is possible. Because of the dramatically reduced air pressure (Figure 8.1(a)) and therefore also oxygen concentration at these high altitudes, the Solar Impulse airplane requires a pressurized cabin and a cabin pressurization control system for the preparation of fresh air. A turbocompressor

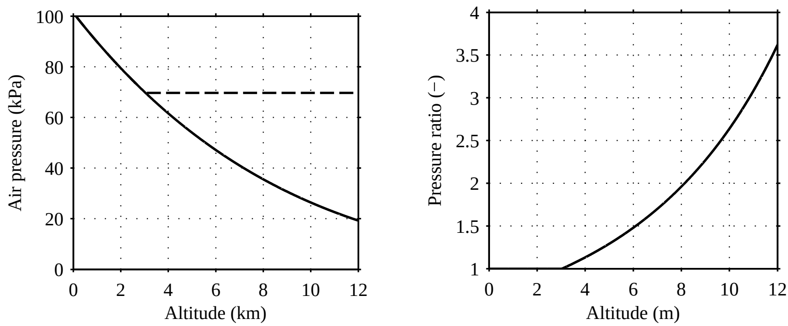

(a) (b)

Figure 8.1: *Air pressure and resulting pressure ratio as a function of altitude. The dashed line in 8.1(a) indicates the minimum pressure that should remain in the cabin of the Solar Impulse airplane.*

system is due to the high power density smaller and lighter than a normal cabin air pressurization system, but the rotational speed lies around 500 000 rpm, at a power rating of approximately 150 W. Because of the mentioned reasons, a pressurized air cabin system based on a micro turbocompressor qualifies for this project, also because the low weight of the turbocompressor positively influences the energy demands of the airplane.

8.2 System Specifications

The two-stage electrically driven turbocompressor has a rated rotational speed of 500 000 rpm, a calculated air pressure ratio of 2.25 and a mass flow of 1 g/s at ambient conditions for temperature and inlet pressure. As mentioned above the system is designed for the cabin air pressurization system of the Solar Impulse airplane [35], but the specifications are in the area of the other applications mentioned in section 1.2.8. The design is based on a one-stage electrically driven compressor built as a first prototype [34]. The two-stage version of the compressor is required for an increase in pressure ratio. This is necessary because the maximum flying altitude of the Solar Impulse airplane will be around 10 000 m,

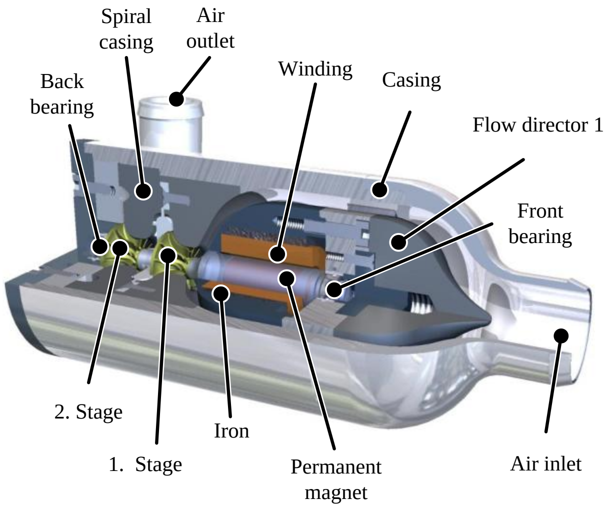

Figure 8.2: *Cross section view of the integrated two-stage electrically driven turbocompressor system.*

where a pressure ratio of 2.6 is required (Figure 8.1(b)). The system is shown in Figure 8.2 and Figure 8.8, it is comprised of two radial impellers, a PMSM and the power and control electronics.

A detailed description of the machine design has been presented in chapter 3, while the optimization process for the electrical machine has been presented in [53]. Therefore only calculated machine data and calculated machine losses are summarized in Table 8.1.

8.3 Turbomachinery Design

A radial compressor was chosen, because this type of compressor can generate high pressure ratios at low mass flows with a single stage. However, to achieve the design goal for the pressure ratio of 2.25 at a very low mass flow of 1 g/s, a two-stage design is employed [78]. The biggest challenges are the manufacturing of the impeller and the fitting between the different pieces, especially impeller and casing, the mechanical rotor design and the rotor dynamics. This is because the manufacturing tolerances

Description	Parameter	Value
Rated speed	n_r	500 000 rpm
Rated electric power		
inlet temperature 220 K	P_{el}	150 W
inlet temperature 300 K	P_{el}	350 W
Rated torque	T_r	2.86 mNm
Inertia	J	$22 \cdot 10^{-9}$ kg m^2
Rated machine temperature	T	120°C
Magnet flux linkage	Ψ_{pm}	0.265 mVs
Back emf at rated speed	u_{emf}	13.9 V
Stator inductance	L_S	3.3 μH
Stator resistance	R_S	0.12 Ω
Copper losses		
Inlet temperature 220 K	P_{Cu}	6.8 W
Inlet temperature 300 K	P_{Cu}	34.4 W
Iron losses	P_{Fe}	0.7 W
Air friction losses	P_{Air}	5 W
Bearing losses (per Bearing)	P_{Bng}	5 W
Total losses (with bearing)		
Inlet temperature 220 K	P_t	22.5 W
Inlet temperature 300 K	P_t	50.1 W
Machine efficiency (low pressure)		
Inlet temperature 220 K	η_m	93.6%
Inlet temperature 300 K	η_m	85.7%

Table 8.1: *Calculated electrical machine data and losses.*

Description	Parameter	Value
Rated speed	n_r	500 000 rpm
Rated pressure ratio	π	2.25
Rated mass flow	$\dot{m}$	1 g/s
Compressor efficiency	η_s	74%
Turbocompressor length	l_c	80 mm
Turbocompressor diameter	d_c	35 mm
Total weight	m	140 g

Table 8.2: *Turbomachinery data.*

cannot be decreased proportional with the downscaling and therefore the leakage losses become more dominant for small compressors. This means that the chosen tip clearance (100 μm) is rather high. For a further investigation of the influence of the tip clearance, the clearance of the first stage can be adjusted between 0 μm and 100 μm.

The first impeller consists of 12 blades (no splitter blades) and has a mean streamline diameter at the inlet of 5.28 mm, while the outlet diameter is 10.5 mm. At the outlet of the first stage return channels guide the air to the second stage and thereby take out the circumferential component of the velocity $c_{u1} = 0$. This means no angular momentum at the inlet of the second stage. The second impeller consists of 12 blades and additional splitter blades and has a slightly smaller mean streamline diameter, while the outlet diameter remains the same. After the flow leaves the second stage, it enters the vane less diffuser and then gets collected in a volute and thereby guided into the exit flange. The two compressor stages are directly mounted with a shrink fit onto the motor rotor shaft as shown in Figure 8.8(b). Between the two stages, a spacer sleeve is mounted, and the back bearing seat is shrink fitted onto the rotor.

According to the results from the one-stage turbocompressor [34], the design pressure ratio is 2.25 at a mass flow of 1 g/s, which is calculated to be achieved at a rotational speed of 500 000 rpm. The power consumption is depending on the mass flow and the inlet temperature of the air; at the design operating point it is 350 W at laboratory conditions. The compressor data is compiled in Table 8.2.

8.4 System Integration

Besides the design of the individual components, an analysis of the mechanical stresses and rotor dynamics of the common rotor of electrical machine and turbomachine, and a thermal design of the entire system are needed. The critical speeds of the rotor are depicted in Figure 8.3. The length of the shaft is adjusted such that the rated speed falls between the second and the third critical speed. In order to reduce losses and to have enough space for the flow director after the first stage the spacing between the two stages should be as big as possible. However, the third critical speed, which limits the maximum speed, is reduced with an increase of the rotor length. Therefore, the space between the two stages is limited. The critical speeds calculations have been made during the machine optimization process with an analytical approach. The final rotor dynamic design has been verified with 3D FE simulations. The torsional vibration modes are much higher than the critical speeds and have therefore not been added to the rotor dynamic analysis.

The main cooling of the motor and the bearings is due to the air flow; the input air first circulates around the motor and bearing 1 and thereby provides cooling. Because of this special design no additional cooling fins are needed to guarantee safe operation under laboratory conditions. The most critical spot is ball bearing 2 (c.f. 8.4), which produces high losses and has worse cooling conditions than bearing 1. The maximal allowed temperature in the bearings is 200°C. A thermal FE analysis of the integrated system under laboratory conditions, including the calculated losses, can be found in cross-section view in Figure 8.4. It can be seen that the temperatures in ball bearing 2 do not exceed 110°C.

8.5 Inverter Design

The bi-directional pulse amplitude modulation (PAM) inverter consists of a standard 3-phase inverter, an additional buck converter and a DSP-based control system. The inverter part is controlled in six-step or block commutation mode, which means that each switch is conducting for 120° electrical degrees, and therefore, switched with the fundamental frequency of the machine. The phase currents are controlled via the dc/dc buck converter. The dc-current is measured for the torque con-

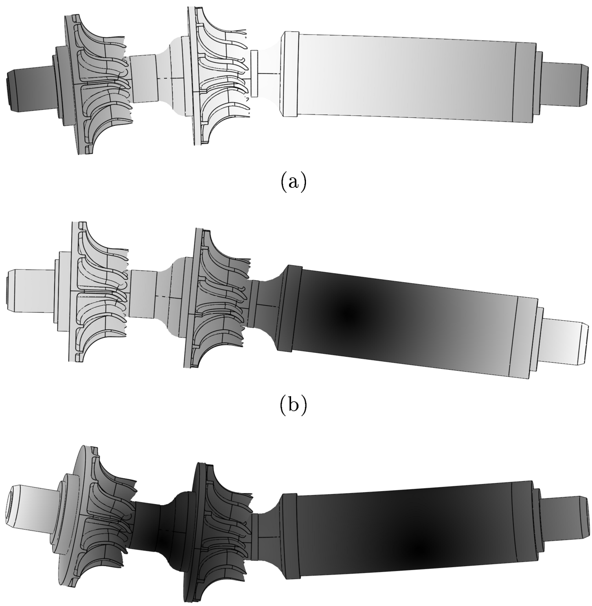

(a) (b) (c)

Figure 8.3: *Critical speeds of the two-stage miniature turbocompressor rotor. First critical speed at 2.6 kHz, 156 krpm 8.3(a), second critical speed at 5.9 kHz, 354 krpm 8.3(b), and third critical speed at 12 kHz, 720 krpm 8.3(c). The grey scale shows the displacement: no displacement (black), maximal displacement (white).*

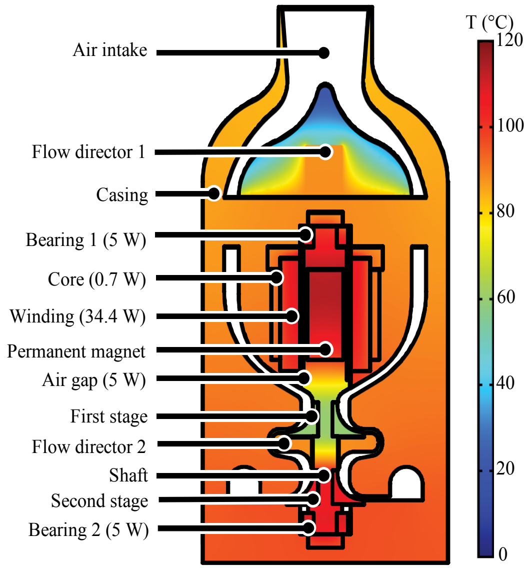

Figure 8.4: *FE simulations of the temperature distribution under laboratory conditions, at 500 000 rpm and a drive power of 350 W, assuming an inlet temperature of 300 K.*

troller, while the stator voltages are measured for the sensorless rotor position detection and for the speed controller. Using a sensorless rotor positioning technique eliminates the disadvantages of rotor position sensors, such as an increased failure probability and an axial extension of the rotor. Especially a longer rotor is unwanted in this application because the critical speeds are lowered. For an inverter with block commutation, the back emf can directly be measured during the 60° electrical degrees off intervals in each phase.

The power electronics (dc/dc buck-converter and 3-phase inverter) have a measured efficiency of 90% at rated power of 150 W and of 82% at 350 W respectively. At rated power only passive cooling is necessary, however under laboratory conditions a higher output power of 350 W is required and therefore forced air cooling is used at this operating point. The block diagram of the inverter and the control system is depicted in

Figure 8.5, while further information has been presented in [46].

Due to the sinusoidal back emf, only the fundamental current waveform contributes to the average torque generation. The instantaneous torque can be calculated as (with $L_d = L_q$)

$$T_e = \frac{3}{2} i_q \Psi_{pm} = \frac{3\sqrt{3}}{\pi} i_{dc} \Psi_{pm} \tag{8.1}$$

where T_e is the resulting torque, Ψ_{pm} is the magnet flux linkage, i_q the current orthogonal to the direction of the rotor flux linkage (reference frame fixed to the rotor) and i_{dc} the dc current in the buck inductor L_{dc} (cf. Figure 8.5). The non-sinusoidal phase currents produce a torque ripple. However, for a turbocompressor application, this torque ripple is negligible due to the high inertia compared to the torque ripple variation, which only leads to a very small speed ripple when the inertia J is sufficiently high. This relation can be computed as

$$J \frac{d\omega}{dt} = T_e - T_b \tag{8.2}$$

where T_b is the breaking torque. The usual problem of noise and vibration due to a high torque ripple is outweighed by the noise and vibration of the turbocompressor.

8.6 Test Bench Setup

An experimental test bench is built in order to verify theoretical considerations and the feasibility of such ultra-compact ultra-high-speed electrically driven turbocompressor systems (Figure 8.6). Therefore, two valves are connected to the compressor inlet and outlet respectively for setting the input and output pressure conditions. When the first valve is fully open, the second valve acts as a variable load, and therefore measurements in over pressure condition can be performed. For low pressure conditions the second valve is open and the input pressure is adjusted using the first valve. A pressure sensor and a thermocouple are placed between the compressor output and the valve. At the compressor inlet a pressure sensor, a thermocouple and a mass flow sensor are used. Additionally, two thermocouples are used to monitor the power electronics and motor winding temperature. Due to the fact that the motor is of

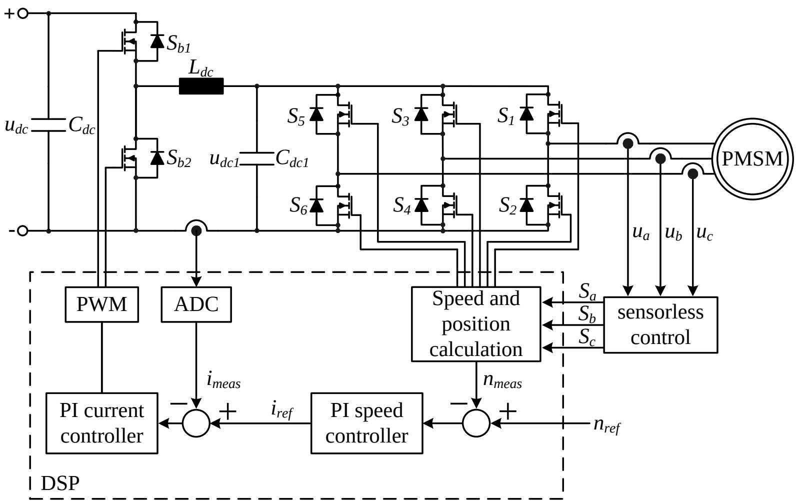

Figure 8.5: *Pulse amplitude modulation (PAM) power electronics and control system for driving an ultra-high-speed PMSM.*

synchronous type, the speed does not have to be measured separately. All measured data is collected by the DSP-based control system and is transmitted to a PC for online and offline analysis.

8.7 Measurements

The flux density in the air gap is 0.4 T and 1.05 T in the iron core respectively. Considering the rated torque and the rotor inertia in Table 8.1 the maximal acceleration ($dn/dt = \frac{T_r}{J}$) is 830 krpm/s. However, the dynamic performance of the speed controller has been limited to 40 krpm/s, in order to prevent additional friction in the ball bearings.

First, the compressor map depicting the pressure ratio versus mass flow for different rotational speeds is measured. Two different tip clearances are tested (35 μm and 70 μm) and both over and low pressure conditions are verified. In Figure 8.9 it can be seen that at rated speed of 500 000 rpm a pressure ratio of 1.95 is achieved with a tip clearance of 35 μm, while the maximum pressure ratio drops to 1.9 with a tip

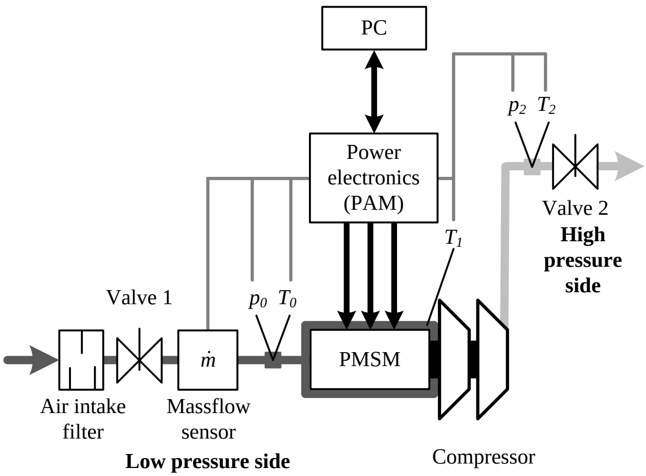

Figure 8.6: *Test bench setup including massflow sensor, two valves (for over and low pressure) and two thermocouples for temperature monitoring.*

clearance of 70 μm (Figure 8.11). This is lower than the prediction of 2.25. One main factor for this difference is the mechanical tolerances in the manufacturing which are not sufficiently small yet, which results in leakage and secondary air flow. Also, the two-stage design needs a flow director with small radii between the two stages, which leads to additional pressure drop, compared to the one-stage turbocompressor system. In Figure 8.10 and Figure 8.12 the electric power consumption of the turbocompressor system is shown.

In Figure 8.7 the maximal pressure ratios of the one and two-stage compressors are compiled. It can be seen that the predicted pressure ratio of the two-stage compressor of 2.25 is reached at a speed of 600 000 rpm, while the one-stage compressor would reach this ratio at 800 000 rpm, which is clearly too high for ball bearings.

The compressor isentropic efficiency can be calculated from the measured pressure ratio and the input and output air temperatures with

$$\eta_i = \frac{T_1 \left[\left(\frac{p_2}{p_1} \right)^{\frac{\kappa - 1}{\kappa}} - 1 \right]}{T_2 - T_1} \tag{8.3}$$

where κ is the adiabatic exponent. The input air temperature measurement is located directly before the first compressor stage in order not to include the air heating by the motor. Due to the compact design it is not possible to measure the temperature between the first and second stage, therefore, no individual stage efficiencies can be measured. The measured efficiency at the operating point (500 000 rpm and 1 g/s) is 60%. This is lower than the calculated efficiency of 74% due to the same reasons as for the difference in measured and calculated pressure ratio, and can be increased by decreasing the tip clearance or a redesign of the second flow director or the impellers.

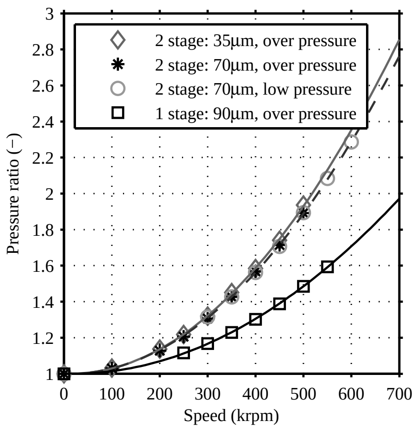

Figure 8.7: *Measurements and interpolation of maximal pressure ratio for over pressure and low pressure conditions and for 70 µm and 35 µm clearance. The black line indicates the maximal pressure ratio for the one-stage compressor [34] for a clearance of approximately 90 µm.*

(a)

(b)

(c)

Figure 8.8: *Miscellaneous components of the miniature two-stage electrically driven compressor 8.8(a), the assembled miniature two-stage rotor 8.8(b) and the power and control electronics including measurements of massflow, pressure and temperature (80 × 80 × 47 mm) 8.8(c).*

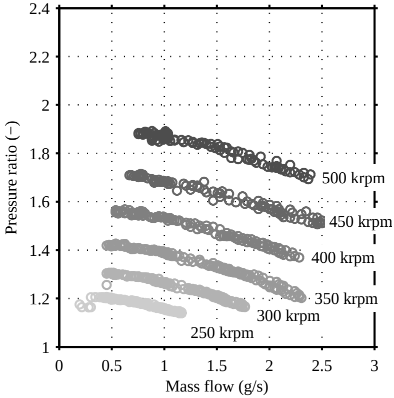

Figure 8.9: *Measured over pressure compressor map of the miniature turbocompressor, with a clearance of 35 μm at the first compressor wheel.*

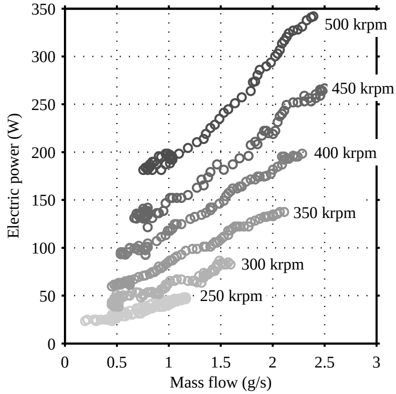

Figure 8.10: *Measured electric power consumed by the high speed electric drive system of the miniature turbocompressor at over pressure conditions.*

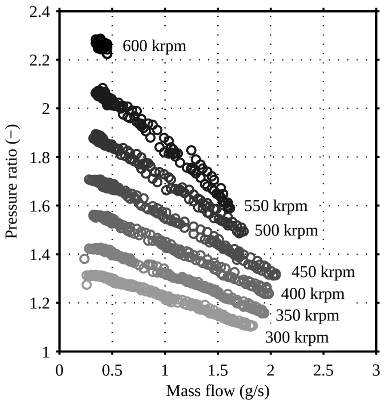

Figure 8.11: *Measured low pressure compressor map of the miniature turbocompressor, with a clearance of 70 μm at the first compressor wheel.*

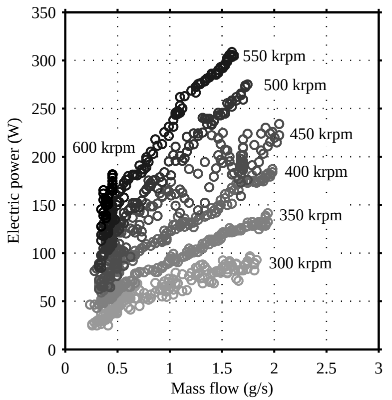

Figure 8.12: *Measured electric power consumed by the high speed electric drive system of the miniature turbocompressor at low pressure conditions.*

Chapter 9

Conclusion

9.1 Summary

In this thesis, bidirectional interfacing of compressed-air and electric power employing ultra-high-speed drives and turbomachinery is analyzed. A compressed-air-to-electric-power systems with an axial impulse turbine and a radial turbine are presented. The described axial impulse turbine system is optimized concerning power density (5.4 W/cm^3, neglecting throtteling valve) and shows a measured system efficiency of 24% and a maximum power output of 124 W at 370 000 rpm. The radial turbine system has an experimentally validated maximum speed of 625 000 rpm and measurements show that the system has a maximum power output of 170 W at 495 000 rpm and a maximum turbine efficiency of 52%.

The measured turbine and generator efficiencies of the descried systems in this thesis are significantly higher compared to similar, standard manufactured turbines and generators and MEMS manufactured turbines and μ-generators described in literature so far. Furthermore, the systems have higher electric output power than MEMS based systems. During assembly, special attention has to be given to the impeller-stator tip clearance in order not to sacrifice the turbine efficiency. Keeping this air gap as small as possible has a significant influence on the overall efficiency. The generator is optimized for lowest losses. For this reason, an optimization method is used which takes air friction losses, iron losses, copper losses and eddy current losses into account. The optimization results show that air friction losses influence the optimum design considerably, leading to a small rotor diameter at high speeds. The optimization constraints are set by the outer dimensions, mechanical stress limitations in the rotor, and the rotordynamic design.

Miniaturization and an increase in rotational speeds allow for a massive increase in power density. Drawbacks of miniaturization are the lower efficiencies (compared to standard size systems) and due to higher speeds the short lifetime of the high-speed ball bearings. With further miniaturization, e.g. MEMS based turbines and μ-generators the power density are increased, however the efficiency will decrease even further.

In order to be able to follow load steps at autonomous operation, a turbine-generator-system has to be extended with a valve in order to operate the turbine at highest possible efficiencies.

The two most common rectifiers, the active 3-phase PWM rectifier with sinusoidal phase currents and the active or passive 3-phase rectifier with an additional boost converter, are not the naturally best choices for low power, variable-speed and variable voltage PM generators, especially for high rotational speeds. The HCBR is an ideal choice for an interface between a variable-speed permanent-magnet generator and a constant dc output voltage. In this thesis, the previously missing analysis on the HCBR is provided, including the voltage space vector representation, the component current stresses and the common mode noise characteristics. With a novel modulation scheme referred to as the sector detection modulation scheme, the switching and conduction losses in the semiconductors can be lowered and therefore the power electronics efficiency increased. In an experimental setup this results in an efficiency increase of approximately 2% over the entire operating range. The modulation scheme uses a sensorless control method originally developed for high speed machines based on the back emf zero crossings detection. Further experimental results show that increasing the switching frequency can result in a higher total efficiency because additional ac inductors (and therefore their losses) can be omitted. Integration into a compressed-air-to-electric-power turbine generator system verifies the theoretical considerations.

Also the reversal of a turbine-generator system is feasible, resulting in ultra-compact, high power density turbocompressors. An experimental 500 000 rpm electrically driven turbocompressor system has been built, for various applications in the area of air and gas pressurization for future automotive, aerospace and residential applications. Measurements show that the system has a performance close to the specified design operating point, and that turbocompressors with speeds even above 500 000 rpm are feasible. The design includes the thermodynamic analysis, the optimization of the electric motor, the inverter, the control and the system integration with rotor dynamics and thermal considerations. The two-stage turbocompressor has been tested up to a speed of 600 000 rpm, where a maximal pressure ratio of 2.25 at a mass flow of 0.5 g/s has been reached under laboratory conditions.

With using several systems in a modular approach also higher power demands can be covered, with a power density much higher than with standard, lower speed turbomachinery. Turbomachinery with ultra-high-speeds in the area of 500 000 rpm are feasible for industrial applications, and concerning power density and efficiency, the systems are very attractive.

9.2 Outlook

A next research vector could be in the area of high or low fluid temperatures. The extension of the air turbine to a high-temperature gas turbine could result in a transportable power unit, e.g. the coupling of a turbine, compressor and a generator/motor. Technical difficulties for a portable gas turbine are the high temperatures at turbine inlet and consequently high temperature gradients with must result in a sophisticated thermal design. A major problem is the bearing technology for such a system, as ball bearings have temperature and lifetime limits at such high temperatures. But also rotordynamics, mechanical stress analysis and materials selection is challenging. As mentioned output stage turbo expanders used in cryogenic plants, could get braked electrically, which implies that the electric generator has an ambient temperature of only a couple of Kelvin. An area of research could be the investigation of high speed machines and bearing technologies at extreme by low temperatures.

Further research could take place in either downscaled or upscaled compressors and turbines. Air or refrigerant fluid compressors with higher electric power (e.g. 1-3 kW), at speed ranges between 250 000 rpm and 500 000 rpm and massflows of up to 50 g/s, would match the requirements for domestic heat pumps or fuel cell compressors. Also compressors and turbines in the low power range, e.g. 10 W to 50 W provide interesting applications. Such low power systems could be manufactured out of MEMS-based turbines and generators. For low power applications 2D-turbines turn out to be best choice, which additionally have advantages in manufacturing (etching or milling) and simple tip clearance control, while for higher power 3D-turbines are the best choice.

However, bearing lifetime is the main challenge before such ultra-high-speed turbine generator systems (or electrically driven compressors) can become widely used in industry. For reaching the acceptable lifetime the high-speed ball bearings must get replaced by air bearings or magnetic bearings. The ball bearings used for the experiments have losses of approximately 5 W at 500 000 rpm, but at 1 000 000 rpm the losses increase to approximately 18 W. Increasing the rotational speed and simultaneously increasing the efficiency implies that the effort for a further optimization should be on the bearing system, as this has the highest influence on the total system efficiency.

Bibliography

[1] A. Binder and T. Schneider, "High-speed inverter-fed AC drives," in *Proc. of the International Aegean Conference on Electrical Machines and Power Electronics (ACEMP 07)*, Sept. 2007, pp. 9–16. PDF

[2] S. Kang, S.-J. J. Lee, and F. B. Prinz, "Size does matter: The pros and cons of miniaturization," in *ABB Review 2*, 2001, pp. 54–62. PDF

[3] A. Mirandola and L. Minca, "Energy recovery by expansion of high pressure natural gas," in *Proc. of the 21st Intersociety Energy Conversion Engineering Conference (IECEC 86)*, vol. 1, Aug. 1986, pp. 16–21. PDF

[4] B. Lehman and E. Worrell, "Electricity production from natural gas pressure recovery using expansion turbines," in *Proc. of the ACEEE Summer Study on Energy Efficiency in Industry*, vol. 2, July 2001, pp. 43–54. PDF

[5] L. Guzzella, M. Betschart, T. Fluri, R. De Santis, C. Onder, and T. Auckenthaler, "Recuperative throttling of SI engines for improved fuel economy," in *Proc. of the SAE 2004 World Congress and Exhibition*, March 2004. PDF

[6] M. Michon, S. Calverley, R. Clark, D. Howe, J. Chambers, P. Sykes, P. Dickinson, M. McClelland, G. Johnstone, R. Quinn, and G. Morris, "Modelling and testing of a turbo-generator system for exhaust gas energy recovery," in *Proc. of the IEEE Vehicle Power and Propulsion Conference (VPPC 2007)*, Sept. 2007, pp. 544 –550. PDF

[7] Electricity from exhaust gases - is it possible? [Online]. Available: www.heat2power.net

[8] Controlled power technologies. Delivering CO_2 reduction technologies. [Online]. Available: www.cpowert.com

[9] P. R. LeGoy, "Utility requirements for power recovery in the cryogenic and chemical industry using variable frequency drives in the regenerative mode," in *Proc. of the IEEE Power Engineering Society Summer Meeting*, vol. 2, July 1999, pp. 542–547. PDF

[10] L. Zheng, T. X. Wu, D. Acharya, K. B. Sundaram, J. Vaidya, L. Zhao, L. Zhou, K. Murty, C. H. Ham, N. Arakere, J. Kapat, and L. Chow, "Design of a super-high speed permanent magnet synchronous motor for cryogenic applications," in *Proc. of the IEEE International Conference on Electric Machines and Drives (IEMDC 05)*, May 2005, pp. 874–881. PDF

[11] S. Sato, S. Jovanovic, J. Lang, and Z. Spakovszky, "Demonstration of a palm-sized 30 Watt air-to-power turbine generator," in *Proc. of the ASME Turbo Expo 2010: Power for Land, Sea and Air – Gas Turbine Technical Congress and Exposition*, June 2010. PDF

[12] U. Drescher and D. Brüggemann, "Fluid selection for the organic Rankine cycle (ORC) in biomass power and heat plants," in *Applied Thermal Engineering*, vol. 27, no. 1, Jan. 2007, pp. 223 – 228. PDF

[13] R. B. Peterson, H. Wang, and T. Herron, "Performance of a small-scale regenerative Rankine power cycle employing a scroll expander," in *Proc. of the Institution of Mechanical Engineers, Part A: Journal of Power and Energy*, vol. 222, no. 3, 2008, pp. 271–282. PDF

[14] R. Mongia, K. Masahiro, E. DiStefano, J. Barry, W. Chen, M. Izenson, F. Possamai, A. Zimmermann, and M. Mochizuki, "Small scale refrigeration system for electronics cooling within a notebook computer," in *the Tenth Intersociety Conference on Thermal and Thermomechanical Phenomena in Electronics Systems (ITHERM 06)*, June 2006, pp. 751–758. PDF

[15] N. Lapeña-Rey, J. Mosquera, E. Bataller, and F. Ortí, "The Boeing fuel cell demonstrator airplane," in *SAE Aero Tech Congress and Exhibition*, Sept. 2007. PDF

[16] H. T. Bradley, A. B. Moffitt, W. R. Thomas, D. Mavris, and E. D. Parekh, "Test results for a fuel cell-powered demonstration aircraft," in *SAE Power Systems Conference and Exposition*, Nov. 2006. PDF

[17] B. Blunier and A. Miraoui, "Air management in PEM fuel cell: State-of-the-art and prospectives," in *Proc. of the International Aegean Conference on Electrical Machines and Power Electronics (ACEMP 07)*, Sept. 2007, pp. 245–254. PDF

[18] J. Schiffmann, "Integrated design, optimization and experimental investigation of a direct driven turbocompressor for domestic heat pumps," Ph.D. dissertation, Ecole Polytechnique Federale de Lausanne, Switzerland, 2008. PDF

[19] D. P. Arnold, P. Galle, F. Herrault, S. Das, J. Lang, and M. G. Allen, "A self-contained, flow-powered microgenerator system," in *Proc. of the 5th International Workshop on Micro and Nanotechnology for Power Generation and Energy Conversion Applications (PowerMEMS 05)*, Nov. 2005, pp. 113–115. PDF

[20] J. Peirs, D. Reynaerts, and F. Verplaetsen, "Development of an axial microturbine for a portable gas turbine generator," *Journal of Micromechanics and Microengineering*, vol. 13, no. 4, pp. 190–195, July 2003. PDF

[21] ——, "A microturbine for electric power generation," *Sensors and Actuators A: Physical*, vol. 113, no. 1, pp. 86–93, 2004. PDF

[22] J. Peirs, T. Waumans, P. Vleugels, F. Al-Bender, T. Stevens, T. Verstraete, S. Stevens, R. D'hulst, D. Verstraete, P. Fiorini, R. A. Van den Braembussche, J. Driesen, R. Puers, P. Hendrick, M. Baelmans, and D. Reynaerts, "Micropower generation with microgasturbines: A challenge," in *Proc. of the Institution of Mechanical Engineers Part C: Journal of Mechanical Engineering Science*, vol. 221, no. 4, 2007, pp. 489–500. PDF

[23] S. Das, D. P. Arnold, I. Zana, J. W. Park, M. G. Allen, and J. H. Lang, "Microfabricated high-speed axial-flux multiwatt permanent-magnet generators–Part I: Modeling," vol. 15, no. 5, pp. 1330–1350, Oct. 2006. PDF

[24] D. P. Arnold, S. Das, J. W. Park, I. Zana, J. H. Lang, and M. G. Allen, "Microfabricated high-speed axial-flux multiwatt permanent magnet generators–Part II: Design, fabrication, and testing," vol. 15, no. 5, pp. 1351–1363, Oct. 2006. PDF

[25] D. P. Arnold, F. Herrault, I. Zana, P. Galle, J.-W. Park, S. Das, J. H. Lang, and M. G. Allen, "Design optimization of an 8-Watt, microscale, axial-flux, permanent-magnet generator," *Journal of Micromechanics and Microengineering*, vol. 16, no. 9, pp. 290–296, Sept. 2006. PDF

[26] B. C. Yen, F. Herrault, K. J. Hillman, M. G. Allen, F. F. Ehrich, S. Jacobson, C.-H. Ji, J. H. Lang, H. Li, Z. S. Spakovszky, and D. R. Veazie, "Characterization of a fully-integrated permanent-magnet turbine generator," in *Proc. of the 8th International Workshop on Micro and Nanotechnology for Power Generation and Energy Conversion Applications (PowerMEMS 08)*, Nov. 2008, pp. 121–124. PDF

[27] H. Raisigel, O. Cugat, and J. Delamare, "Permanent magnet planar micro-generators," in *Sensors and Actuators A*, vol. 130–131, 2006, pp. 438–444. PDF

[28] C. Zwyssig and J. W. Kolar, "Design considerations and experimental results of a 100 W, 500 000 rpm electrical generator," *Journal of Micromechanics and Microengineering*, vol. 16, no. 9, pp. 297–302, Sept. 2006. PDF

[29] K. Isomura, M. Murayama, S. Teramoto, K. Hikichi, Y. Endo, S. Togo, and S. Tanaka, "Experimental verification of the feasibility of a 100 W class micro-scale gas turbine at an impeller diameter of 10 mm," *Journal of Micromechanics and Microengineering*, vol. 16, no. 9, pp. 254–261, Sept. 2006. PDF

[30] S. Tanaka, K. Hikichi, S. Togo, M. Murayama, Y. Hirose, T. Sakurai, S. Yuasa, S. Teramoto, T. Niino, T. Mori, M. Esashi, and K. Isomura, "World's smallest gas turbine establishing Brayton cycle," in *Proc. of the 7th International Workshop on Micro and Nanotechnology for Power Generation and Energy Conversion Applications (PowerMEMS 07)*, Nov. 2007, pp. 359–362. PDF

[31] K. Hikichi, S. Togo, K. Isomura, M. Saji, N. Esashi, and S. Tanaka, "Ultra-high-speed tape-type radial foil bearing for micro turbomachinery," in *Proc. of the 9th International Workshop on Micro and Nanotechnology for Power Generation and Energy Conversion Applications (PowerMEMS 09)*, Nov. 2009, pp. 79–82. PDF

[32] P.-D. Pfister and Y. Perriard, "Very high speed slotless permanent magnet motors: Analytical modeling, optimization, design and torque measurement methods," vol. 57, no. 1, pp. 296–303, Jan. 2010. PDF

[33] D. Arnold, "Review of microscale magnetic power generation," vol. 43, no. 11, pp. 3940–3951, Nov. 2007. PDF

[34] C. Zwyssig, D. Krähenbühl, H. Weser, and J. W. Kolar, "A miniature turbocompressor system," in *Proc. of the Smart Energy Strategies (Zurich)*, Sept. 2008, pp. 144–149. PDF

[35] The Solar Impulse Challenge. [Online]. Available: www.solarimpulse.com

[36] M. V. Casey and C. J. Robinson, "A guide to turbocharger compressor characteristics," in *Dieselmotorentechnik, 10. Symposium, TAE Esslingen*, M. Bargende, Ed., 2006. PDF

[37] G. Cordes, *Strömungstechnik der gasbeaufschlagten Axialturbine.* Springer-Verlag, Berlin, Göttingen, Heidelberg, Germany, 1963.

[38] R. A. Van den Braembussche, "Micro gas turbines - a short survey of design problems," in *Proc. of the RTO-VKI lecture series: Micro gas turbines*, Dec. 2004. PDF

[39] Y. Gong, B. T. Sirakov, A. H. Epstein, and C. S. Tan, "Aerothermodynamics of micro-turbomachinery," in *Proc. of the ASME Turbo Expo: Power for Land, Sea, and Air*, June 2004, pp. 95–102. PDF

[40] O. Cordier, "Similarity conditions in turbomachines, Ähnlichkeitsbedingungen für Strömungsmaschinen," in *BWK (Brennstoff-Wärme-Kraft), German*, vol. 5, no. 10, Oct. 1953, pp. 337–340. PDF

[41] M. V. Casey, "The effects of Reynolds number on the efficiency of centrifugal compressor stages," *Journal of Engineering for Gas Turbines and Power*, vol. 107, no. 2, pp. 541–548, 1985. PDF

[42] R. A. Strub, L. Bonciani, C. J. Borer, M. V. Casey, S. L. Cole, B. B. Cook, J. Kotzur, H. Simon, and M. A. Strite, "Influence of the Reynolds number on the performance of centrifugal compressors," *Journal of Turbomachinery*, vol. 109, no. 4, pp. 541–544, 1987. PDF

[43] J. F. Gülich, "Effect of Reynolds number and surface roughness on the efficiency of centrifugal pumps," *Journal of Fluids Engineering*, vol. 125, no. 4, pp. 670–679, 2003. PDF

[44] M. Casey and C. Robinson, "A new streamline curvature throughflow code for radial turbomachinery," *Journal of Turbomachinery*, vol. 132, no. 3, pp. 31 021–31 031, April 2010. PDF

[45] W. Traupel, *Thermische Turbomaschinen. Klassiker der Technik.* Springer–Verlag Berlin, 1988, vol. 1.

[46] C. Zwyssig, "An ultra-high-speed electrical drive system," Ph.D. dissertation, Swiss Federal Institute of Technology Zurich, Switzerland, 2008. PDF

[47] S. Timoshenko and J. Goodier, *Theroy of elasticity.* New York, USA: McGraw-Hill, 1970. PDF

[48] C. Zwyssig, S. D. Round, and J. W. Kolar, "Analytical and experimental investigation of a low torque, ultra-high speed drive system," in *Proc. of the 41st IEEE Industry Applications Society Annual Meeting (IAS 06)*, vol. 3, Oct. 2006, pp. 1507–1513. PDF

[49] A. Borisavljevic, H. Polinder, and J. Ferreira, "On the speed limits of permanent-magnet machines," vol. 57, no. 1, pp. 220–227, Jan. 2010. PDF

[50] C. Zwyssig, S. D. Round, and J. W. Kolar, "An ultra-high-speed, low power electrical drive system," vol. 55, no. 2, pp. 577–585, Feb. 2008. PDF

[51] J. A. Ferreira, *Electromagnetic modeling of power electronic converters.* Norwell, USA: Kluwer Academic Publishers, 1989.

[52] C. P. Steinmetz, "On the law of hysteresis," vol. 72, no. 2, pp. 197–221, Feb. 1984. PDF

[53] J. Luomi, C. Zwyssig, A. Looser, and J. W. Kolar, “Efficiency optimization of a 100 W 500 000 r/min permanent-magnet machine including air-friction losses,” vol. 45, no. 4, pp. 1368–1377, July–Aug. 2009. PDF

[54] M. Mack, “Luftreibungsverluste bei elektrischen Maschinen kleiner Baugrösse,” Ph.D. dissertation, Universität Stuttgart, Stuttgart, Germany, 1967. PDF

[55] L. G. Frechette, S. A. Jacobson, K. S. Breuer, F. F. Ehrich, R. Ghodssi, R. Khanna, C. W. Wong, X. Zhang, M. A. Schmidt, and A. H. Epstein, “Demonstration of a microfabricated high-speed turbine supported on gas bearings,” in *Proc. of the Solid-State Sensor and Actuator Workshop*, June 2000, pp. 43–47. PDF

[56] I. Kovacevic, S. D. Round, J. W. Kolar, and K. Boulouchos, “Optimization of a wearable power system,” in *Proc. of the 11th Workshop on Control and Modeling for Power Electronics (COMPEL 08)*, Aug. 17–20, 2008, pp. 1–6. PDF

[57] G. Boyle, Ed., *Renewable Energy: Power for a sustainable Future.* Oxford University Press, 1996.

[58] D. J. Perreault and V. Caliskan, “Automotive power generation and control,” vol. 19, no. 3, pp. 618–630, May 2004. PDF

[59] J. Kikuchi, M. D. Manjrekar, and T. A. Lipo, “Performance improvement of half controlled 3-phase PWM boost rectifier,” in *Proc. of the 30th Annual IEEE Power Electronics Specialists Conference (PESC 99)*, vol. 1, June 1999, pp. 319–324. PDF

[60] ——, “Complementary half controlled three phase PWM boost rectifier for multi-DC-link applications,” in *Proc. of the 15th Annual IEEE Applied Power Electronics Conference and Exposition (APEC 2000)*, vol. 1, Feb. 6–10, 2000, pp. 494–500. PDF

[61] Y. Jang and M. M. Jovanovic, “A bridgeless PFC boost rectifier with optimized magnetic utilization,” vol. 24, no. 1, pp. 85–93, Jan. 2009. PDF

[62] J. Rivas, D. Perreault, and T. Keim, “Performance improvement of alternators with switched-mode rectifiers,” *IEEE Transaction on Energy Conversion*, vol. 19, no. 3, pp. 561–568, Sep. 2004. PDF

[63] J. C. Salmon, "Circuit topologies for PWM boost rectifiers operated from 1-phase and 3-phase AC supplies and using either single or split DC rail voltage outputs," in *Proc. of the 10th Annual Applied Power Electronics Conference and Exposition (APEC 95)*, no. 0, Mar. 5–9, 1995, pp. 473–479. PDF

[64] J. Miniböck, "Dreiphasen Dreischalter Dreipunkt Pulsgleichrichtersystem," Ph.D. dissertation, Swiss Federal Institute of Technology Zurich, Switzerland, March 2008. PDF

[65] J. Rodriguez, J. Dixon, J. Espinoza, J. Pontt, and P. Lezana, "PWM regenerative rectifiers: State of the art," vol. 52, no. 1, pp. 5–22, Feb. 2005. PDF

[66] L. Huber, Y. Jang, and M. M. Jovanovic, "Performance evaluation of bridgeless PFC boost rectifiers," vol. 23, no. 3, pp. 1381–1390, May 2008. PDF

[67] N. Bianchi, S. Bolognani, and F. Luise, "Potentials and limits of high-speed PM motors," vol. 40, no. 6, pp. 1570–1578, Nov.–Dec. 2004. PDF

[68] H. Ye, Z. Yang, J. Dai, C. Yan, X. Xin, and J. Ying, "Common mode noise modeling and analysis of dual boost PFC circuit," in *Proc. of the 26th Annual International Telecommunications Energy Conference (INTELEC 04)*, Sep. 19–23, 2004, pp. 575–582. PDF

[69] K. Iizuka, H. Uzuhashi, M. Kano, T. Endo, and K. Mohri, "Microcomputer control for sensorless brushless motor," no. 3, pp. 595–601, May 1985. PDF

[70] Gecko Research. [Online]. Available: www.gecko-research.com

[71] D. Krähenbühl, C. Zwyssig, H. Hörler, and J. W. Kolar, "Design considerations and experimental results of a 60 W compressed-air-to-electric-power system," in *Proc. of the 2008 IEEE/ASME International Conference on Mechatronic and Embedded Systems and Applications (MESA 08)*, Oct. 2008, pp. 375–380. PDF

[72] *Industrial, scientific and medical equipment - Radio-frequency disturbance characteristics - Limits and methods of measurement - Publication 11*, Comité international spécial des perturbations radioélectriques (CISPR) Std. 5.0, May 2009.

[73] W. R. Erickson and D. Maksimovic, *Fundamentals of Power Electronics*, 2nd ed. Springer, Jan. 2001.

[74] D. Krähenbühl, C. Zwyssig, H. Weser, and J. W. Kolar, "Mesoscale electric power generation from pressurized gas flow," in *Proc. of the 7th International Workshop on Micro and Nanotechnology for Power Generation and Energy Conversion Applications (PowerMEMS 07)*, Nov. 2007, pp. 289–292. PDF

[75] ——, "Experimental results of a mesoscale electric power generation system from pressurized gas flow," in *Proc. of the 8th International Workshop on Micro and Nanotechnology for Power Generation and Energy Conversion Applications (PowerMEMS 08)*, Nov. 2008, pp. 377–380. PDF

[76] D. Krahenbuhl, C. Zwyssig, H. Weser, and J. W. Kolar, "Theoretical and experimental results of a mesoscale electric power generation system from pressurized gas flow," *Journal of Micromechanics and Microengineering*, vol. 19, no. 9, pp. 94 009–94 015, Sept. 2009. PDF

[77] ——, "A miniature 500 000-r/min electrically driven turbocompressor," *IEEE Transactions on Industry Applications*, vol. 46, no. 6, pp. 2459 –2466, Nov.-Dec. 2010. PDF

[78] M. V. Casey, P. Dalbert, and E. Schurter, "Radial compressor stages for low flow coefficients," in *Proc. of the 4th European Congress on Fluid Machinery for Oil, Petrochemical and Related Industries, IMechE paper C403/004.*, 1990, pp. 117–125. PDF

List of Figures

List of Tables

Appendix A

Free Discharge from Nozzles

The mass flow through the nozzle guide vanes and the turbine can be modeled as a free discharge from a pressure-vessel, like schematically shown in Figure 2.2. The derivation of (2.26) and (2.27) starts with the Bernoulli equation, which can be expressed as

$$-\int_0^1 v dp = \frac{1}{2}\left(c_1^2 - c_0^2\right) + g(z_1 - z_0) + W_{01}. \tag{A.1}$$

It can be assumed that no work is done ($W_{01} = 0$), the change in potential energy can be neglected ($z_0 = z_1$) and further can be assumed that the velocity in the reservoir is zero, e.g. $c_0 = 0$. Solving (A.1) for the velocity c_1 results in

$$c_1 = \sqrt{-2\int_0^1 v dp}. \tag{A.2}$$

The assumption that there is no heat exchange ($q_{01} = 0$) gives the adiabatic relationship $p \cdot v^{\kappa} = const$ whith can be expressed as

$$p_0 v_0^{\kappa} = p_1 v_1^{\kappa} \tag{A.3}$$
$$p_0^{\frac{1}{\kappa}} v_0 = p_1^{\frac{1}{\kappa}} v_1 \tag{A.4}$$
$$v_{1(p_1)} = p_0^{\frac{1}{\kappa}} v_0 p_1^{-\frac{1}{\kappa}} \tag{A.5}$$

and which can be substituted into $-\int_0^1 vdp$

$$-\int_0^1 vdp = -p_0^{\frac{1}{\kappa}} v_0 \int_0^1 p^{-\frac{1}{\kappa}} dp \tag{A.6}$$
$$= -p_0^{\frac{1}{\kappa}} v_0 \left[\frac{p^{\left(-\frac{1}{\kappa}+1\right)}}{-\frac{1}{\kappa}+1} \right]_0^1 \tag{A.7}$$
$$= -\frac{\kappa}{\kappa - 1} p_0^{\frac{1}{\kappa}} v_0 \left[p_1^{\frac{\kappa-1}{\kappa}} - p_0^{\frac{\kappa-1}{\kappa}} \right] \tag{A.8}$$
$$= \underbrace{\frac{\kappa}{\kappa - 1}}_{\frac{c_p}{R}} \underbrace{p_0 v_0}_{RT_0} \left[1 - \left(\frac{p_1}{p_0} \right)^{\frac{\kappa-1}{\kappa}} \right] \tag{A.9}$$

resulting in

$$c_1 = \sqrt{RT_0} \sqrt{\frac{2\kappa}{\kappa - 1} \left[1 - \left(\frac{p_1}{p_0} \right)^{\frac{\kappa-1}{\kappa}} \right]}. \tag{A.10}$$

To compute the mass flow rate $\dot{m}$, the continuity equation

$$\dot{m} = A \cdot c_1 \cdot \rho_1 \tag{A.11}$$

is used together with the definition of the density

$$\rho_1 = \frac{1}{v_1} = \frac{1}{v_0} \left(\frac{p_1}{p_0} \right)^{\frac{1}{\kappa}} = \frac{p_0}{RT_0} \left(\frac{p_1}{p_0} \right)^{\frac{1}{\kappa}} \tag{A.12}$$

to give

$$\dot{m} = A\frac{p_0}{RT_0}\sqrt{RT_0}\sqrt{\left(\frac{p_1}{p_0}\right)^{\frac{2}{\kappa}}}\sqrt{\frac{2\kappa}{\kappa-1}\left[1-\left(\frac{p_1}{p_0}\right)^{\frac{\kappa-1}{\kappa}}\right]} \tag{A.13}$$

$$= A\frac{p_0}{\sqrt{RT_0}}\underbrace{\sqrt{\frac{2\kappa}{\kappa-1}\left[\left(\frac{p_1}{p_0}\right)^{\frac{2}{\kappa}}-\left(\frac{p_1}{p_0}\right)^{\frac{\kappa+1}{\kappa}}\right]}}_{\Psi}. \tag{A.14}$$

Curriculum Vitæ

Name	Daniel Krähenbühl
Birth	5^{th} August 1982
Place of birth	Bern, BE (Switzerland)
Citizen of	Switzerland
Education	1989–1991 Elementary School, Cleveland, Ohio (USA)
	1991–1998 Primary and Secondary School, Münsingen
	1998–2001 Mathematisch-Naturwissenschaftliches Gymnasium (MNG), Bern Neufeld
University	2001–2007 ETH Zürich M.Sc. in Electrical Engineering
Doctorate	2007–2010 Doctorate at the Power Electronics Systems Laboratory (PES), ETH Zurich
Work	2010–present Project Manager at Celeroton Ltd.